MASARYK
UNIVERSITY

Faculty of Science

DOCTORAL THESIS

Brno 2024 Martin Blažek

MASARYK UNIVERSITY

Faculty of Science

Department of Theoretical Physics and Astrophysics

Astronomical Institute
of the Czech Academy of Sciences

Doctoral Thesis

Characterisation of exoplanetary systems

Martin Blažek

Supervisor: Dipl.-Phys. Petr Kabáth, Dr. rer. nat.

Brno 2024

Bibliografický záznam

Autor: Martin Blažek,
Přírodovědecká fakulta, Masarykova univerzita,
Ústav teoretické fyziky a astrofyziky;
Astronomický ústav Akademie věd České republiky

Název práce: Charakterizace exoplanetárních systémů

Studijní program: Fyzika

Specializace: Astrofyzika

Školitel: Dipl.-Phys. Petr Kabáth, Dr. rer. nat.

Akademický rok: 2024/2025

Počet stran: 96

Klíčová slova: Exoplanety; Atmosféry exoplanet; Přehlídky WASP a OGLE; Vesmírná mise TESS; Fotometrická metoda

Bibliographic entry

Author:	Martin Blažek Faculty of Science, Masaryk University, Department of Theoretical Physics and Astrophysics; Astronomical Institute of the Czech Academy of Sciences

Title of Thesis:	Characterisation of exoplanetary systems
Degree programme:	Physics
Specialisation:	Astrophysics
Supervisor:	Dipl.-Phys. Petr Kabáth, Dr. rer. nat.
Academic Year:	2024/2025
Number of Pages:	96
Keywords:	Exoplanets; Exoplanetary atmospheres; WASP and OGLE surveys; TESS space mission; Photometric method

Abstrakt

Fotometrická pozorování jsou stěžejní jak pro detekci exoplanet, tak i pro studium jejich atmosfér. Asi tři čtvrtiny z 5700 dodnes potvrzených exoplanet byly objeveny fotometrickou metodou (detekce tranzitu). Atmosféry exoplanet, jejich chemické složení a teplotní profily lze studovat spektroskopicky během tranzitu nebo fotometricky při okultacích. Disertační práce je zaměřena na analýzu fotometrických dat tzv. horkých Jupiterů získaných z pozemních observatoří ESO a vesmírné mise *TESS* za účelem hledání a studia okultací. Analýza vedla k několika úspěšným detekcím okultací ve filtru NB2090 ($\lambda = 2.09\,\mu$m) a *TESS* s následujícími hloubkami okultací ($\delta_{\rm occ}$): WASP-43 b (NB2090): $\delta_{\rm occ} = 1.47 \pm 0.21$ ppt, WASP-18 b (*TESS*): $\delta_{\rm occ} = 0.35 \pm 0.01$ ppt, WASP-36 b (*TESS*): $\delta_{\rm occ} = 0.18 \pm 0.05$ ppt, WASP-50 b (*TESS*): $\delta_{\rm occ} = 0.20 \pm 0.06$ ppt. Dále byly stanoveny horní limity okultace. Mimo méně ostrých limitů z dat ESO byly z dat *TESS* pro planety WASP-43 b, WASP-51 b a OGLE2-TR-L9 b stanoveny horní limity okultací: $\delta_{\rm occ} < 0.18$ ppt, $\delta_{\rm occ} < 0.11$ ppt a $\delta_{\rm occ} < 1.58$ ppt, v uvedeném pořadí. S výjimkou WASP-18 b a WASP-43 b jsou to první stanovené limity hloubky okultace. Z nich bylo následně odvozeno geometrické albedo. Nízké výsledné hodnoty albeda jsou v souladu s hodnotami pro jiné horké Jupitery, uvedenými v literatuře. Dále byly vytvořeny modely emisního spektra a teplotního profilu planet WASP-18 b a WASP-43 b, které jsou schopny vysvětlit pozorování *TESS* a HAWK-I. Modely vyžadují neefektivní distribuci tepla mezi polokoulemi a taktéž na denní straně. Za další, není zapotřebí odraženého světla, což odpovídá čistému termálnímu záření a absenci mraků. V neposlední řadě, data byla nejlépe popsána modelem, kde teplotní profil WASP-18 b vyžaduje teplotní inverzi, zatímco pro WASP-43 b toto požadováno není.

Abstract

Photometric observations are crucial both for detection of exoplanets and for studying their atmospheres. From 5700 confirmed exoplanets to date about three quarters of them have been discovered by the photometric method (transit detection). Atmospheres of exoplanets, their chemical composition and temperature profiles can be studied spectroscopically during transits or photometrically during occultations. The doctoral thesis is aimed to analyse photometric data of so-called hot Jupiters obtained from ground-based ESO observatories and a space-based *TESS* mission to seek and study occultations. The analysis led to several successful occultation detections in NB2090 filter ($\lambda = 2.09\,\mu\mathrm{m}$) and *TESS* with the following occultation depths (δ_{occ}): WASP-43 b (NB2090): $\delta_{\mathrm{occ}} = 1.47 \pm 0.21$ ppt, WASP-18 b (*TESS*): $\delta_{\mathrm{occ}} = 0.35 \pm 0.01$ ppt, WASP-36 b (*TESS*): $\delta_{\mathrm{occ}} = 0.18 \pm 0.05$ ppt, and WASP-50 b (*TESS*): $\delta_{\mathrm{occ}} = 0.20 \pm 0.06$ ppt. Furthermore, upper limits on occultation depth have been placed. Besides less strict constraints from ESO data, for planets WASP-43 b, WASP-51 b and OGLE2-TR-L9 b from *TESS* data the upper limits are as follows: $\delta_{\mathrm{occ}} < 0.18$ ppt, $\delta_{\mathrm{occ}} < 0.11$ ppt and $\delta_{\mathrm{occ}} < 1.58$ ppt, respectively. With the exception of WASP-18 b and WASP-43 b those are the first derived constraints on occultation depths. The derived depths were subsequently used to infer the geometric albedo. The acquired low albedo values are consistent with albedos inferred for other hot Jupiters cited in literature. In addition, models of emission spectra and temperature profiles of WASP-18 b and WASP-43 b have been created. They are able to explain the *TESS* and HAWK-I observations. The models require inefficient heat redistribution between the hemispheres and on the dayside. Further, no reflected light is needed to explain the observations and this corresponds to pure thermal emission and no cloud coverage. Moreover, the data have been best described by a model where the inferred temperature profile of WASP-18 b requires temperature inversion whilst for WASP-43 b no inversion is needed.

Acknowledgements

I would like to thank my supervisor Dr. Petr Kabáth for his grant providing me a job at the Astronomical Institute of the Czech Academy of Sciences in Ondřejov where surrounded by the beautiful nature with a lot of trees I could work on this thesis in peace. I also thank him and my co-supervisor Mgr. Marek Skarka, Ph.D., of the Astronomical Institute in Ondřejov for their suggestions and comments on my thesis to make it clearer and more understandable. I also thank my girlfriend Anička for her patience and giving me space to finish my studies in recent years. Further, my thanks go to my deceased parents since they brought me to my birth. At last, I thank Mother Nature for its complexity and allowing us to be studied.

I declare that this thesis has been written by my own with the use of cited resources.

Teplice (CZ), 14$^{\text{th}}$ October 2024 .....

Martin Blažek

List of Publications

Blažek, M.; Kabáth, P.; Piette, A. A. A.; Madhusudhan, N.; Skarka, M.; Šubjak, J.; Anderson, D. R.; Boffin, H. M. J.; Cáceres, C. C.; Gibson, N. P.; Hoyer, S.; Ivanov, V. D.; Rojo, P. M. (2022) *Constraints on TESS albedos for five hot Jupiters.* Monthly Notices of the Royal Astronomical Society, Volume 513, Issue 3, pages 3444–3457.

The article has been prepared entirely by the main author (M.B.) except making atmospheric models and the section describing them.

Kabáth, P.; Chaturvedi, P.; MacQueen, P. J.; Skarka, M.; Šubjak, J.; Esposito, M.; Cochran, W. D.; Bellomo, S. E.; Karjalainen, R.; Guenther, E. W.; Endl, M.; Csizmadia, S.; Karjalainen, M.; Hatzes, A.; Žák, J.; Gandolfi, D.; Boffin, H. M. J.; Vines, J. I.; Livingston, J. E.; García, R. A.; Marthur, S.; Gonzáles-Cuesta, L.; **Blažek, M.**; and 33 others together with KESPRINT team. (2022) *TOI-2046b, TOI-1181b, and TOI-1516b, three new hot Jupiters from TESS: planets orbiting a young star, a subgiant, and a normal star.* Monthly Notices of the Royal Astronomical Society, Volume 513, Issue 4, pages 5955–5972.

M.B. contributed as a data observer, an editor of the article, and performed a partial analysis of the presented data.

Šubjak, J.; Endl, M.; Chaturvedi, P.; Karjalainen, R.; Cochran, W. D.; Esposito, M.; Gandolfi, D.; Lam, K. W. F.; Stassun, K.; Žák, J.; Lodieu, N.; Boffin, H. M. J.; MacQueen, P. J.; Hatzes, A.; Guenther, E. W.; Georgieva, I.; Grziwa, S.; Schmerling, H.; Skarka, M.; **Blažek, M.**; and 24 others. (2022) *TOI-1268b: The youngest hot Saturn-mass transiting exoplanet.* Astronomy & Astrophysics,Volume 662, id. A107, 21 pp.

M.B. contributed as an observer of the presented data.

Blažek, M.; Kabáth, P.; Skarka, M.; Klocová, T.; Špoková, M.; Šubjak, J.; Dvořáková, J.; Žák, J.; Dupkala, D.; Plávalová, E. (2020) *The Ondřejov Exoplanet Group.* (2020) Proceedings of the conference Stars and their Variability Observed from Space, held in Vienna on $19^{\text{th}} - 23^{\text{rd}}$ August 2019. Eds.: C. Neiner, W. W. Weiss, D. Baade, R. E. Griffin, C. C. Lovekin, A. F. J. Moffat. University of Vienna, 2020, pages 443–445.

The poster and the contribution to the proceedings were prepared entirely by M.B.

Šubjak, J.; Sharma, R.; Carmichael, T. W.; Johnson, M. C.; Gonzales, E. J.; 31 others; **Blažek, M.**; and 44 others. (2020) *TOI-503: The First Known Brown-dwarf Am-star Binary from the TESS Mission*. The Astronomical Journal, Volume 159, Issue 4, id. 151, 19 pp.

M.B. contributed as an observer and performed a partial analysis of the presented data.

Kabáth, P.; Skarka, M..; Sabotta, S.; Guenther, E.; Jones, D.; Klocová, T.; Šubjak, J.; Žák, J.; Špoková, M.; **Blažek, M.**; Dvořáková, J.; Dupkala, D.; Fuchs, J.; Hatzes, A.; Kortusová, E.; Novotný, R.; Plávalová, E.; Řezba, L.; Sloup, J.; Škoda, P.; Šlechta, M. (2020) *Ondřejov Echelle Spectrograph, Ground Based Support Facility for Exoplanet Missions*. Publications of the Astronomical Society of the Pacific, Volume 132, Issue 1009, id. 035002, 12 pp.

M.B. contributed as an observer and performed a partial analysis of the presented data.

Skarka, M.; Kabáth, P.; Paunzen, E.; Fedurco, M.; Budaj, J.; Dupkala, D.; Krtička, J.; Hatzes, A.; Pribulla, T.; Parimucha, Š.; Mikulášek, Z.; Guenther, E.; Sabotta, S.; **Blažek, M.**; Dvořáková, J.; Hambálek, L.; Klocová, T.; Kollár, V.; Kundra, E.; Šlechta, M.; Vaňko, M. (2019) *HD 99458: First time ever Ap-type star as a δ Scuti pulsator in a short period eclipsing binary?* Monthly Notices of the Royal Astronomical Society, Volume 487, Issue 3, pages 4230–4237.

M.B. contributed as an observer and performed a partial analysis of the presented data.

Blažek, M.; Kabáth, P.; Klocová, T.; Skarka, M. (2018) *Automation of processing and photometric data analysis for transiting exoplanets observed with ESO NIR instrument HAWK-I.* Proceedings of the 49$^{\text{th}}$ Conference on Variable Stars Research, vol. 187, held 3$^{\text{rd}}$ – 5$^{\text{th}}$ November 2017 in Brno, Czech Republic, pages 12–16.

The contribution to the proceedings was prepared entirely by M.B.

Contents

Now it is the last time to leave this place,
where I have stayed a part of my life.
In thoughts I had many times left to Space,
and appeared there where all is calm and live.

We have never been for such mad step prepared
that is why to jump straight to the cosmic sea.
The Space is with much beauty starred,
and after all obstacles we may it see.

Those blinkings invite us to learn things,
we are sure that It is to become.
Yet a different mind another way thinks,
be aware if it means DO NOT COME!

THE AUTHOR

1. Introduction

Since ancient ages, people were thinking about worlds outside our Earth. The ideas were mainly speculations of philosophers and others who were interested in nature and especially the cosmos. But as time was passing, philosophers began to be more scientific and ideas became discoveries—based on sophisticated observations and calculations.

It took long time until the first exoplanet, a planet orbiting other star than the Sun, has been discovered. The first discoveries later showed that they were just false detection of an exoplanet (Campbell et al., 1988) or, these newly discovered planets were retracted to be exoplanets soon after their discovery and had to be re-confirmed later. But finally, in the nineties of the twentieth century, the first invincible discoveries have come—a planetary system around a pulsar star, PSR 1257+12 (Wolszczan & Frail, 1992), and especially a system around a Sun-like star, 51 Pegasi (Mayor & Queloz, 1995). Since then, this relatively new field of astronomical and astrophysical research has been evolving very rapidly.

We found that our imagination how planets outside our Solar System can look like and where they can be found was not sufficiently rich. And what more, the first discovered exoplanets instantly showed us that we had to expand our set of possible types of planets—we found, e.g., planets orbiting a pulsar or giant planets orbibing closer than Mercury orbits the Sun.

This led scientists to categorise exoplanets. By size we now clasify them as Earth-size planets, super-Earths, Neptune-like planets, or Jupiter-like planets. By mass they are clasified as sub-/super-/Earths/Neptunes/Jupiters or super-Jupiters (Perryman, 2018). The planetary temperature is also important. It depends on the stellar temperature, the distance from the parent star and also on the composition of the atmosphere of the planet. Thus, by temperature we clasify planets as cold, warm, hot, or ultra-hot. As an example, 'hot Jupiters' is a large category of hot and very big exoplanets; therefore, their detection is relatively easy.

Soon after first exoplanets were discovered, their characterisation became also possible. To confirm an object to be an exoplanet, we need to know the mass of that object. Knowing also the radius, we can simply derive the average density of the exoplanet. This allows us to characterise the planet type. Today, about 30 years after the first exoplanet discovery, we are able to find out many important characteristics such as composition of their atmospheres, inner composition, or describe their evolution.

One of the most important problems is to describe the atmosphere of an exoplanet: to derive its chemical composition, pressure–temperature profiles, reveal atmospheric layers or sources of planetary and atmospheric radiation. The two main radiation sources of a planet, reflected light and thermal radiation, are typically detectable in the visible and the (near) infrared bandpass, respectively. As most of space missions and ground-based instruments work in these wavelengths, we have a lot of potential detectors of exoplanetary radiation at disposal.

To measure reflectivity of a planet, we generally use *albedo*, A. To describe reflectivity over all wavelengths, the Bond albedo (A_{B}) is used, whilst the geometric albedo (A_{g}) is used for observations at a specific wavelength/frequency. This can be photometrically measured during occultations (e.g. Angerhausen et al. 2015, Mallonn et al. 2019), i.e. when a planet is hidden behind its host star. The albedo reveals us some details of the atmosphere, its physical properties and even the presence of hazes and clouds can be detected (e.g. Burrows et al., 2008).

If we measure a high albedo value, it indicates that significant portion of optical radiation is scattered and this may come from possible presence of clouds and/or hazes.

For several types of planets the geometric albedo of their atmosphere was measured, suggesting various cloud coverage from no clouds to significant cloud coverage, e.g. TrES-2 b—a hot Jupiter: $A_g = 0.025 \pm 0.007$ (Kipping & Spiegel, 2011), WASP-12 b—an ultra-hot Jupiter: $A_g < 0.064$ (Bell et al., 2017), Kepler-7 b—a hot Jupiter: $A_g = 0.35 \pm 0.02$ (Demory et al., 2011, 2013), HAT-P-11 b—a warm/hot Neptune: $A_g = 0.39 \pm 0.07$ (Huber et al., 2017), HD 189733 b—a warm/hot Jupiter: $A_g = 0.40 \pm 0.12$ (Evans et al., 2013), Kepler-10 b—a hot super-Earth: $A_g < 0.61$ (Batalha et al., 2011). Observations suggest that clouds are mostly found in cooler planets than in hotter planets and that the transition between atmospheres with and without clouds is ≈ 1900 K (Parmentier et al., 2016).

In contrast to observations in the visible band allowing us to constrain the planetary albedo, detected radiation from a planet measured in the near-infrared (NIR) or infrared band is of thermal-radiation nature. Thermal emission of atmospheres is important for studying of chemical composition and deriving temperature profiles. To study exoplanetary atmospheres in detail we ideally observe both in the visible and NIR. These observations are highly complementary since they probe different atmospheric layers.

For this thesis, data sets from instruments working in both the NIR and the visible band were analysed. The NIR data were obtained by the High Acuity Wide-field K-band Imager (HAWK-I) on the Very Large Telescope (VLT) of ESO. The HAWK-I instrument is suitable to probing thermal emission of exoplanetary atmospheres (e.g. Anderson et al. 2010, Gibson et al. 2010). For observations in the visible bandpass, data from Transiting Exoplanet Survey Satellite (*TESS*; Ricker et al., 2014) was used to measure reflected light and to provide constraints on the geometric albedo of the studied exoplanets (e.g. Shporer et al. 2019, Beatty et al. 2020).

The motivation for this doctoral thesis is to contribute to the research of exoplanetary atmospheres by the photometric method for which the measured occultation depth is the crucial outcome. The obtained depth then leads to derivation of the atmospheric albedo which also implies an estimate of thermal emission. For WASP-18 b and WASP-43 b as the opposite ends of the temperature range (≈ 2500 K vs ≈ 1400 K), atmospheric models will be presented and investigated.

The goal of characterisation of atmospheres of hot Jupiters is revealing diversity of this type planets as well as comparison with Solar-Systems planets, mainly with Jupiter. In general, this field of exoplanetary research is vital since this is an important step to a biosignature detection which is a crucial point on the way for finding life outside the Solar System.

This thesis is structured as follows: after the introductory section the timeline of the exoplanetary research is described in Section 2. In Section 3, the studied physical quantities of exoplanetary atmospheres together with methods used for their detection and characterisation are described. The used data, instruments and software are presented in Section 4. The data which did not lead to successful detections of occultations are analysed in Section 5 whereas those with successful detections are analysed in Section 6. Subsequently, atmospheric models are presented and described in Section 7 and the obtained results of the whole thesis are summarised in Section 8.

2. From history to future

2.1. Beginnings of the exoplanetary research

A long time ago, some scholars were playing with an idea—and some were sure about it—that there is not only one world, only one (habitable) planet. They really believed that there was plenty of planets which were similar to that of ours. On the other hand, there were also extreme opinions claiming the contrary.

One of those who believed in other worlds was a Greek philosopher Epicurus of Samos (341 B.C.E.–270 B.C.E.) who, loosely translated, claimed that 'there is an endless number of worlds alike the ours as well as different ones not similar to our world at all'. As the opposite of this statement an opinion of another Greek philosopher, Aristotle of Stagira (384 B.C.E.–322 B.C.E.), can be chosen claiming that 'there can not be more worlds than one'.

Either way, the truth is that such claims were only speculations until the second half of the twentieth century. There was no observational technique providing facts to support these 'assumptions'. We could imagine that nowadays, in the age of progress in technology, we can observe planets around other stars without any problem. But it is not like that. Distances between us and the planets being searched are still very large. Moreover, unlike stars, radiation of planets in the visible band is below our detection limits. But what we are able to measure is stellar radiation scattered or/and reflected by planets.

If we look at modern observations of exoplanets, it is worth to mention the story of the Dutch pioneer in exoplanet search Piet van de Kamp (1901–1995). After his discovery and publishing of an exoplanet orbiting the Barnard's star (a star with great proper motion) in the 1960s, Kamp with his assistants made many images of this star on photographic plates. From deviations of the position of the star in the images, he came to a conclusion that a planet of 1.6-Jupiter-mass is orbiting the Barnard's star (van de Kamp, 1963). Moreover, soon after that he clarified his result that even two planets are orbiting the star (van de Kamp, 1982). Although it was not an officially confirmed exoplanet, after some time first critics appeared claiming that they had not found anything anomalous about the star (e.g. Gatewood & Eichhorn, 1973). At the time, computing was more advanced and their rigorous method to compute positions of stars did not confirm the existence of a planetary companion of the Barnard's star. Even other methods contradicted the Kamp's results. Till the very end of his life, Kamp was convinced of his truth and even though he was not right, with his immense vitality he had aroused interest of an expert audience about a topic which began to wildly evolve after his death in 1995.

Shortly before Kamp, Struve (1952) made a theoretical estimate revealing a possible detection of Jupiter-sized planets on close orbits around their stars by using transit (dimming of light of the host star due to crossing of a planet in front of it) and radial velocity (measuring the motion of the host star about a star–planet centre of mass) methods. Twenty years later, Griffin (1973) proposed using telluric lines to improve accuracy of stellar radial velocities. In the 1980s, Campbell et al. (1988) claimed a discovery of Jupiter-size planets using radial velocities of some stars but the existence of one of the planets was later rejected (Walker et al., 1992) (but being finally confirmed by Hatzes et al. 2003). A discovery of a brown dwarf (or possibly a giant planet) was reported by Latham et al. (1989), again using spectroscopic measurements.

Through this listing of important works I came to the recent past of the introductory part, it is worth to mention the definition of an exoplanet which was formulated in this millennium. According to the decision accepted at a congress of the International Astro-

nomical Union (IAU) in Prague in August 2006 (van der Hucht, 2007), the solar-system planet is a celestial body *which is in orbit around the Sun, has a sufficient mass for its self-gravity to overcome rigid body forces so that it assumes a hydrostatic equilibrium (nearly round) shape, and has cleared the neighbourhood around its orbit.* Although there is no definition of an exoplanet, the IAU's Working Group on Extrasolar Planets proposed a working definiton of an exoplanet (Lecavelier des Etangs & Lissauer, 2022) that *these objects are with true masses below the limiting mass for termonuclear fushion of deuterium (which is about 13 Jupiter masses) that orbit stars or stellar remnants.* Considering the size required for an exoplanet to be a planet, it is the same like a solar-system planet.

By mentioning the definitions I got to the one of the most important milestones of this field—the first real discovery of an extrasolar planet. It is not, nevertheless, considered as the first of its kind from all points of view. The reason is that this first exoplanet is orbiting a pulsar (PSR 1257+12)—a type of a star where no one had expected that something like this was even possible. This discovery was made by Alexander Wolszczan and Dale Frail in 1992 (Wolszczan & Frail, 1992). By the way, as of now there are three confirmed planets orbiting this pulsar. Owing to this discovery, our view at forming planets have changed since it showed that planets can form and exist even in extreme conditions.

As already mentioned, the first discovery of an extrasolar planet came in 1992, yet a planet not orbiting a Sun-like star. In October 1995 in Florence in Italy, a conference on topic 'Cool stars' was held. Michel Mayor of Geneva Observatory presented there his contribution concerning a planetary companion of a cool-type star. He reported that together with Didier Queloz they had measured radial velocities of star 51 Pegasi (Mayor & Queloz, 1995). This star is found about fifty light years from the Earth and it is a similar star to our Sun. Based on spectroscopic observations it is known that this star is being orbited by an object of a planetary mass (roughly one half of the mass of Jupiter) in a distance of 0.052 AU. The orbit is almost circular and the orbital period is 4.23 days. The orbital distance, i.e. the semi-major axis, is really short—only one eighth of the Sun–Mercury distance.

In a short time gap after the first exoplanet orbiting a Sun-like star, other discoveries followed. Therefore, it is logical that the curve of growth of the number of discovered exoplanets began to rise steeply. As of 13$^{\text{th}}$ October 2024, more than 5700 planets have been confirmed in about 4300 single and nearly 1000 multiple planetary systems (NASA-Archive). In the beginning, most exoplanets had been discovered by using radial-velocity-measurement (spectroscopic) method but in the last years the transit (photometric) method allows us to discover majority of new exoplanets, see Figure 1. This is mainly due to space missions, such as *Kepler* and *TESS* (see further). Nevertheless, the methods are complementary in the way that spectroscopy provides us planetary mass whilst photometry gives us planetary size.

Apart from the discovery of an exoplanet, there are also other important moments of this field of research. The first transit of an exoplanet should be mentioned. It was observed in 2000 by David Charbonneau and Timothy Brown (Charbonneau et al., 2000). The measured star was HD 209458. Moreover, these observers also detected an atmosphere of this exoplanet (HD 209458 b) in 2002 (Charbonneau et al., 2002). Another important milestone was the first real image of an exoplanet (2M 1207 b) by Gael Chauvin at the observatory Cerro Paranal in Chile in 2004 (Chauvin et al., 2004).

The above-mentioned first detection of the exoplanetary atmosphere was reached from *HST*/STIS data in which sodium as an absorption feature was detected. It was followed by a detection of hydrogen (Vidal-Madjar et al., 2003) and oxygen together with carbon (Vidal-Madjar et al., 2004), all in the atmosphere of that planet. Another atoms and/or

molecules in atmospheres of other planets were found, e.g. H_2O/water (HD 189733 b; Tinetti et al. 2007), CH_4/methane (HD 189733 b; Swain et al. 2008), sodium (HD 189733 b; Redfield et al. 2008), CO/carbon monoxide (HD 209458 b; Snellen et al. 2010), or pottasium (HD 80606 b, XO-2 b; Sing et al. 2011, Colón et al. 2012, respectively).

The method of occultation photometry led to other signs of existing planetary atmospheres—detections of both thermal emission and reflected light. Thermal emission which provides thermal structures, insights into chemical compositions, transport of energy and other properties, was detected by e.g. Burrows et al. (2008), Gibson et al. (2010), Cowan & Agol (2011), or Parmentier et al. (2016). Reflected light, revealing us clouds and hazes and providing insights into the physical properties of atmospheres, was measured by e.g. Burrows et al. (2008), Cowan & Agol (2011), Esteves et al. (2015), or Blažek et al. (2022). An important feature of atmospheres of some hot-Jupiter planets is the presence of a thermal inversion layer, such as detected e.g. in the atmosphere of HD 209458 b (Knutson et al., 2008).

To determine the bulk composition of an atmosphere of a planet, atmospheric models (reflected light, transmission and emission spectra) and temperature profiles are constructed. The codes used for modelling of exoplanetary atmospheres are often variants of general codes adapted for planets, such as models for transiting hot Jupiters in general (e.g. Burrows et al. 1997), or for giant transiting exoplanets, e.g. HD 209458 b (Baraffe et al., 2003) or TrES-1 b & HD 209458 b (Burrows et al., 2005). Studying atmospheres can also allow us to derive their heat redistribution and, thus, maps of temperature distribution may be created (e.g. HD 189733 b; Knutson et al. 2007).

During the journey to find other worlds beyond the Solar System people had come and left but the questions remained the same: *Are there similar planetary systems to ours?; Do they have Earth-like planets?; How did they evolve?; How old are they?...*, and the main question: *Is there another Earth hosting life?*

2.2. Recent, current and future research

There are and were many projects to observe exoplanets, both spaced- and ground based. In this chapter, some of them are briefly described together with their merit for the exoplanetary research.

- WASP (Wide Angle Search for Planets; Pollacco et al. 2006)—a ground-based international project. It is aimed to search for exoplanets by using the transit method which has been working since 1999. It includes two robotic observatories, each with eight cameras observing in all bandpasses (*'clear'*)—SuperWASP-north (La Palma, Canary Islands, Spain) and SuperWASP-south (Southerland, South Africa). It has discovered around 200 exoplanets until now.

- *CoRoT* (Convection, Rotation and planetary Transits; Baglin et al. 2009)—a space mission of French Space Agency and ESA, operating between 2006 and 2013. During its mission, it discovered over 30 planets, most of them of a mass/radius as Jupiter's.

- *Kepler/K2* (Borucki et al., 2010a,b)—a very successfull NASA space mission, divided into *Kepler* part and *K2* part, working from 2009 to 2013 and from 2014 to 2018, respectively. It was working within a wavelength range 430–890 nm. The whole mission discovered more than 2700 exoplanets.

- *TESS* (Transiting Exoplanets Survey Satellite; Ricker et al. 2014)—an extraordinary space project of NASA which has been working since 2018. The spacecraft, which

includes four 10-cm cameras operating within a bandpass range 600–1000 nm, scans almost the entire sky. To date, it has discovered more than 500 exoplanets and over 4600 are yet to be confirmed or refuted.

- *JWST* (James Webb Space Telescope; Gardner et al. 2023)—a successive and complementary mission to Hubble Space Telescope of NASA and therefore it is not solely dedicated to the exoplanetary research. The diameter of the primary mirror is 6.5 m. It was launched at the end of 2021 and it has been fulfilling its scientific goals since the middle of 2022. As the potential of the telescope is really great, exciting details about exoplanetary atmospheres may be expected and some have been already revealed (e.g. Matthews et al., 2024).

There are also some planned important observational projects, both space and ground-based, which are expected to begin to work in this decade:

- ELT (Extremely Large Telescope; Tamai et al. 2022)—an ESO project aimed not only to observe exoplanetary systems. The diameter of the primary mirror is going to be 39.3 m. The telescope is currently under construction and its first light is planned for 2028.

- PLATO (PLAnetary Transits and Oscillations of stars; Rauer & Catala 2012)—an ESA space project with the launch planned for 2026. It is going to consist of 26 telescopes and each of them with a diameter of 12 cm.

  As a ground-based support to this mission, there is going to be a new spectrograph called PLATOSpec[1] mounted on a 1.52-m Chilean telescope of ESO. It is already in operation although it is temporarily using a different spectrograph.

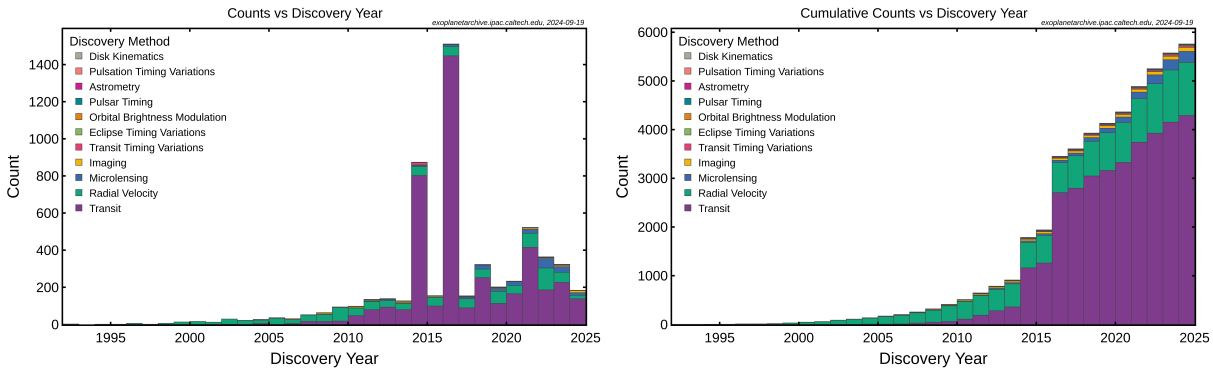

Figure 1: Number of detections of new exoplanets per year (*left*) and number of cumulative detections per year (*right*) as of 26th September 2024, distinguished according to discovery methods. Taken from NASA-Archive.

[1] https://stelweb.asu.cas.cz/plato/index.html

3. Exoplanet atmospheres and methods of their characterisation

As quickly as the field of the exoplanet science develops, the number of exoplanet-discovering and characterising methods increases as well. The first used methods were radial velocity and transit measurements, using spectroscopic and photometric observations, respectively. They are still the most widely used methods but there are others, such as e.g. astrometry, gravitational microlensing, transit timing variations and direct imaging.

The photometric observations are crucial. They do not provide us only information about the size of the measured exoplanet but they can give us valuable information about the atmosphere of the planet. Moreover, when combined with spectroscopic measurements, further details can be unveiled.

As this doctoral thesis is almost entirely based on photometric measurements, the theoretical basis relevant for the thesis and its potential to reveal intriguing atmospheric characteristics of foreign worlds will be described in more detail in this chapter. This will be done with subtle emphasis on atmospheres of hot-Jupiter-type planets.

3.1. Exoplanetary atmospheres

During primary transits, a planet blocks some portion of stellar light. If the planet possesses an atmosphere, a small amount of the light from the star passes through the atmosphere of the planet which can be seen as a thin ring around the planetary body. Moreover, in some moment this planet disappers because it is occulted by its host star. During this event, we observe secondary transits/eclipses or simply occultations. Right before the planet hides behind the observed stellar disc, we are observing a (nearly) full planetary disc. In this moment, we are detecting maximum planetary radiation (but still together with the stellar), no matter what origin it is. An important fact is that the measured planetary flux is generally dependent on the wavelength of the observation since various chemical elements interact differently with photons of different wavelengths. The constraint of the photometric method is that it can be used only if the measured planet is a transiting one. An example of a light curve showing both a transit and an occultation is displayed in Figure 2.

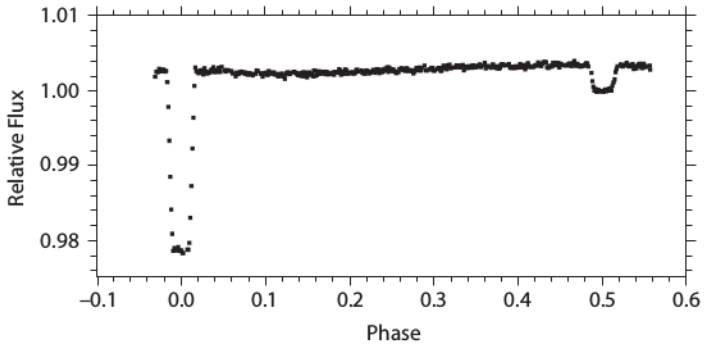

Figure 2: A light curve of exoplanet HD 189733 b with clearly visible transit and occultation at a phase 0.0 and 0.5, respectively, observed at $\lambda = 8\,\mu$m. Taken from Knutson et al. (2007).

3.1.1. Albedos

As previously remarked, one of the measures obtained from occultation observations is reflected light. To describe reflectivity of a celestial body, we use a quantity called *albedo*[2]. The physical meaning in general is that it is the ratio of the light scattered by the body to the light acquired by the body. Furthermore, albedos are frequency and hence also wavelength dependent. It is an important quantity to study atmospheres since a non-zero albedo typically indicates the presence of clouds or hazes, or possibly a reflective surface.

There are a few used types of albedos. These are following:

- single scattering albedo, $\tilde{\omega}(\lambda)$: this albedo is related to a single particle and describes, thus, what fraction of light is scattered by a particle;
- geometric albedo, $A_{\mathrm{g}}(\lambda)$: for full phase, it is the ratio of the flux of a planet to the flux of a Lambert disc[3] which is at the same distance and has the same area;
- spherical albedo, $A_{\mathrm{S}}(\lambda)$: it is the fraction of stellar radiation scattered by the planet into all directions at a specific wavelength;
- Bond albedo, A_{B}: the definition is the same as for A_{S} but it involves radiation at all wavelengths;
- apparent albedo: ratio of the scattered flux by a planet in the direction of the observer to the flux scattered by a perfectly reflecting Lambert sphere of the same properties as of the planet.

In studies of exoplanetary atmospheres, the geometric and Bond albedo are mostly studied. Since atmospheres of majority of the planets investigated in this thesis has not been thoroughly examined yet (or not at all), the geometric albedo for specific wavelengths of each planet will be derived supposing it is qualitatively possible.

The range of possible values is between zero and one from the definitions. However, note that A_{g} is an exception—the definition allows values grater than one and, indeed, some bodies exceed this value, for example Saturn's moon Enceladus with $A_{\mathrm{g}} = 1.38$. This implies that there is no easy way to set an upper limit on the geometric albedo in cases where the analysed data are not enough accurate. On the other hand, to theoretically estimate the contribution of reflected light to the total occultation depth, a greatest A_{g} value is needed to be set. Therefore, $A_{\mathrm{g}} = 1$ is assumed for these occurences. Besides, it is not contradictory to our knowledge about albedos of massive planets which are known to be predominantly low (Angerhausen et al., 2015). This is because atmospheres of hot Jupiters are hot enough that materials to potentially form reflective clouds are in a gaseous form.

The measured flux drop during occultations caused by reflectivity of the planet is the ratio of the planetary flux, F_{p}, to the stellar flux, $F_{\star}$:

$$\frac{F_{\mathrm{p}}}{F_{\star}} = A_{\mathrm{g;p}} \left(\frac{R_{\mathrm{p}}}{a} \right)^2 \Phi(\alpha). \tag{1}$$

Here, R_{p} is the radius of the planet, a is the semi-major axis and $\Phi(\alpha)$ is the phase function, a function of the phase angle α. The phase angle is equal to 0° when the planet is behind its star and it is 180° when the planet transits and is thus not illuminated from our observation point. Although $\alpha = 0°$ means that we do not see the planet, we consider

[2]For the purpose of the thesis it will always be describing a planetary atmosphere.

[3]That is a disc/surface which scatters intensity isotropically.

α to be very close to zero for the purposes described here and as typically used in albedo studies in general. Hence, when putting $\alpha \approx 0°$ into the phase function, we obtain a value of one since $\Phi(\alpha) = [\sin\alpha + (\pi - \alpha)\cos\alpha]/\pi$. Therefore, we may drop using the phase function in further text.

When we change the notation and introduce variable $\delta_{\mathrm{occ,re}}$ as the occultation depth due to reflected light instead of $F_\mathrm{p}/F_\star$ and express the geometric albedo from Equation 1, we get

$$A_\mathrm{g;p} = \delta_{\mathrm{occ,re}} \left(\frac{a}{R_\mathrm{p}}\right)^2. \tag{2}$$

In the thesis, if an upper limit is placed on the geometric albedo, then the occultation depth due to reflected light is substituted by its upper limit. Also, index 'p' standing for 'planet' is either dropped or replaced by 'b' (in tables) since all the studied planets are the first ones discovered in the given systems.

3.1.2. Temperatures

Another crucial quantity to characterise atmopsheres is the temperature—it can vary in all directions in the atmosphere, it changes between hemispheres and with time. Moreover, it drives the state of chemical equilibrium and is thus imprinted in the emergent spectrum.

There are three types of temperatures which are commonly used for exoplanets:

- the effective temperature, T_eff: it is the temperature of a blackbody of the same shape, with the same total flux and at the same distance as the planet is;
- the equilibrium temperature, T_eq: this is the effective temperature of a planet with no internal luminosity;
- the brightness temperature, $T_\mathrm{br}\,(\lambda)$: the definition is the same as for T_eff but for a specific range of wavelengths (frequencies).

Since it is impossible to measure T_eff of exoplanets, T_eq is widely used to describe their atmospheres. Furthermore, T_br is often employed in analyses of atmospheres since only this temperature is really measurable for exoplanets.

The equilibrium temperature of an exoplanet is estimated as

$$T_\mathrm{eq;p} = T_{\mathrm{eff};\star}\sqrt{\frac{R_\star}{a}}\sqrt[4]{f(1 - A_\mathrm{B})}, \tag{3}$$

where $T_{\mathrm{eff};\star}$ is the stellar effective temperature, $R_\star$ is the stellar radius, A_B is the Bond albedo and f is a heat redistribution factor which will be discussed in the following subchapter.

The advantage of the brightness temperature is that only one observation in a specific wavelength range is needed to obtain it. Note that measuring the brightness temperature supposes that the studied planet behaves as a blackbody only in the wavelength range where the flux is measured. Planetary spectra can significantly depart from a blackbody. Hence, T_br can vary extensively with wavelength/frequency.

Using the derived occultation depth, δ_occ, the brightness temperature is calculated applying this equation:

$$\int_\lambda B_\lambda(T_\mathrm{br;p})\,\mathrm{d}\lambda = \delta_\mathrm{occ}\left(\frac{R_\star}{R_\mathrm{p}}\right)^2 \int_\lambda B_\lambda(T_{\mathrm{eff};\star})\,\mathrm{d}\lambda. \tag{4}$$

As the stellar temperature the effective temperature is used and B_λ is the wavelength-dependent Planck function:

$$B_\lambda(T) = \frac{2hc^2}{\lambda^5} \frac{1}{e^{(hc/\lambda k_B T)} - 1}, \tag{5}$$

where λ is the wavelength and T is the temperature at which we calculate the function, and h, c and k_B are the Planck constant, the speed of light and the Boltzmann constant, respectively.

The procedure to obtain $T_{br;b}$ is following: the integral (related to the star) on the right-hand side of Equation 4 is solved and then multiplied by the occultation depth and the star-to-planet area ratio. The obtained value is stored. Subsequently, the left-hand side (related to the planet) of the equation is solved. It is integrated numerically—iteratively by putting successively increasing numbers until the value of the right-hand side corresponding to the planetary brightness temperature is reached.

3.1.3. Heat redistribution

In the description of the equilibrium temperature the heat redistribution factor, f, was introduced. It is used so that T_{eq} from only one hemisphere could be described as this is what we can always observe at a time.

For cases when the stellar radiation absorbed by the planet is uniformly redistributed around the whole planet, $f = 1/4$. However, if the radiation absorbed by one hemisphere is instantaneously reradiated instead of uniform redistribution, then $f = 2/3$. This is asserted for slowly rotating planets or planets tidally locked to the host stars. The case of $f = 2/3$ implies that the dayside is hotter than the nightside.

To calculate the heat redistribution factor, f is expressed from Equation 3 and $T_{eq;p}$ is substituted with priorly deduced $T_{br;p}$:

$$f = (1 - A_B)^{-1} \left(\frac{a}{R_\star}\right)^2 \left(\frac{T_{br;p}}{T_{eff;\star}}\right)^4. \tag{6}$$

3.2. Occultation spectroscopy

The radiation of a planet is the sum of its thermal emission and the reflected light. These two measures are independent. Typically, strong thermal radiation usually means low albedo and vice versa. But it is not a general rule.

Since planets are cooler than stars, the thermal-radiation component becomes prevalently apparent at different, longer, wavelegths than the reflected-light component. In other words, the thermal emission is obtained from (near-) infrared measurements whilst the reflected light (albedo) is obtained from data in the optical/visible band. Observations of the thermal emission provide valuable information about thermal structures, transport of energy, chemical composition etc. In turn, optical measurements provide knowledge about physical properties of the atmosphere and about the presence of clouds/hazes by which albedos are strongly influenced. Furthermore, whilst the reflected light comes from the top of the atmosphere, the thermal radiation emerges in bigger depths.

If the transit depth of a studied planet together with $T_{eff;\star}$, $R_\star$ and a (to obtain $T_{eq;p}$) are already known from previous measurements, by approximating the star and the planet to radiate as blackbodies the occultation depth due to the thermal emission can be estimated as

$$\delta_{\mathrm{occ,th}} = \left(\frac{R_{\mathrm{p}}}{R_{\star}}\right)^2 \frac{B_{\lambda}(T_{\mathrm{eq;p}})}{B_{\lambda}(T_{\mathrm{eff;}\star})}. \tag{7}$$

An estimate of the contribution of the reflected light to the overall occultation depth can be obtained by knowing R_{p}, a and A_{g}. In cases when the geometric albedo is unknown, it has to be estimated. As the highest A_{g} a value of one is commonly placed but for hot Jupiters a lower value is more appropriate.

By re-arranging the terms in Equation 2 we obtain the reflected-light contribution to the occultation depth,

$$\delta_{\mathrm{occ,re}} = A_{\mathrm{g}} \left(\frac{R_{\mathrm{p}}}{a}\right)^2. \tag{8}$$

More details about methods, derivation of equations related to atmospheres etc. can be found in literature, e.g. Seager (2010a,b).

4. The VLT and TESS photometric data

The photometric data sets of the selected planetary systems have been analysed for the purpose to detect occultations of the studied planets and to derive above-mentioned atmospheric characteristics from those occultations depths. In cases where the occultations were clearly detected the depth for the specific wavelength (used filter) was used as an additional data point to compute a model of the atmospheric emission spectrum of the given planet. This does not concern, however, planets with the only occultation detection.

The occultation data studied further were obtained by using three different facilities: space-based *TESS* in the optical band, ground-based ESO VLT FORS2 in the visible/near-infrared band and also ground-based ESO VLT HAWK-I in the near-infrared band. Furthermore, in one case data of ESO VLT UVES spectrograph were used as complementary data to better constrain orbital parameters.

4.1. Target selection

The targets were observed for their expected large occultation depth and, thus, studying atmospheres of the planets of these systems, in addition belonging into two groups—ultra-hot ones and cooler ones. The targets were discovered by two ground-based surveys: Wide Angle Search for Planets (WASP; Pollacco et al. 2006) and Optical Gravitational Lensing Experiment (OGLE; Udalski et al. 1992), particularly its second phase, OGLE-2 (Udalski et al., 1997). The individual data sets were selected as unpublished data except one, chosen for a comparison of different methods of data analysis.

The described and analysed data sets in this thesis include these exoplanetary systems: WASP-18, WASP-36, WASP-43, WASP-50, WASP-51 (corresponding to HAT-P-30) and OGLE2-TR-L9. It is notable that some targets involve more data sets per each instrument as they were observed more times or/and by using different filters.

As the first, the ESO VLT data were obtained—they were downloaded from ESO Science Archive Facility[4]. Next, data of the same targets were obtained by *TESS*—these were downloaded from Mikulski Archive for Space Telescopes[5] (MAST).

Table 1 shows observing properties of the parent stars of the studied systems.

Table 1: Properties relevant to observe the parent stars of the studied systems. The right ascension and the declination are given together with apparent magnitudes in K and *TESS* filters as well as the spectral type. Taken from Simbad and MAST. *Note*: $^{(a)}$: given in J filter.

System	RA [α]	DEC [δ]	m_{K} (mag)	m_{TESS} (mag)	Sp. type
WASP-18	$01^{\mathrm{h}}37^{\mathrm{m}}25^{\mathrm{s}}$	$-45°40'40''$	8.13	8.83	F6V
WASP-36	$08^{\mathrm{h}}46^{\mathrm{m}}20^{\mathrm{s}}$	$-08°01'37''$	11.29	12.15	G2
WASP-43	$10^{\mathrm{h}}19^{\mathrm{m}}38^{\mathrm{s}}$	$-09°48'23''$	9.27	11.02	K7V
WASP-50	$02^{\mathrm{h}}54^{\mathrm{m}}45^{\mathrm{s}}$	$-10°53'53''$	9.97	11.01	G9V
WASP-51	$08^{\mathrm{h}}15^{\mathrm{m}}48^{\mathrm{s}}$	$+05°50'12''$	9.15	9.91	G0
OGLE2-TR-L9	$11^{\mathrm{h}}07^{\mathrm{m}}55^{\mathrm{s}}$	$-61°08'47''$	$13.51^{(a)}$	14.07	F3V

[4] http://archive.eso.org/eso/eso_archive_main.html
[5] https://mast.stsci.edu

4.2. Instruments used to acquire the data sets

4.2.1. HAWK-I

The instrument used for taking most of the near-infrared images was High Acuity Wide-field K-band Imager[6] (HAWK-I; Pirard et al. 2004, Casali et al. 2006, Kissler-Patig et al. 2008, Siebenmorgen et al. 2011). The instrument is mounted on UT4 of the Very Large Telescope which is operated by the European Southern Observatory.

HAWK-I is composed of four detectors into a square and each of them has resolution of 2048×2048 px with the field of view of $7.5' \times 7.5'$. One pixel on the detector corresponds to $0.106''$ on the sky. The instrument is cooled down to 80 K (low dark current) and works in a wavelength range 0.85 µm–2.5 µm. HAWK-I hosts ten various filters. Four of them are broad: Y, J, H, K; and the six remaining are narrow band filters: Bracket γ, CH_4, H_2, NB1060, NB1190 and NB2090. The last three ones have been used to acquire the data sets analysed in this thesis. The wavelength ranges of their transmission are 1057–1066, 1180–1192 and 2085–2105 nm with central wavelengths of 1061, 1186 and 2095 nm, respectively. The HAWK-I filters are graphically displayed in Figure 3.

Besides standard readout modes (such as Generic Offset Mode), HAWK-I can also obtain data using Fast Photometry Mode (FPM). This mode allows to get a huge number of images during a single night (up to tens of thousands). Fast read-out (high cadence of images) is reached due to smaller resulting size of an image because not the whole detectors are read in FPM. Every detector can be read in horizontal and vertical stripes which are set by the observer before the planned observation. After a certain number of images is reached, they are stacked on top of each other and a 'cube' of these images (cube `fits` file) is created. In this manner 3D files containing usual `fits` images are the output of FPM of HAWK-I. Examples of two science images obtained using two different modes are shown in Figure 4.

4.2.2. FORS2

The second ground-based instrument is FOcal Reducer and low dispersion Spectrograph 2[7] (FORS2; Appenzeller et al. 1998). The instrument is mounted on UT1 of the Very Large Telescope of the European Southern Observatory.

FORS2 allows observations in regimes of imaging, spectroscopy and polarimetry. It is a successor of FORS1 which was dismounted in 2009. FORS2 is composed of two detectors with resolution of 2000×4000 px per each detector. The field of view of the instrument is $7.1' \times 7.1'$ (when the standard resolution collimator is used). The pixel scale is $0.25''$, $0.125''$, or $0.0632''$ per pixel depending on the chosen resolution and binning. FORS2 works between 330 and 1100 nm and uses seven broadband filters for the imaging mode. To acquire data analysed in this thesis a standard broad z-band filter, z_GUNN+78, was used. Its central wavelength is at 910 nm.

The wavelength coverage of the filters as the function of their transmission is shown in Figure 5. An example of an image obtained by the imaging mode is shown in Figure 6.

4.2.3. *TESS*

The last instrument used to acquire the further analysed data is Transiting Exoplanets Survey Satellite—*TESS* (Ricker et al., 2014). It is a space mission led by NASA which has been working since 2018. The mission is aimed to measure brightness of hundreds of

[6] https://www.eso.org/sci/facilities/paranal/instruments/hawki.html
[7] https://www.eso.org/sci/facilities/paranal/instruments/fors.html

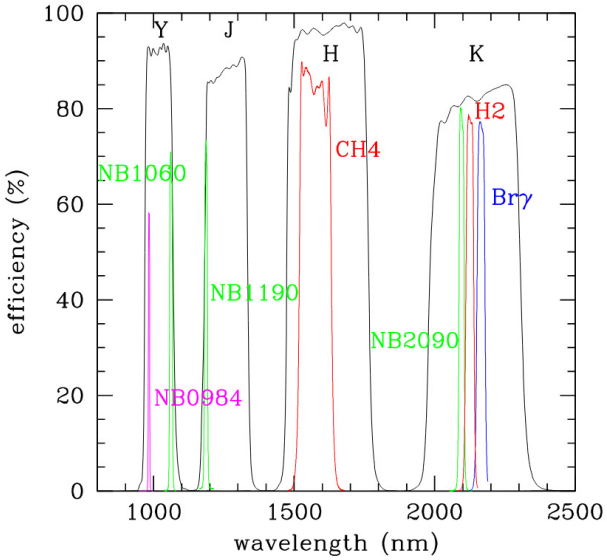

Figure 3: Efficiency/transmittance of the HAWK-I narrow-band filters compared to other near-infrared ones. Taken from ESO HAWK-I manual.

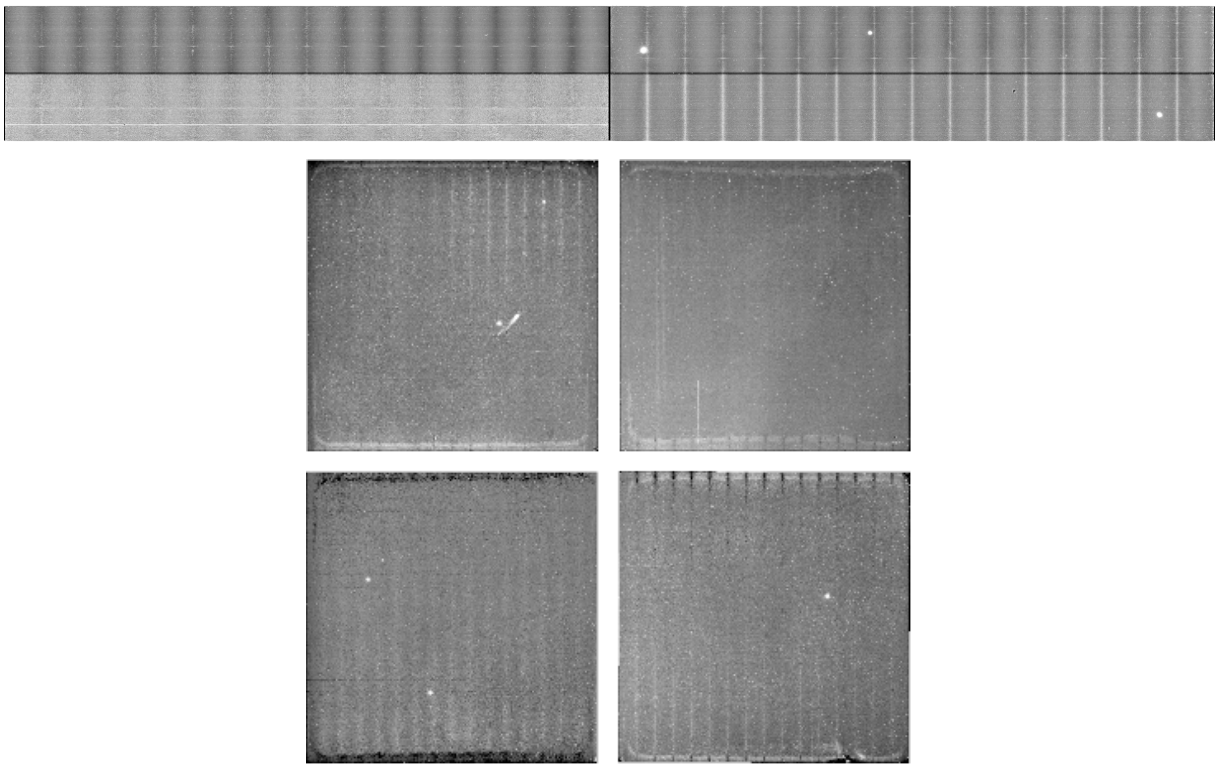

Figure 4: Examples of HAWK-I raw science images taken through NB2090 filter. *Top:* WASP-18 using Fast Photometry Mode; *bottom:* WASP-43 using Generic Offset Mode.

thousands of stars and seek for transits. Since *TESS* target stars are much brighter than stars observed by cameras onboard *Kepler* mission, it is easier to characterise the targets with follow-up ground observations.

The instrument itself consists of four cameras, each with a pupil diameter of 10.5 cm and the field of view of 24° × 24° where every camera consists of four CCDs giving in total an imaging array of 4096 × 4096 px. The readout noise is lower than 10 e^- and all the CCDs are being kept at a temperature of −75 °C which reduces the dark current to a level where it can be neglected. The *TESS* cameras work between 600 and 1000 nm

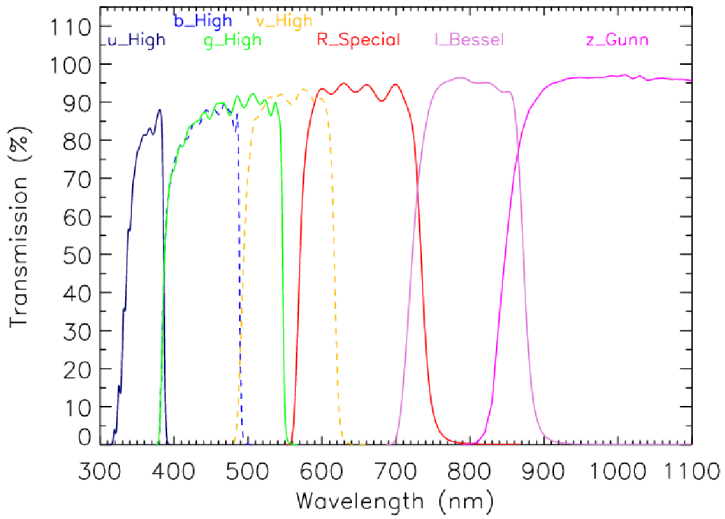

Figure 5: Transmission and wavelength coverage of FORS2 standard broadband filters. Taken from ESO FORS2 manual.

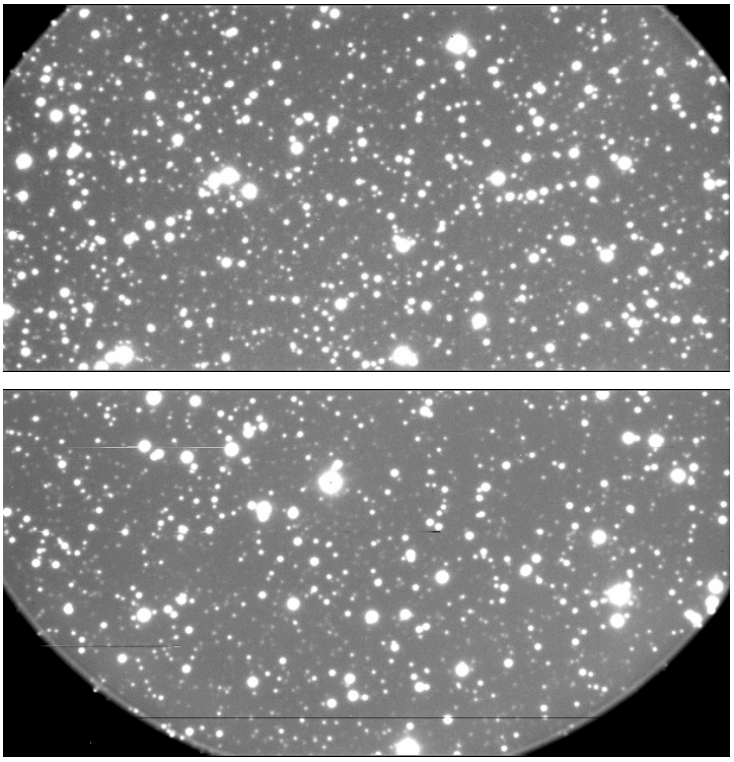

Figure 6: An example of a FORS2 raw science image taken through z_GUNN+78 broadband filter during an observation of OGLE2-TR-L9. The top image is obtained by detector 1 whilst the bottom one by detector 2.

and are centred at 786.5 nm, see Figure 7. Thus, they cover the visible red and the near-infrared bandpass. The continuous stream of 2-second integrations of the cameras results in 2-minute postage stamps of Target Pixel Files and 30-minute Full-Frame Images. All the images of the *TESS* data sets analysed in this thesis have been taken with a 2-minute cadence.

If a user wants to have control over the data, the rawest form of the data, Target Pixel Files are the solution and the user may perform own aperture photometry. Hence, very detailed analysis of studied targets can be done. On the other hand, if this is not required,

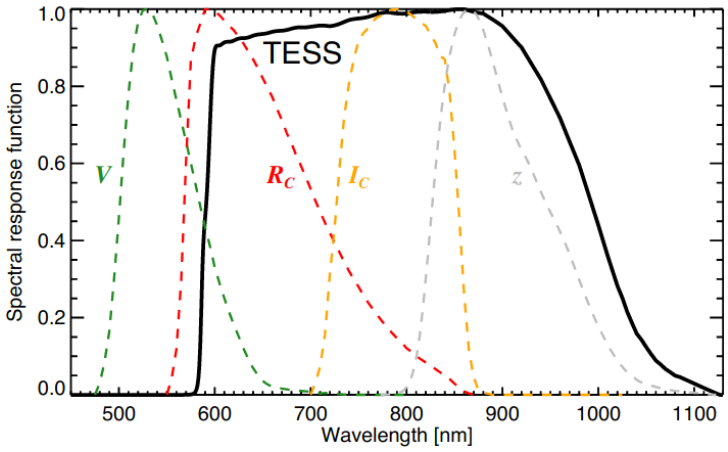

Figure 7: Spectral response function of *TESS* filter compared to Johnson-Cousins and SDSS filter curves. Taken from Ricker et al. (2014).

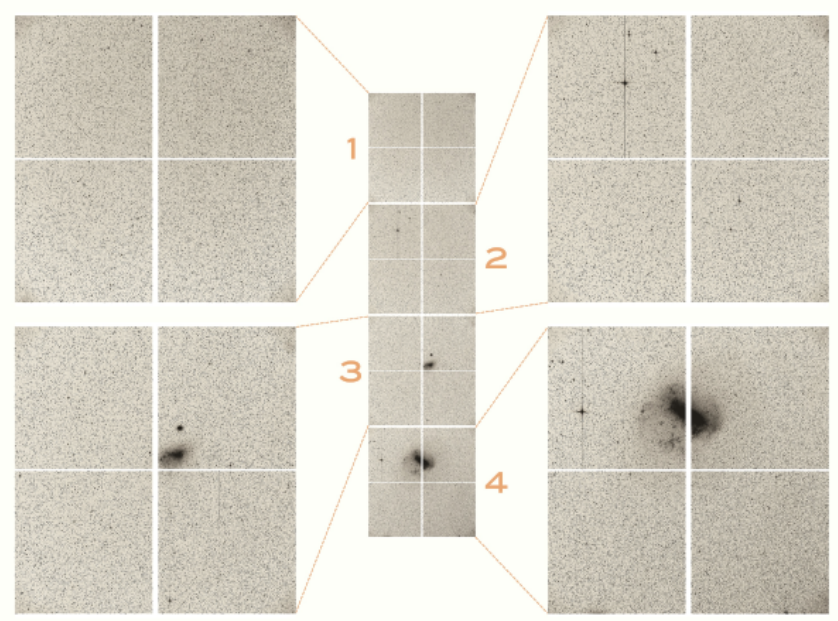

Figure 8: The first image obtained by *TESS* (inverted) with the Small and Large Magellanic Cloud clearly visible. In the middle, the arrangement of the images corresponds to the original arrangement of the four cameras with the field of view of 24° × 96°. Credit: NASA/MIT/TESS.

there is a *TESS* pipeline developed by the Science Processing Operations Center at NASA Ames Research Center. It results in various outputs where one of often used types is Presearch Data Conditioned Simple Aperture Photometry Flux (PDCSAP_FLUX; Smith et al. 2012a, Stumpe et al. 2012, Jenkins et al. 2016). On this data type, used in analyses in this thesis, aperture photometry has been already performed as well as long-term trends have been removed.

The processed data obtained by *TESS* are then archived at Mikulski Archive for Space Telescopes. An example of an image acquired by *TESS* is shown in Figure 8.

4.3. Software used to process and analyse the data sets

4.3.1. HAWK-I pipeline

To reduce and process data sets acquired by HAWK-I instrument a simple pipeline was applied. This was developed mainly for Fast Photometry Mode of HAWK-I because no software to reduce FPM data has been available and most HAWK-I data in this thesis were obtained using FPM. Such software requires working with cube `fits` files produced by FPM and adapting calibration frames allowing then to perform data reduction.

To create this pipeline, several software packages have been used: Image Reduction and Analysis Facility (IRAF; Tody 1986, 1993), Python programming language (Van Rossum & Drake, 2009) and Python library PyRAF (Science Software Branch at STScI, 2012). The pipeline consists of a few Python scripts using IRAF commands, each of them executing different tasks, such as data reduction, photometry, light curve settings and plotting, and others. The pipeline is described in more detail in Blažek (2017) master thesis.

The HAWK-I data in this thesis are reduced by a standard way including division by a normalised master flat-field frame. Since dark current (at 75 K) of HAWK-I is less than 0.01 e/s/pix, dark frames are not used for the data reduction although this step is included in the pipeline. After the data reduction differential aperture photometry is performed. At the end, a light curve both as a plot and as a text file are created.

4.3.2. allesfitter

To analyse the data of transits, occultations and radial velocity described in the following sections, allesfitter[8] (Günther & Daylan 2019, 2021) software package was used. It is a Python open-source code which was developed to model photometric and radial velocity (RV) data. It allows modelling of multiple exoplanet systems, multiple star systems, star spots and stellar flares.

To model noise, various baseline models are included in the package. In this thesis, GP Matérn 3/2 kernel is used to model the correlated noise. This particular kernel is selected from a few possible ones since it is strongly favoured over other kernels as found by Günther & Daylan (2021). The corresponding parameters of Matérn 3/2 are the height scale (amplitude) and the length scale, denoted within the package as σ and ρ, respectively.

To take samples from the posterior of the chosen model, Markov Chain Monte Carlo (MCMC) or Nested Sampling inference algorithm (NS) can be chosen by the user. The latter has the advantage that it computes the Bayesian evidence ($\ln \mathcal{Z}$) for the selected model given the observed data. Hence, it allows us to compare different physical models which we used to fit for our data. Moreover, NS ensures that all convergence criteria are fulfilled.

As a photometry input data file, a `csv` text file is used and this must include three columns: time in days, normalised flux and the uncertainty of the flux. For radial velocity data these are time in days, radial velocity in $\mathrm{km\,s^{-1}}$ and the instrumental error of the RV in $\mathrm{km\,s^{-1}}$. It is also necessary to create input files where all settings of the intended fit are stored and where all needed parameters together with their prior estimates are given. Another file, providing stellar mass, radius and temperature, is optional. The output involves plots, LaTeX and ASCII tables of the fitted and derived parameters, and others. A detailed description of allesfitter including examples of its usage is provided in Günther & Daylan (2021).

[8] https://www.allesfitter.com

4.4. Observational constraints and post-processing

4.4.1. Effects affecting data, data quality evaluation

When we are doing an observation from the ground, the measured light from our target—after it travelled a long undisturbed distance—reaches the Earth's atmosphere which influences the behaviour of the light until it hits our detector. There are several effects originating from the atmosphere itself which generally hamper our observations.

Seeing (measured in arcseconds) is blurring of an image which can lead to breaking the image up into speckles. These changes can be occuring very rapidly with time. Thus, the observed light source may exhibit fluctuations in its brightness during our measurement. The effect originates in random distortion of the wavefront which is a result of atmospheric turbulence. Although it can be compensated by adaptive optics, it can not be removed completely to get an image as obtained outside the atmosphere.

Coherence time (measured usually in milliseconds), τ_0, is closely connected with seeing as it describes the turbulence evolution in the unit of its characteristic time. The coherence time is a function of wavelength and the average turbulent velocity. The less turbulent atmosphere implies longer τ_0 which improves our results of the observation.

Airmass (dimensionless), X, describes the amount of air which light from the observed target is going through. In other words, objects in the zenith have the lowest possible airmass value, one, and towards the horizon it increases as the amount of air mass do. It can be estimated as $X = \sec z = 1/\cos z$, where z is the angular distance of the object from the zenith on the sphere. This means that the best observational position of an object is in the zenith whilst observing close to the horizon does not usually lead to high-quality data.

Unlike the above discussed effects coming into consideration only for ground-based observations, there two main types of noise present in both ground-based and space-based surveys.

Red noise, or 'time-correlated noise', is a designation for systematics in our time-series data. It can be recognised as random brightness fluctuations of an astrophysical source. The level of the red noise raises with decreasing frequency—for infrared observations, crucial for atmospheric characterisations, it can be an obstacle to get meaningful results from our infrared data. There are various sources of the red noise such as those mentioned above. To restrain the effect of red noise and to gain our probability to detect a real astrophysical signal, we use models to describe the red-noise variations when fitting our data (e.g. Pont et al., 2006). The model is eventually subtracted from the fit.

White noise is always present in any data. This noise is uncorrelated in time and in astronomy it is also known as 'photon noise'. It simply comes from the fact that we do not measure the same number of photons (i.e. our signal) for each of our entirely same measurements of the same integration time. This is given by characteristics of photons—they arrive at random, each reaching the detector independent of other photons. There is a rule describing the photon noise and its relation to the measured signal: $\bar{x} \pm \sqrt{\bar{x}}$, where $\bar{x}$ is the average number of photons and $\sqrt{\bar{x}}$ is thus the standard deviation of the measurement following the normal distribution.

Signal-to-noise ratio (SNR) is used to numerically evaluate the quality of our signal. If we consider the photon noise as the primary source of noise, then the SNR is the signal divided by the noise. Using the notation of the white noise description, we may write $\mathrm{SNR} = \bar{x}/\sqrt{\bar{x}} = \sqrt{\bar{x}}$. We can see that a greater signal leads to a greater signal-to-noise ratio and this is what we need. One way to increase the SNR is to set the exposure time as long as possible (but keeping the capabilities of the detector).

4.4.2. Post processing

Binning is another way to increase the SNR of our time-series science images which is a part of post-processing of the acquired images. We do this by summing a selected number of science images and taking an average value of the obtained signal. Although this operation results in raising both the signal and the noise, the gain of the signal is dominant. The signal-to-noise ratio of N images is expressed as $\mathrm{SNR}_N = N\bar{x}/\sqrt{N\bar{x}} = \sqrt{N\bar{x}}$. This indicates that the SNR of N images increases the total signal-to-noise ratio by a factor of $\sqrt{N}$ when compared to the SNR of a single image. There is another merit of binning. Since it leads to a lower number of images than without binning, the data processing is, thus, computationally favourable in terms of the needed time.

Bad pixel mask (BPM) should be used if some pixels of the used detector do not respond linearly which misrepresents the real measured signal. Generally, pixels not responding properly can be 'hot' or 'dead' pixels. Creating a BPM consists in replacing a bad pixel by the median value of the surrounding pixels. To generate a BPM flat-field frames with low and high levels of intensity are applied and then the ratio of those two types is derived to identify the bad pixels.

4.4.3. Statistics of data sets

The analysed data sets in the subsequent sections also include their statistical parts. Each of them serves as an quantifier of the quality of the data set.

For every data set the weighted standard deviation, σ_w, has been calculated, following this commonly used formula:

$$\sigma_\mathrm{w} = \sqrt{\frac{\sum_{i=1}^{N} w_i(x_i - \overline{x}_\mathrm{w})}{\sum_{i=1}^{N} w_i}}, \tag{9}$$

where N is the number of data points (observations), $w_i = 1/\sigma_i^2$ is the weight of the i^{th} data point of the value x_i measured with the uncertainty σ_i, and $\overline{x}_\mathrm{w} = \Sigma_{i=1}^{N} x_i w_i / \Sigma_{i=1}^{N} w_i$ is the weighted mean.

In astronomy, when statistically describing quality of a data set using the standard deviation 'RMS' initialism, meaning 'Root Mean Square', is usually used. This designation is also used in this thesis together with its form 'RMS_w' denoting to 'Weighted Root Mean Square'. The reason for this is especially to avoid confusion with other meanings of 'σ', e.g. with parameters describing noise.

4.5. Description and analysis of the data sets

To theoretically estimate if the occultation can be detected in the data, RMS_w (Equation 9) of each analysed data set and the theoretical expected depth for the investigated planet given the wavelength of observation were compared. The expected occultation depth was calculated as the sum of thermal emission (Equation 7) and reflected light (Equation 8). The former differs for various wavelength ranges whilst the latter is the same for all bandpasses. For the estimates here, the thermal radiation was assumed to have a form of a blackbody and for the reflected light the geometric albedo was supposed to be equal to 1 or 0.1.

The RMS_w was obtained applying different approaches. For the *TESS* data unbinned and binned data were used as well as arbitrarily chosen time intervals on which the RMS_w

was calculated too. For the ground-based data, unbinned and binned data were also used but including all or only out-of-occultation data points. By exluding the points spanning the occultation event the RMS_w should markedly decrease. If it does not, the noise is stronger than the depth of the occultation or possibly the supposed time of the occultation event is incorrect.

Physical and orbital characteristics of all the studied planetary systems are summarised in Table 2.

4.5.1. Data reduction and fitting

The *TESS* data have already been reduced and processed by a *TESS* pipeline as described in Section 4.2.3. The HAWK-I data were reduced and photometry performed using own pipeline, see Section 4.3.1. A part of this pipeline together with EsoReflex[9] environment of ESO (Freudling et al., 2013) were used to reduce the FORS2 data set (OGLE-9).

To fit the data, stellar priors were used involving the effective temperature, the radius and the mass. Furthermore, the stellar metallicity and the logarithm of the surface gravity were used to obtain the limb darkening coefficients (where relevant). These were derived from the quadratic model of PyLDTk software package of Parviainen & Aigrain (2015) using the spectrum library of Husser et al. (2013). The expected occultation depth was used as the initial value of the surface brightness ratio, the white and red noise parameters were estimated from the data, and the baseline offset and the phase curve modulators were initially set to zero. The initial values of the remaining measures were adopted from the published works as in Table 2. Uniform or normal prior bounds were set to the fitted parameters.

All the light curves were fitted by allesfitter software (Section 4.3.2) applying Matérn 3/2 kernel to deal with red noise unless explicitly mentioned. To sample from the posteriors, Nested Sampling inference algorithm was used. The fits of the binned ground-based data were performed ten times. For further analysis, that one with the highest $\ln \mathcal{Z}$ was selected. The only derived parameter obtained from the ground-based data was the occultation depth, δ_{occ}.

[9] http://www.eso.org/sci/software/esoreflex

Table 2: Physical characteristics of all the systems studied in this thesis, taken from literature. The mean planetary density is obtained from the values of R_b and M_b. *References*: $^{(a)}$: Cortés-Zuleta et al. (2020), $^{(b)}$: Shporer et al. (2019), $^{(c)}$: Nymeyer et al. (2011), $^{(d)}$: Smith et al. (2012b), $^{(e)}$: Mancini et al. (2016), $^{(f)}$: Maciejewski et al. (2016), $^{(g)}$: Chen et al. (2014), $^{(h)}$: Gillon et al. (2012), $^{(i)}$: Gillon et al. (2011), $^{(j)}$: Tregloan-Reed & Southworth (2013), $^{(k)}$: Sada et al. (2012), $^{(l)}$: Johnson et al. (2011), $^{(m)}$: Enoch et al. (2011), $^{(n)}$: Snellen et al. (2009), $^{(o)}$: Southworth (2010).

	WASP-18	WASP-36	WASP-43	WASP-50	WASP-51	OGLE-9
Discovery article	Hellier et al. 2009	Smith et al. 2012b	Hellier et al. 2011	Gillon et al. 2011	Johnson et al. 2011	Snellen et al. 2009
Parameter (Unit)	*Stellar parameters*					
Effective temperature, $T_{\mathrm{eff};\star}$ (K)	$6432 \pm 48^{(a)}$	$5959 \pm 134^{(d)}$	$4536^{+98\,(g)}_{-85}$	$5400 \pm 100^{(i)}$	$6304 \pm 88^{(l)}$	$6933 \pm 58^{(n)}$
Radius, $R_\star$ ($\mathrm{R}_\odot$)	$1.319^{+0.061\,(a)}_{-0.062}$	$0.985 \pm 0.012^{(e)}$	$0.660^{+0.008\,(g)}_{-0.009}$	$0.855 \pm 0.018^{(j)}$	$1.330 \pm 0.030^{(m)}$	$1.503 \pm 0.083^{(o)}$
Mass, $M_\star$ ($\mathrm{M}_\odot$)	$1.294^{+0.063\,(a)}_{-0.061}$	$1.081 \pm 0.025^{(e)}$	$0.713^{+0.018\,(g)}_{-0.021}$	$0.861 \pm 0.052^{(j)}$	$1.180 \pm 0.030^{(m)}$	$1.520 \pm 0.080^{(n)}$
Logarithm of the surface gravity, $\log g_\star$ (cgs)	$4.310^{+0.036\,(a)}_{-0.033}$	$4.486 \pm 0.009^{(e)}$	$4.652 \pm 0.006^{(g)}$	$4.509 \pm 0.012^{(j)}$	$4.260 \pm 0.010^{(m)}$	$4.236 \pm 0.043^{(o)}$
Metallicity, [Fe/H] (dex)	$0.11 \pm 0.08^{(a)}$	$-0.26 \pm 0.10^{(d)}$	$0.01^{+0.10\,(g)}_{-0.09}$	$-0.12 \pm 0.08^{(i)}$	$-0.08 \pm 0.08^{(m)}$	$-0.05 \pm 0.20^{(n)}$
Parameter (Unit)	*Orbital and planetary parameters*					
Radius, R_b (R_J)	$1.191 \pm 0.038^{(b)}$	$1.327 \pm 0.019^{(e)}$	$1.034 \pm 0.014^{(g)}$	$1.138 \pm 0.024^{(j)}$	$1.420 \pm 0.030^{(m)}$	$1.614 \pm 0.083^{(o)}$
Mass, M_b (M_J)	$10.200 \pm 0.350^{(a)}$	$2.361 \pm 0.062^{(e)}$	$2.029^{+0.035\,(g)}_{-0.040}$	$1.437 \pm 0.063^{(j)}$	$0.711 \pm 0.028^{(l)}$	$4.340 \pm 1.470^{(o)}$
Mean density, $\bar{\rho}_\mathrm{b}$ ($\mathrm{kg\,m^{-3}}$)	7487 ± 137	1253 ± 49	2276 ± 35	1209 ± 60	308 ± 72	1280 ± 476
Orbital period, P_b (d)	$0.941\,452\,6\,(16)^{(b)}$	$1.537\,365\,3\,(26)^{(d)}$	$0.813\,474\,37\,(13)^{(g)}$	$1.955\,090\,5\,(22)^{(k)}$	$2.810\,595\,(5)^{(l)}$	$2.485\,533\,5\,(7)^{(o)}$
Semi-major axis, a_b (AU)	$0.020\,24\,(31)^{(a)}$	$0.026\,43\,(26)^{(d)}$	$0.015\,26\,(18)^{(h)}$	$0.029\,13\,(59)^{(j)}$	$0.041\,18\,(31)^{(m)}$	$0.0404 \pm 0.0011^{(o)}$
Inclination of the orbit, i_b (deg)	$84.88 \pm 0.33^{(b)}$	$83.61 \pm 0.21^{(d)}$	$82.64 \pm 0.19^{(g)}$	$84.74 \pm 0.24^{(i)}$	$82.48^{+0.16\,(m)}_{-0.15}$	$82.07 \pm 0.69^{(o)}$
Orbital eccentricity, e_b	$0.0091 \pm 0.0012^{(c)}$	$0^{(f)}$	$< 0.0298^{(h)}$	$0.009^{+0.011\,(i)}_{-0.006}$	$0.035 \pm 0.024^{(l)}$	$\approx 0^{(n)}$
Argument of periastron, ω_b (deg)	$269 \pm 3^{(c)}$	—	$-32^{+115\,(h)}_{-34}$	$44^{+62\,(i)}_{-80}$	$252 \pm 84^{(l)}$	—

5. Strategy of measurements of exoplanetary atmospheres

The first part of the data analysis involves data sets where no clear occultation detection was reached although the systems were observed during occultations. Nevertheless, analysing of such data can still lead to reasonable and also usable results for future planning of observing strategies. We usually claim a non-detection if the measured quantity is obtained at less than 3σ significance (i.e. the value itself is at least three times the uncertainty). For such cases an upper limit may be placed and a 3σ limit is usually used to trust the obtained result—it means that there is a 99.73-% probability in the normal distribution that the real value really lies below the placed upper limit (in some works 2σ limits are placed, corresponding to a 95.45-% probability). This strategy is used in the analyses of the data described in this section. The derived 3σ upper limits on the occultation depth are in turn used to place upper limits on the geometric albedo, the brightness temperature and the heat redistribution factor.

Table 3 shows properties of the science frames of all the described data sets in numbers. All important measures of the observations together with the obtained differential light curves are plotted in Figure 9, the *TESS* raw light curves are shown in Figure 10 whilst the binned ground-based light curves are shown in Figure 11.

5.1. The data sets

WASP-18 b, HAWK-I

There are two HAWK-I data sets which were obtained by using FPM through NB1060 and NB2090 filters. They were obtained during an observational night on 21st September 2013 (JD = 2,456,557) and on 2nd August 2013 (JD = 2,456,506), respectively. Two comparison stars were observed together with the target star, the same in both the cases.

NB1060: During the observation of the target, most of the night the star was rising on the sky. As for the target position on the detector, it was rather stable both in X and Y axis, in a range of roughly ten pixels. However, values of seeing and coherence time were unsubtly changing and having, thus, a strong effect on the measured flux. As seen in the plots, the variation of seeing copies the light curve showing strong dependence of these two measures.

NB2090: Most of the observational night the target star was rising on the sky. There were significant changes of coherence time and hence also changes of seeing—these had an apparent effect on the measured flux. The target position on the detector was again varying in a range of ten pixels with occasional higher 'jumps' from the mean point. To decrease the size of images and get shorter read-out time, the original positions of the measured stars on the detector were changed (by slight rotation of the detector). The adjustement caused a short observational break between BJD 0.74 and 0.75 d.

The data reduction and differential aperture photometry of both the data sets were performed as described in Section 4.5.1 and using the same comparison star—that one with more stable flux.

WASP-36 b, HAWK-I/NB2090

The data set was obtained during an observational night on 30$^{\text{th}}$ December 2011 (JD = 2,455,925), by using FPM of HAWK-I through filter NB2090. Three comparison stars of similar brightness to the target star were observed together with it.

The target star was rising on the sky the first two thirds of the observation night and almost reached the zenith. Coherence time was strongly varying in the first quarter. Similarly, seeing variance was significant reaching a range of almost three arcseconds but in the first quarter it was low and stable. Positions of the target star on the detector were mostly in a range of seven pixels both for X and Y axis. In about a half of the observation, there were shifts in the positions on both the axes but without an obvious effect on the resulting data, as opposed to the seeing variance.

WASP-43 b, HAWK-I/NB1060

The data set was obtained during an observational night on 30$^{\text{th}}$ January 2014 (JD = 2,456,687) by using FPM of HAWK-I through filter NB1060. Two comparison stars together with the target star were observed. From an unknown reason the observation terminated roughly an hour after it began, in the first third of the occultation event.

The target was rising on the sky during the whole observation. Coherence time was changing in a more plausible range than in the previous HAWK-I data sets. Likewise, variances of seeing were not so strong but reaching relatively high values up to two arcseconds. Positions of the star on the detector were stable within a range of eight and six pixels for X and Y axis, respectively. There were some exceptions exceeding this range which seems to have an effect on the resulting light curve, e.g. between 0.647–0.648 d.

WASP-50 b, HAWK-I/NB2090

The data set was obtained during an observational night on 6$^{\text{th}}$ December 2011 (JD = 2,455,901), by using FPM of HAWK-I through filter NB2090. Two comparison stars were observed together with the target star.

Most of the observational time the target was setting down from almost the zenith position. In the first half coherence time and seeing were strongly varying but in the second half the situation improved. Positions of the target star on the detector were stable within a range of nine and eleven pixels for X and Y axis, respectively. These variations had an effect on the resulting light curve in time range 0.60–0.61 d. This is, nevertheless, relatively far before the occultation begins and it did not affect the baseline of the light curve.

WASP-51 b, HAWK-I/NB2090

The data set was obtained during an observational night on 23$^{\text{rd}}$ January 2012 (JD = 2,455,949), by using FPM of HAWK-I through filter NB2090. The target star was observed together with two comparison stars. Note that there are two notations for this planetary system—besides WASP-51 also HAT-P-30 is used.

During the first third of the observation the target was rising on the sky and nearly reached the zenith. For the rest of the night it was setting down to reaching an altitude of 20°—this is reflected in the airmass. Coherence time was varying during the whole observation in a range of roughly three milliseconds with several sudden changes. Following this trend, seeing was significantly changing as well. Target positions on the detector

were stable in a range of twelve pixels and their variance did not noticeably affect the resulting light curve. What in contrast did affect the light curve is the variance of the coherence time/seeing.

WASP-51 b, *TESS*

This data set counts two individual data sets obtained between January 2019 and February 2021 which were observed in *TESS* sectors 7 and 34. The data include about 16 orbits of the planet around its parent star.

OGLE-9 b, HAWK-I/NB1190

This data set was obtained during an observational night on 28$^{\text{th}}$ January 2010 (JD = 2,455,224). Unlike the previous HAWK-I data, Generic Offset mode (template) was applied and the observation was performed through filter NB1190. The target star was one of many observed stars involved in the field of view of detector 3 of HAWK-I and nine of them were selected for further processing.

During the first quarter of the observation the observational conditions were the worst of the whole run—high airmass and seeing and short coherence time. Later, the target reached a higher altitude and the seeing decreased and stabilised in a range of 0.5″. The positions of the target on the detector on X and Y axis were stable within four and five pixels, respectively. In the applied instrument template, to subtract sky-background an offset is set which results in different positions of stars on even and odd images, especially on the X axis. All the mentioned measures seem to have an effect on the resulting light curve.

OGLE-9 b, FORS2/z_GUNN+78

Two data sets using z_GUNN+78 filter of FORS2 instrument were obtained from two observational runs. The former was performed on 4$^{\text{th}}$ March 2010 (denoted as 'March data'; JD = 2,455,259) and the latter on 25$^{\text{th}}$ May 2010 ('May data'; JD = 2,455,341). The data were acquired by using 'IMG' (imaging) instrument mode and 'Normal' readout mode. The target star was one of many observed stars within the field of view of detector 2 and ten of them were used in further processing.

March data: The observational conditions during the whole run were quite unstable. There was significant variance of coherence time and seeing with a strong drop in the middle of the observation. The target star was rising on the sky, implying decreasing airmass throughout the observation. Positions of the measured star on the detector on both the axes were keeping in a range of four pixels with successive stabilising of the position. The observational conditions had an obvious effect on the resulting light curve, especially in the second half.

May data: In comparison with March data the observational conditions were more stable but found in less favourable ranges of values. From the second third of the observation, variance of coherence time and seeing decreased which is more important than the value itself as found out from the previous analyses of the ground-based data. The target star was setting during the whole run, implying dropping airmass. Target positions on the detector were stable in a range of three pixels for both the axes and with a constant slight drift in the positions. There is a moderate effect of the seeing variability on the resulting light curve. The data of this system are, nevertheless, rather white-noise than red-noise limited.

OGLE-9 b, *TESS*, UVES

These data consist of three individual data sets. They were obtained between March 2019 and April 2021 and were observed in *TESS* sectors 10, 11 and 37. They include in total 30 complete orbits of the planet around its star.

The analysis of the *TESS* photometric data also includes spectroscopic data. These were acquired with Ultraviolet and Visual Echelle Spectrograph (UVES) of ESO between December 2007 and January 2008. The resulting radial velocity measurements contain eight data points. The star was observed, the data were analysed and the original results published by Snellen et al. (2009). From this work, the measured radial velocities were adopted.

Table 3: Properties of the data sets studied in this section. For the ground-based data, $\tau_{\rm int}$ is the integration time, $N_{\rm CFF}$ is the number of cube `fits` files, and $N_{\rm FF}$ is the number of particular images of the given cube. Further, $N_{\rm ax1}$ and $N_{\rm ax2}$ are the sizes of images in X and Y axis, respectively, and $t_{\rm first}$ and $t_{\rm last}$ are the times of the first and the last image taken of the given data subset, respectively. For the *TESS* data, $N_{\rm dp}$ denotes the number of data points per a data set and time ranges of the observations are given in the common calendar and Julian date.

$\tau_{\rm int}$ (s)	$N_{\rm CFF}$	$N_{\rm FF}$	$N_{\rm ax1}$ (px)	$N_{\rm ax2}$ (px)	$t_{\rm first}$ (UTC)	$t_{\rm last}$ (UTC)
WASP-18, HAWK-I/NB1060						
0.7674	31	1516	4096	920	1.46:16	2.09:06
0.8000	605	20,942	4096	920	2.10:36	7.24:54
All:	**636**	**22,458** |	**Duration of the observation: 5 h 38 min 38 s**			
WASP-18, HAWK-I/NB2090						
2.0000	2	28	4096	2260	04.12:09	04.13:24
1.8432	186	2009	4096	2260	04.17:44	05.41:42
0.5000	98	4053	4096	460	05.52:03	06.32:50
0.3966	655	32,989	4096	460	06.33:23	10.38:04
All:	**941**	**39,079** |	**Duration of the observation: 6 h 25 min 55 s**			
WASP-36, HAWK-I/NB2090						
6.0	2	128	4096	512	03.22:19	03.35:22
4.0	5	315	4096	512	03.37:00	03.59:37
2.5	100	6300	4096	512	04.00:35	09.00:31
All:	**107**	**6743** |	**Duration of the observation: 5 h 38 min 12 s**			
WASP-43, HAWK-I/NB1060						
1.2	99	2475	4096	200	02.46:33	03.39:35
All:	**99**	**2475** |	**Duration of the observation: 0 h 53 min 02 s**			
WASP-50, HAWK-I/NB2090						
0.8	7	413	4096	512	01.06:39	01.18:41
1.5	38	2394	4096	512	01.19:21	02.32:32
0.7	261	16,440	4096	512	02.33:19	08.00:00
All:	**306**	**19,247** |	**Duration of the observation: 6 h 53 min 21 s**			
WASP-51, HAWK-I/NB2090						
0.2156	1	62	4096	512	02.06:07	02.06:21
0.2500	191	10,092	4096	512	02.07:16	03.49:28
0.4000	420	26,435	4096	512	03.49:58	09.07:25
All:	**612**	**36,589** |	**Duration of the observation: 7 h 01 min 18 s**			

			OGLE-9, HAWK-I/NB1190			
8.0	—	272	2048	2048	04.38:43	09.45:10
All:		**272** |	**Duration of the observation:**		**5 h 06 min 27 s**	
			OGLE-9, FORS2/z_GUNN+78, March data			
10.0	—	437	2048	1024	00.30:21	04.59:59
All:		**437** |	**Duration of the observation:**		**4 h 29 min 38 s**	
			OGLE-9, FORS2/z_GUNN+78, May data			
10.0	—	6	2048	1024	00.30:08	00.33:20
5.0	—	2	2048	1024	00.34:24	00:35:00
7.0	—	413	2048	1024	00.35:58	04.30:45
All:		**421** |	**Duration of the observation:**		**4 h 00 min 37 s**	

Sector	N_{dp}	$Date_{beg}$	$Date_{end}$	JD_{beg}	JD_{end}	Days
			WASP-51, TESS			
7	16,362	08/01/19	01/02/19	2,458,491	2,458,515	25
34	16,809	14/01/21	08/02/21	2,459,228	2,459,253	26
All:	**33,171** |		**Days of the observation in total:**			**51**
			OGLE-9, TESS			
10	16,458	26/03/19	22/04/19	2,458,568	2,458,595	28
11	16,881	23/04/19	20/05/19	2,458,596	2,458,623	28
37	17,336	02/04/21	28/04/21	2,459,306	2,459,332	27
All:	**50,675** |		**Days of the observation in total:**			**83**

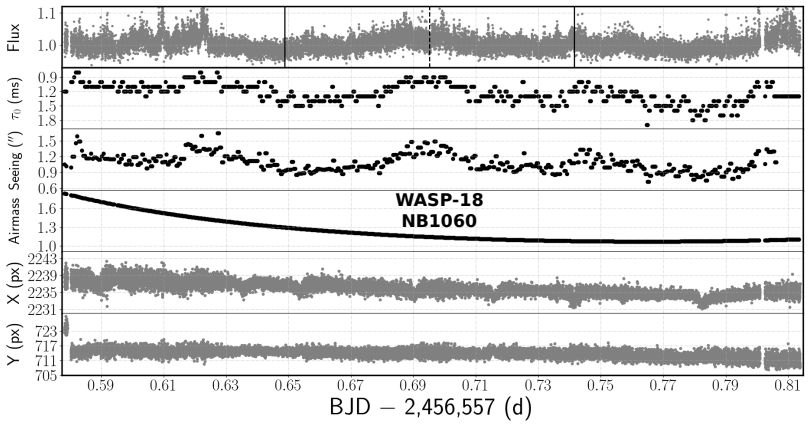

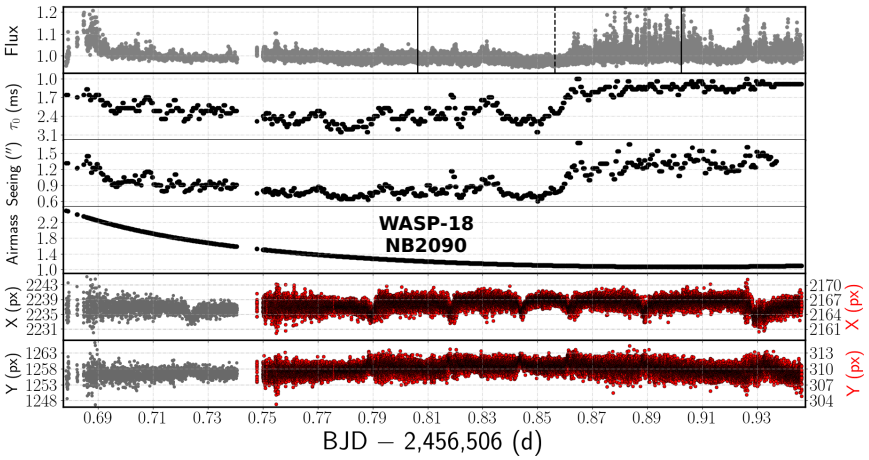

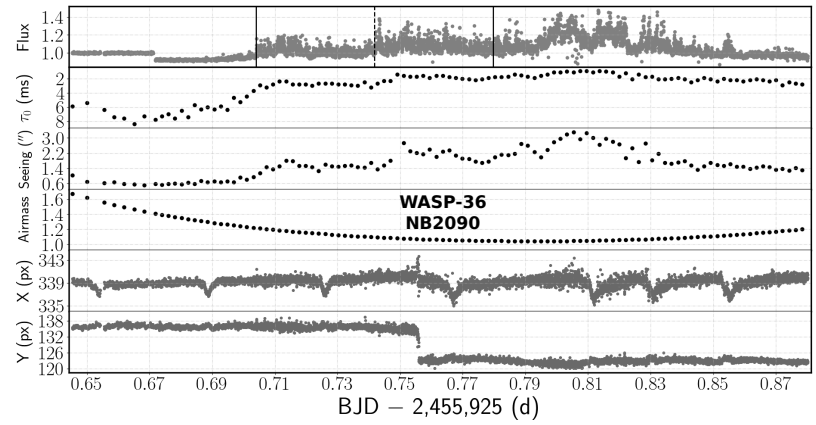
Flux
τ_0 (ms)
Seeing (″)
Airmass
X (px)
Y (px)
WASP-36
NB2090
BJD − 2,455,925 (d)

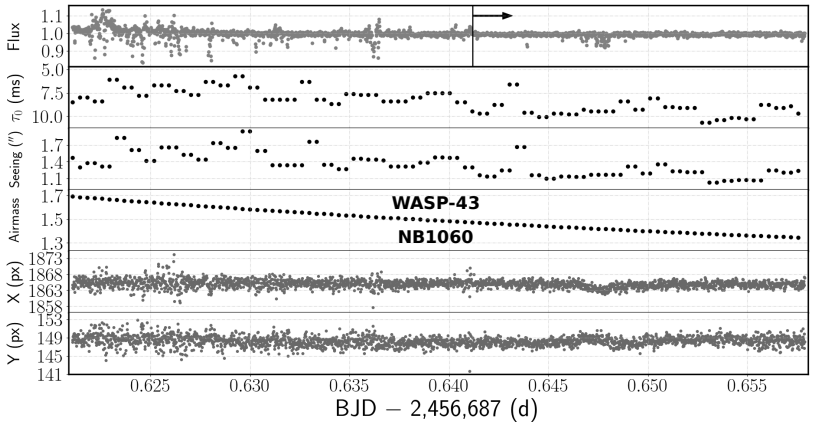
Flux
τ_0 (ms)
Seeing (″)
Airmass
X (px)
Y (px)
WASP-43
NB1060
BJD − 2,456,687 (d)

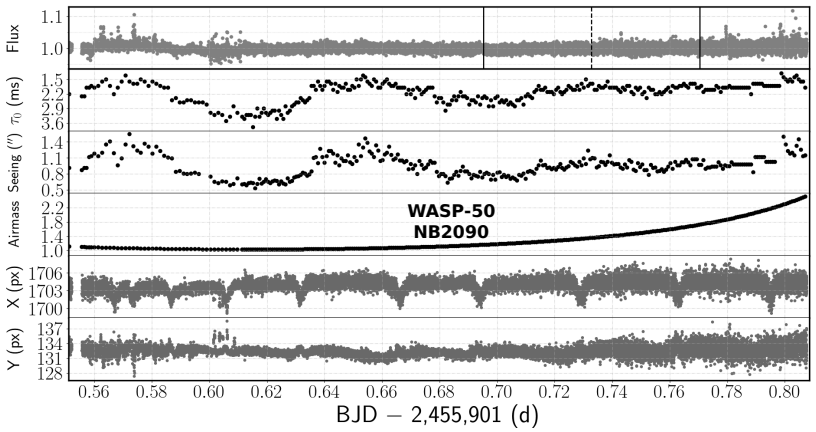
Flux
τ_0 (ms)
Seeing (″)
Airmass
X (px)
Y (px)
WASP-50
NB2090
BJD − 2,455,901 (d)

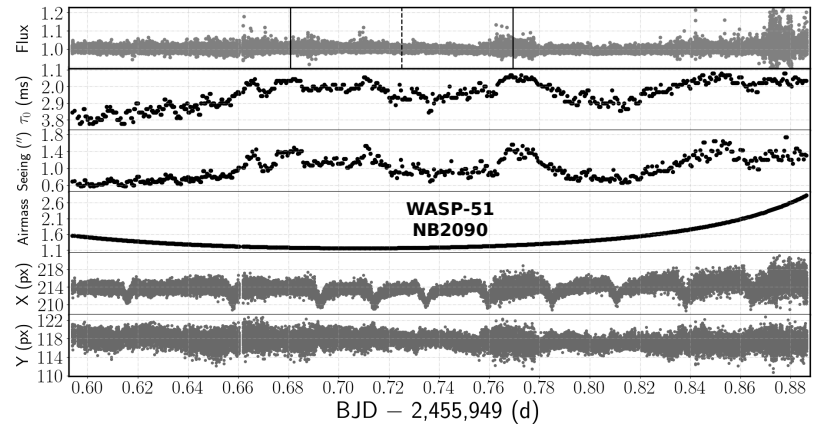
Flux
τ_0 (ms)
Seeing (″)
Airmass
X (px)
Y (px)
WASP-51
NB2090
BJD − 2,455,949 (d)

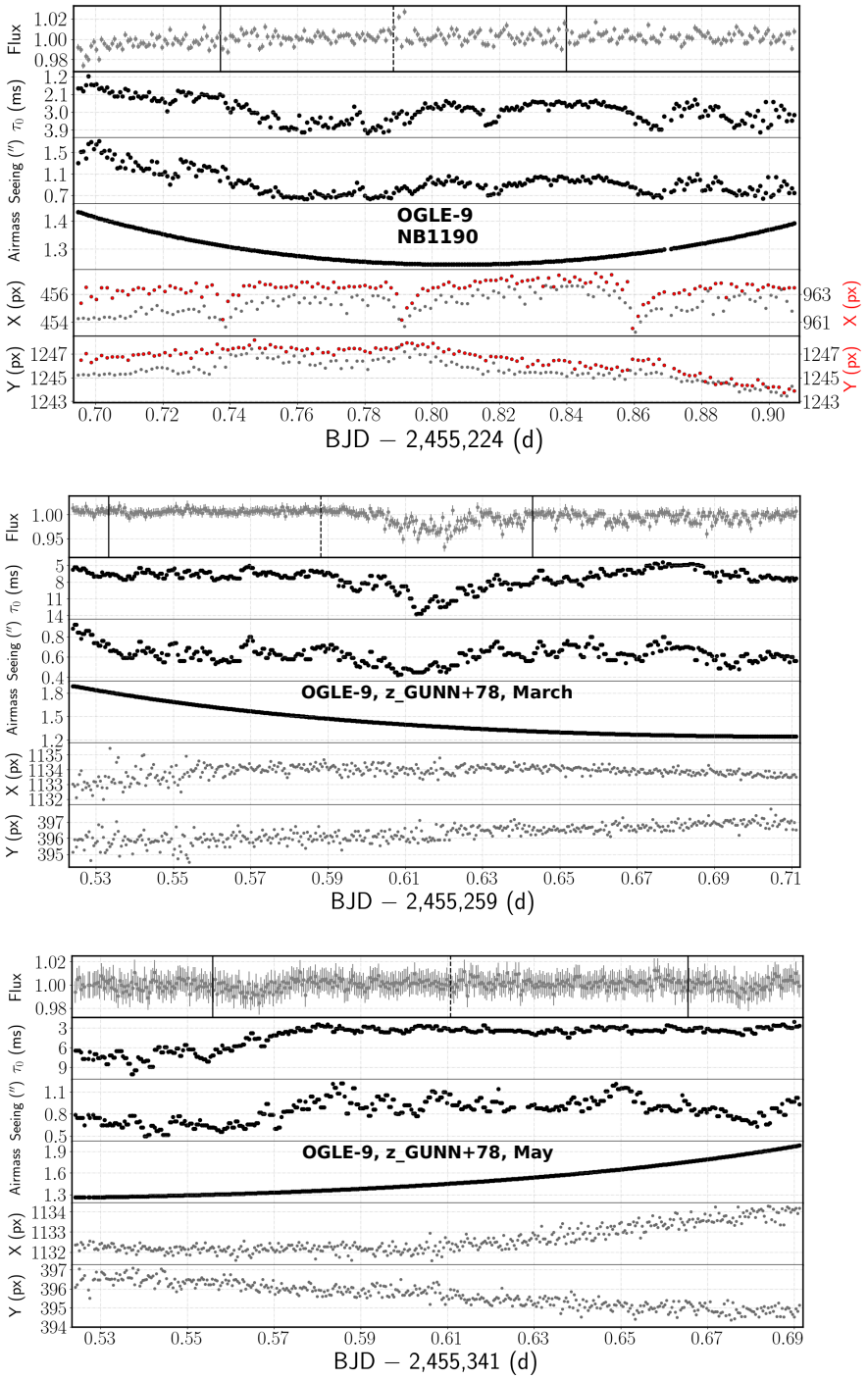

Figure 9: *Each panel from top to bottom*: normalised flux, coherence time, seeing, airmass, X and Y target position on the detector, all as the function of time. The vertical lines on the uppermost plot show the expected time of the beginning, the centre and the end of the occultation. This is shown for all the ground-based data of this section.

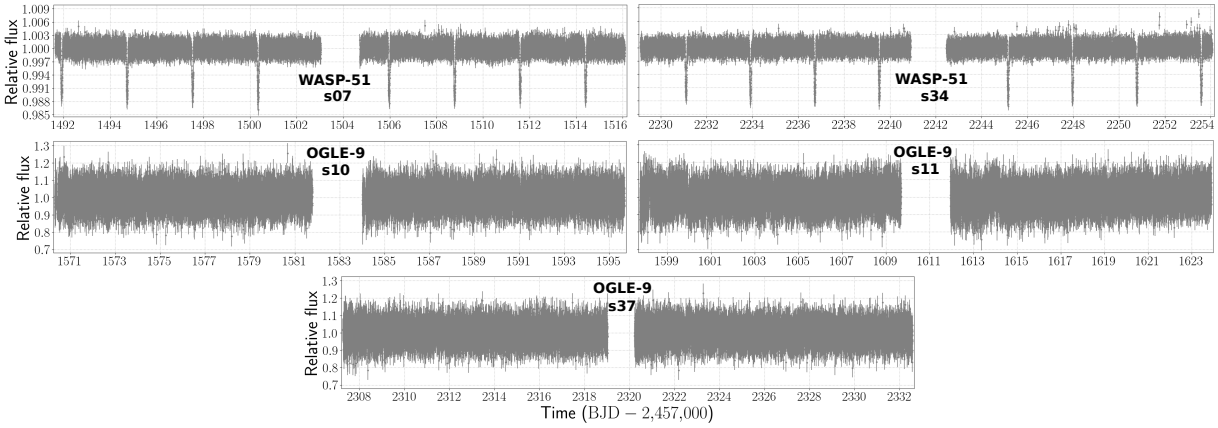

Figure 10: Raw *TESS* light curves of WASP-51 and OGLE-9 which are analysed in this section. Due to high uncorrelated noise the primary transits of OGLE-9 b are not visible in these original unbinned data.

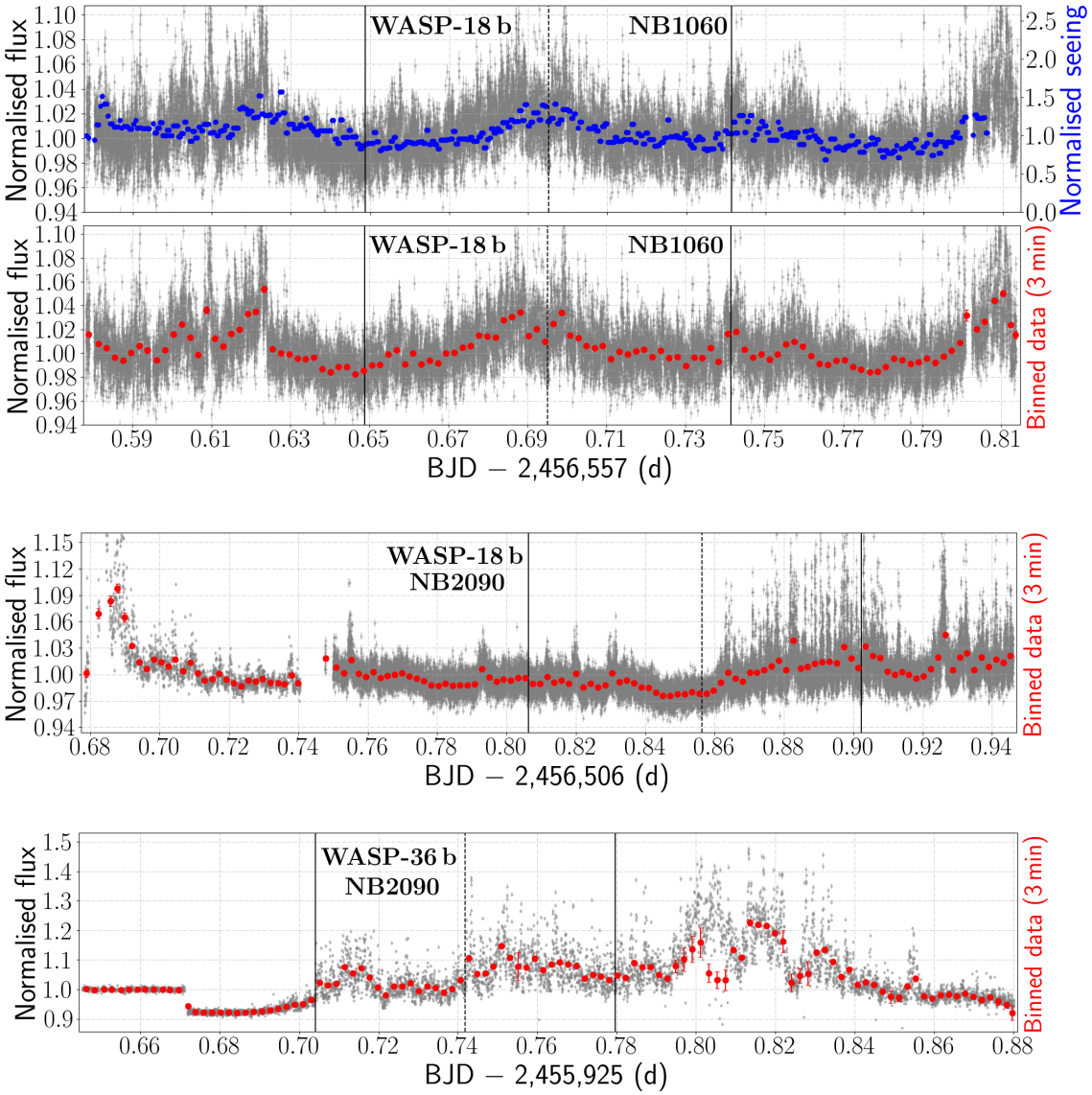

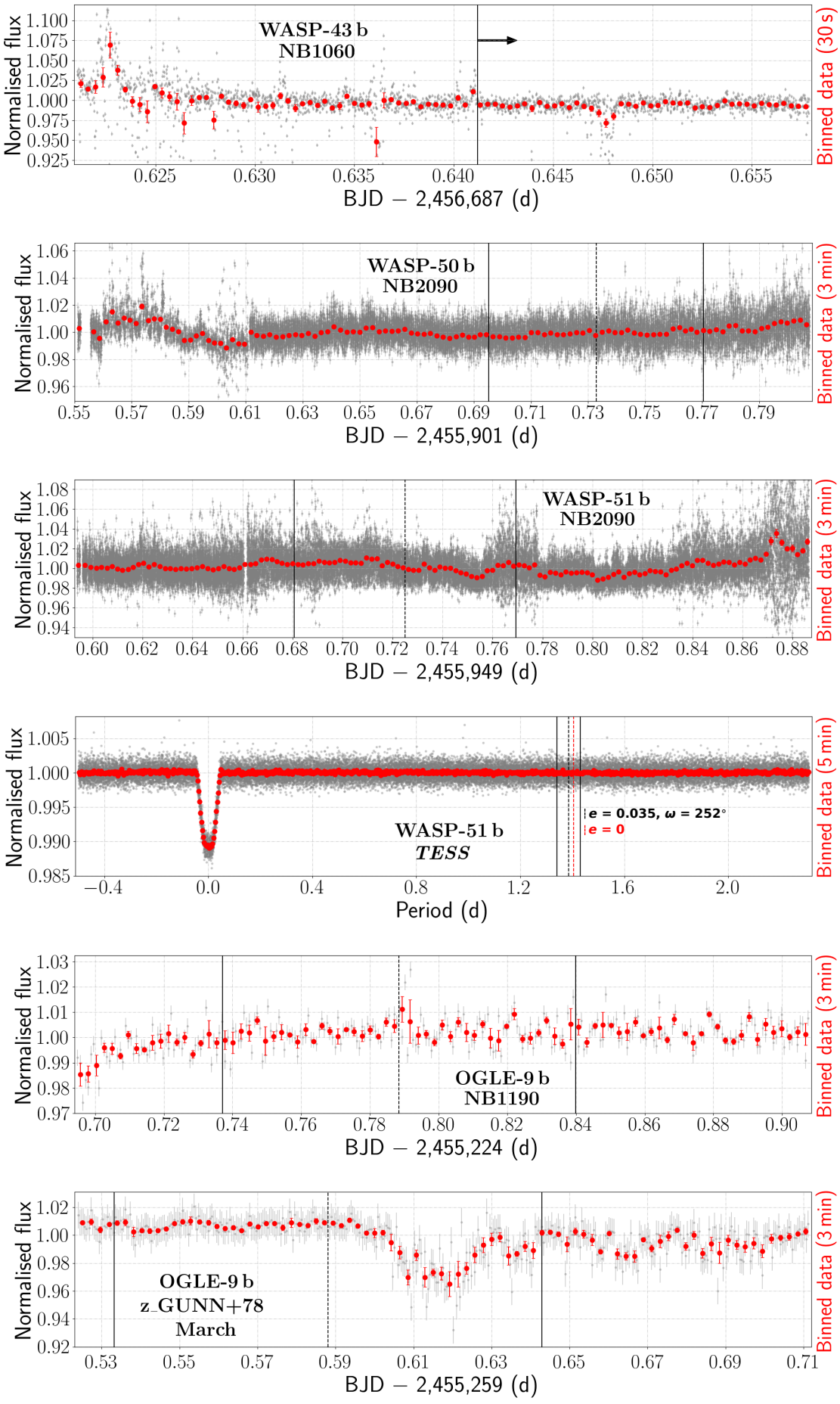
WASP-43 b
NB1060
Normalised flux
Binned data (30 s)
BJD − 2,456,687 (d)
WASP-50 b
NB2090
Binned data (3 min)
BJD − 2,455,901 (d)
WASP-51 b
NB2090
BJD − 2,455,949 (d)
WASP-51 b
TESS
e = 0.035, ω = 252°
e = 0
Binned data (5 min)
Period (d)
OGLE-9 b
NB1190
BJD − 2,455,224 (d)
OGLE-9 b
z_GUNN+78
March
BJD − 2,455,259 (d)

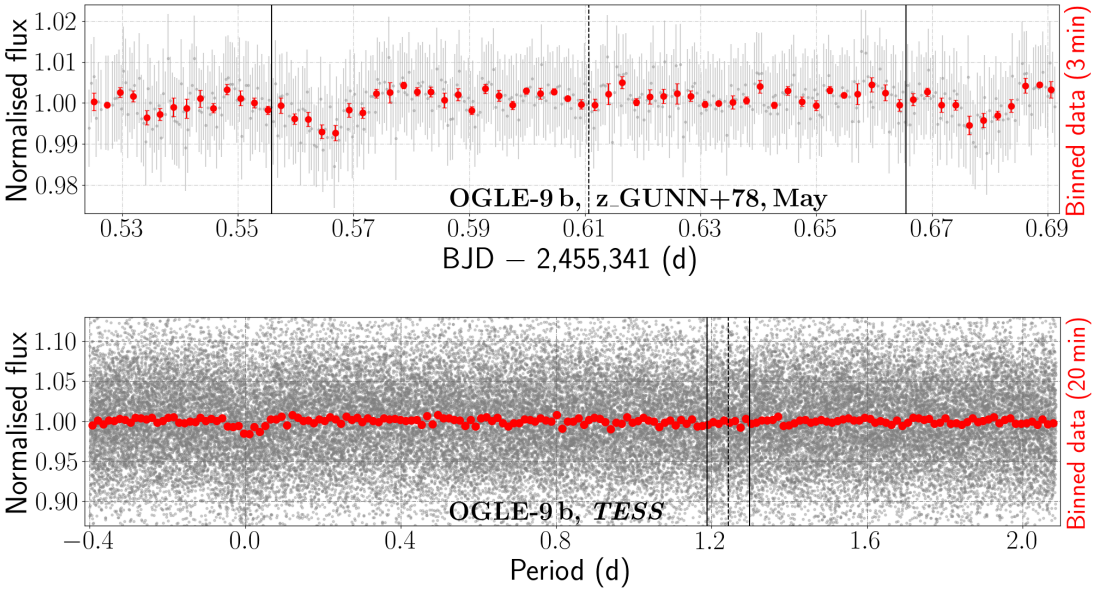

Figure 11: The HAWK-I, FORS-2 and *TESS* (period-folded) light curves of the systems studied in this section. The grey dots show normalised flux—for the ground-based data including error bars. The red bullets with the error bars (not always recognisable) show the binned data. The black vertical lines show the occultation event as in Figure 9. Except WASP-51 b/*TESS*, $e = 0$ is always supposed.

5.2. Data analysis and results

Although the quality of the data excludes a clear detection of the occultation, they were further analysed to see if any usable outcome can be attained. A theoretical estimate of possible detection of the occultation in each of the data sets was performed as described in Section 4.5. The resulting values are listed in Table 4. A fit of the unbinned light curve was performed. The resulting residuals were used for constructing a plot showing contribution of red noise. Furthermore, fits of the data binned per 3 minutes (unless a different bin width is explicitly mentioned) were performed, as described in Section 4.5.1.

Fits of OGLE-9 b/*TESS* were performed as modelling solely the photometric data as well as a joint fit of the *TESS* photometric and UVES spectroscopic data. To model the noise contained in the RV data, GP Real kernel was applied and the corresponding kernel hyperparameters were estimated from the data. These are GP amplitude of the RV, $(\ln)a$, and GP time scale of the RV, $(\ln)c$. The joint fit of the photometric and spectroscopic data gave more accurate results than the fit of purely *TESS* light curve. Furthermore, as the *TESS* data are white-noise limited due to low brightness of the measured star, they were binned per 20 minutes to increase the signal-to-noise ratio whilst keeping sufficient time resolution. Thus, results obtained from the joint fit and using the binned light curve are used for the further analysis.

The obtained values of the input and derived parameters are listed in Table 5 for the ground-based data and in Table 6 for the *TESS* and UVES data. The corresponding light curves and the RV curve with their best-fitting models are shown in Figures 12 and 13.

Planetary orbit

WASP-51 b, TESS: Since orbital parameters are not well constrained in published studies, they were set as free parameters. The derived values of the eccentricity and the argument

of periastron are $e = 0.145^{+0.031}_{-0.028}$ and $\omega = 172 \pm 9$ deg. Johnson et al. (2011) inferred $e = 0.035 \pm 0.024$ which implies an upper limit $e^{3\sigma\mathrm{UL}} < 0.072$ and is, thus, consistent with the derived eccentricity within $\approx 2.6\sigma$. Regarding the derived value of the argument of periastron, it is also consistent with that presented in the mentioned work as they inferred $\omega = 252 \pm 84$ deg. In this case, unlike the previous planets, the orbit is not circular and should not be considered as circularised. Moreover, this is supported by the result obtained by comparing the Bayesian factors for the above mentioned fit and a fit with supposed zero eccentricity which was also performed—$\Delta \ln Z > 800$ in favour of the fit with non-zero eccentricity.

OGLE-9 b, TESS: Investigation of the orbital parameters revealed that the orbital eccentricity is consistent with zero. If $\ln Z$ of fits with zero eccentricity set as a fixed and as a free parameter are compared, the former fit is slightly preferred. For the latter, the derived parameters are $e = 0.000\,133^{+000\,220}_{-000\,100}$ and $\omega = 165^{+130}_{-\ 99}$ deg, consistent with a circular orbit.

Phase curve variations

WASP-51 b, TESS: Although planetary atmospheric and Doppler boosting contributors to the phase curve modulation were not derived with sufficient significance, the amplitude of tidal (ellipsoidal) distortion is well detected, $A_{\mathrm{ellipsoidal}} = 0.0737^{+0.0095}_{-0.0096}$ ppt. This results in shifting the occultation event off the moment of the maximum flux. The detection of the ellipsoidal modulation shows that the parent star is tidally distorted by the gravity of the planet which is not a rare phenomenon in systems with hot Jupiters.

OGLE-9 b, TESS: The phase curve reveals obvious flux modulation. As none of the possible contributors to the phase curve modulation (atmospheric, beaming, ellipsoidal) were clearly detected, a straightforward conclusion can not be made. Nevertheless, the derived values of all the three contributors suggest that each of them contributes to the modulation of the phase curve to a similar extent.

Occultation (and transit) depth

WASP-18 b, HAWK-I/NB1060: The theoretical occultation depth was compared with $\mathrm{RMS_w}$ of the data to estimate possible detection. The obtained values of $\mathrm{RMS_w}$ suggest that the occultation is hidden in the noisy data which can also be clearly seen in the light curve. The $\mathrm{RMS_w}$ exceeds the expected depth by an order both in the case when in-occultation data points were excluded and included in the calculation. Due to the strong systematics the occultation can be barely detected.

The derived depth of the binned light curve is $\delta_{\mathrm{occ}} = 0.463^{+0.278}_{-0.284}$ ppt. Since the occultation depth is obtained only with $\approx 1.6\sigma$ significance, a 3σ upper limit on the occultation depth was placed, $\delta^{3\sigma\mathrm{UL}}_{\mathrm{occ}} < 0.853$ ppt. Sheppard et al. (2017) detected occultations in wavelength ranges lying between 1.1 and 1.7 µm from *HST*/WFC3 data. For the nearest wavelength range of 1.118–1.136 µm towards 1.06 µm of NB1060 filter they derived an occultation depth of 0.818 ± 0.028 ppt. This result is consistent with the placed upper limit on the occultation depth obtained from this data set.

WASP-18 b, HAWK-I/NB2090: Like the previous data, this data set is dominated by noise and by comparing the expected depth with the derived $\mathrm{RMS_w}$ we come to the same results showing that the occultation can not be detected. Since the part of the light curve until BJD = 0.749 d exhibits a strong scatter of the data points and is relatively far from the occultation event, another approach was to discard this part for further analysis. The lowest obtained $\mathrm{RMS_w}$ of this reduced light curve is, however, still high

enough when compared to the maximum expected occultation depth, no matter if all or only out-of-occultation data were involved in the calculation.

The obtained depth is $\delta_{\rm occ} = 0.490^{+0.267}_{-0.281}$ ppt which is within one sigma value of the depth obtained from NB1060 data. This only $\approx 1.7\sigma$ significance implies a 3σ upper limit on the occultation depth, $\delta_{\rm occ}^{3\sigma{\rm UL}} < 0.844$ ppt, which broadly corresponds to the upper limit of NB1060. Zhou et al. (2015) detected from data of IRIS2 infrared camera of Anglo-Australian Telescope an occultation depth of 1.3 ± 0.3 ppt in Ks band ($\lambda_{Ks} = 2.144\,\mu$m) whose transmittance is close to that of NB2090 of HAWK-I. Their value is higher than the HAWK-I upper limit; however, if we take into account the inferred uncertainties of the detection, we reach $\approx 1.5\sigma$ consistency. Nevertheless, for longer wavelengths we would expect deeper occultation depths. It means that the value of Zhou et al. (2015) corresponds with this assumption in contrast to the upper limit obtained here. Moreover, the result of 1.3 ppt matches to the theoretical value supposing a low geometric albedo. Hence, the resulting occultation depth of NB2090 indicates to be undervalued.

WASP-36 b, HAWK-I/NB2090: This data set is very strongly affected by red noise. The comparison of the expected depth and the $\rm RMS_w$ of the binned data shows that there is one order difference between them and when comparing with the unbinned data, there is even two-order difference. The data set consists of three subsets (according to exposure times). During the observation of the last subset the observational conditions significantly worsened which is the reason why the normalised flux reveals such a 'jump' at BJD = 0.672 d. This analysis implies that the occultation can not be found in these data.

The binned light curve resulted in $\delta_{\rm occ} = 0.859^{+0.611}_{-0.616}$ which is only a $\approx 1.4\sigma$ significance. From the uncertainty of the derived depth, a 3σ upper limit on the occultation depth was set, $\delta_{\rm occ}^{3\sigma{\rm UL}} < 1.847$ ppt. This value is consistent with $\delta_{\rm occ} = 1.3 \pm 0.4$ ppt obtained in Ks filter with IRIS2 camera mounted on Anglo-Australian Telescope, operating at similar central wavelength as HAWK-I ($\lambda = 2.144\,\mu$m) and derived by Zhou et al. (2015).

WASP-43 b, HAWK-I/NB1060: The systematics of this data set are weaker than in the previous cases. The data scatter is largest at the first quarter and during the occultation the flux is relatively stable. However, the $\rm RMS_w$ of the data is still about four times greater than the expected depth when the geometric albedo of one is considered. Therefore, the $\rm RMS_w$ is supposed to exceed the real depth even more and thus making the detection of the occultation (the observed part) impossible.

The original light curve was binned per 30 seconds as a suitable compromise between the number of points and time resolution. The fit of the binned data resulted in an occultation depth of $1.187^{+0.927}_{-0.825}$ ppt which is only $\approx 1.3\sigma$ significance. From the uncertainty of the inferred depth a 3σ upper limit on the occultation depth was placed, $\delta_{\rm occ}^{3\sigma{\rm UL}} < 2.781$ ppt. It is consistent with the upper limits of 0.85 and 1.70 ppt of Gillon et al. (2012) obtained at 915.9 and 1186 nm, respectively (TRAPPIST/Sloan z' and HAWK-I/NB1190 filters). The derived value of 1.19 ppt is comparable with the maximum total expected value of 1.09 ppt. Yet, from an incomplete observation and inaccurate results an explicit conclusion can not be drawn.

WASP-50 b, HAWK-I/NB2090: The scattter of the data is relatively small, especially in the central part of the light curve the flux is relatively stable. Nevertheless, the $\rm RMS_w$ of the 3-min-binned data still exceeds the expected occultation depth about five and eight times for the geometric albedo values of one and one tenth, respectively. It is not, therefore, supposed that the occultation could be clearly detected in this data set.

The fit of the binned data resulted in $\delta_{\rm occ} = 1.072^{+0.590}_{-0.700}$ ppt which is not a clear detection ($\approx 1.5\sigma$) and which is a higher value than the expected depth. Another fit was performed with a discarded part of the data from the beginning up to 2,455,901.61 d

(exhibiting large scatter) but it did not lead to any improvement of the precision. Hence, from the original fit a 3σ upper limit on the occultation depth was placed, $\delta_{\rm occ}^{3\sigma{\rm UL}} < 2.1$ ppt. This is the first occultation measurement for this planetary system in the infrared bandpass, for the *TESS* band a 3σ upper limit of 0.149 ppt was derived (Blažek et al., 2022).

WASP-51 b, HAWK-I/NB2090: The expected depth is roughly the same as for WASP-50 b but the data scatter is about twice larger with some occasional stronger deviations. The $\rm RMS_w$ of the binned data is still an order greater than the expected depth. Hence, the occultation can not be clearly detected in this data set.

The fit of the binned light curve resulted in $\delta_{\rm occ} = 0.589^{+0.426}_{-0.397}$ ppt. The derived depth is not a convincing detection (only $\approx 1.4\sigma$), therefore, the uncertainties were used to place a 3σ upper limit on the occultation depth, $\delta_{\rm occ}^{3\sigma{\rm UL}} < 1.278$ ppt. This is the first constraint on the occultation depth for this wavelength. Blažek et al. (2022) placed $\delta_{\rm occ}^{3\sigma{\rm UL}} < 0.086$ ppt for the optical range (*TESS*) whilst using *Spitzer* data, Foster et al. (2016) inferred $\delta_{\rm occ} = 1.63 \pm 0.10$ and 1.46 ± 0.13 ppt for 3.6- and 4.5-μm channels, respectively; although in a thesis of the same author $\delta_{\rm occ} = 1.77 \pm 0.18$ and 2.47 ± 0.24 ppt for the same channels and observing runs were published (Foster, 2016). This is what would be expected, i.e. increasing occultation depth with longer wavelengths where thermal radiation of hot Jupiters more contributes to the overall planetary radiation. The inferred upper limit at 2.1 μm of NB2090 matches well between the depths obtained in the optical range and at 3.6 μm.

For the purpose of possible better detection of the occultation data from BJD = 2,455,949.84 were discarded as this part exhibits increased flux variance. This step, however, did not have the desired effect. The precision of the obtained depth remained practically unchanged but still being consistent with the above discussed results.

WASP-51 b, TESS: The comparison of the obtained $\rm RMS_w$ and the expected depth suggests that the occultation could be detected from the 5-min-binned data and if the geometric albedo was relatively high since the theoretical thermal emission of this planet for ths bandpass is negligible. We should not, however, expect a high albedo, so the occultation depth of a few hundredths ppt is a more realistic estimate. Therefore, a clear detection of the occultation is not expected in these data.

The inferred occultation depth is $\delta_{\rm occ} = 0.047^{+0.036}_{-0.029}$ ppt which, although to be very close to the expected value for $A_{\rm g} = 0.1$, is only 1.3σ significance. The uncertainty of the obtained depth leads to a 3σ upper limit on the occultation depth, $\delta_{\rm occ}^{3\sigma{\rm UL}} < 0.109$ ppt. The upper limit as well as the inferred depth are consistent with $\delta_{\rm occ}^{3\sigma{\rm UL}} < 0.086$ ppt derived by Blažek et al. (2022) in the *TESS* band. In fact, the difference is only in the approach how each the upper limit was inferred. These are the only measurements of the occultation of this planetary system in the visible bandpass.

The inferred transit depth is $\delta_{\rm tra} = 10.838^{+0.053}_{-0.051}$ ppt. This is a lower and slightly inconsistent value with the planet-to-star area ratio of 12.2 ± 0.2 ppt derived by Enoch et al. (2011) using ground-based data (mostly in the visible band) or of 12.4 ± 0.1 ppt derived by Bai et al. (2022) using ground-based (R band) and *TESS* data. Note that the measured transit depth need not be necessarily equal to the ratio of the planet to star disc area. A minor cause of the inconsistency may come from using different software to analyse the data.

OGLE-9 b, HAWK-I/NB1190: For this data set, data reduction involved also applying a bad pixel mask replacing bad pixels spanning the stars used in photometry.

The scatter of the data is not so large as of the HAWK-I data obtained in Fast Photometry Mode. Further, the expected thermal emission is relatively weak at this wavelength due to high effective temperature of the parent star (spectral type F3), the

hottest star of all the studied systems. By comparing the total expected depth and the RMS_w we can see that the RMS_w is about one order greater than the expected depth. This implies that theoretically the occultation can not be detected in these data.

The fit of the binned light curve resulted in an occultation depth $\delta_{occ} = 0.264^{+0.394}_{-0.188}$ ppt. The value fits between the expected values although the significance is poor. From the uncertainty of the measurement a 3σ upper limit on the occultation depth was placed, $\delta_{occ}^{3\sigma UL} < 1.183$ ppt. This constraint is the first study of occultations of this exoplanetary system.

OGLE-9 b, FORS2/z_GUNN+78: For this wavelength, the thermal emission is lower than for HAWK-I/NB1190 whilst the assumed reflected light remains the same. This makes the possible detection more demanding.

• *March data*: The unstable observational conditions causing a strong flux drop during the occultation resulted in significantly greater RMS_w than the expected depth is. This shows that the occultation can not be theoretically detected in the data. Moreover, the baseline before the start of the occultation is too short which can generally make the measurement more difficult.

The inferred occultation depth is $\delta_{occ} = 0.621^{+0.423}_{-0.390}$ ppt ($\approx 1.5\sigma$). This non-detection implies a 3σ upper limit on the occultation depth, $\delta_{occ}^{3\sigma UL} < 1.268$ ppt which is a higher value than the maximum expected depth and roughly corresponding to the δ_{occ} of HAWK-I/NB1190. For this wavelength range it is, nevertheless, the first occultation measurement.

• *May*: Due to more stable conditions, these data are of better quality than March data. Nevertheless, the RMS_w is still more than five times greater when compared to the expected depth. Therefore, it is not supposed that the occultation could be clearly detected.

The inferred occultation depth obtained from this data set is $\delta_{occ} = 0.225^{+0.347}_{-0.166}$ ppt. This is again a non-detection and implies a 3σ upper limit on the occultation depth, $\delta_{occ}^{3\sigma UL} < 1.040$ ppt. This places a better constraint than in the case of the previous data set even though it is still roughly twice the maximum theoretical value.

• *March+May joint fit*: Both the data sets were also fitted as a joint fit to find out if it helps to get more precise results. This fit resulted in $\delta_{occ} = 0.594^{+0.424}_{-0.423}$ ppt and hence giving $\delta_{occ}^{3\sigma UL} < 1.272$. Whilst consistent with the values of the previous fits, this result did not help anyhow to better constrain the occultation depth. Therefore, the occultation constraint derived from May data is used in the further analysis.

OGLE-9 b, TESS: The high value of the apparent magnitude of the parent star leads to a high level of the photon noise. This is obvious in the raw light curves and even the flux drop due to transit is hidden in the original unbinned data. To decrease the photon noise and thus gain the signal-to-noise ratio, the data were binned per 20 minutes. Despite that, the RMS_w is still large enough to expect a clear detection of the occultation as there is one order difference between the theoretical occultation depth and the RMS_w of the binned light curve.

The inferred occultation depth of the 20-min-binned data is $\delta_{occ} = 1.153^{+0.527}_{-0.501}$ ppt. Since it is only a $\approx 2.2\sigma$ significance, a 3σ upper limit on the depth was placed, $\delta_{occ}^{3\sigma UL} < 1.582$ ppt. This is the first occultation constraint derived for this planet in the visible bandpass. The obtained depth and the upper limit are significantly greater than those obtained in the NIR bands and than the expected depth, even for $A_g = 1$. This could be theoretically explained by strong thermal emission of the planetary atmosphere but it can not be explained entirely by reflected light. On the contrary, the geometric albedo is expected to be low as ultra-hot Jupiters lack clouds to reflect the incident radiation due to high temperature of the atmosphere.

The derived transit depth is $\delta_{\mathrm{tra}} = 17.50^{+2.04}_{-2.16}$ ppt. The transit depth itself has not so far been published at any work but some authors inferred the planet-to-star radius ratio. When it is used to calculate the ratio of the planetary to stellar area ($R_{\mathrm{p}}^2/R_\star^2$), we come to 11.77 ± 0.02 ppt (optical $g'r'i'z'$ channels; Snellen et al. 2009) or 12.54 ± 0.67 ppt (optical $g'r'i'z'$ channels; Lendl et al. 2010) which does not well match the derived *TESS* transit depth. To do a proper comparison, the obtained values of $R_{\mathrm{p}}/R_\star$ should be compared each other since and a transit depth need not be equal to $R_{\mathrm{p}}^2/R_\star^2$. By doing so, the $R_{\mathrm{p}}/R_\star$ inferred here is consistent within 2.5 and 2.1σ with the mentioned works. The difference may be caused by atmospheric properties—Lendl et al. (2010) revealed a slight dependence of $R_{\mathrm{p}}/R_\star$ on wavelength. Moreover, they applied a larger stellar radius in their analyses than which is adopted in this thesis.

Radial velocity and mass of the planet

OGLE-9 b, TESS: From the joint fit of the RV curve with the *TESS* photometric data the semi-amplitude of the radial velocity of the star was derived, $K = 334^{+131}_{-144}\,\mathrm{m\,s^{-1}}$. This is a lower value than $510 \pm 170\,\mathrm{m\,s^{-1}}$ obtained by Snellen et al. (2009) from the same data. It must be noted, however, that the data point at phase ≈ 0.61 is vertically shifted by $\approx 0.9\,\mathrm{km\,s^{-1}}$ in the mentioned work or the RV value of this point in their table of listed spectroscopic observations is incorrect. The difference in the values of this data point consequently affected the derived semi-amplitude and the planetary mass. The herein inferred mass of the planet is $2.95^{+1.24}_{-1.28}\,\mathrm{M_J}$ whilst the mass obtained by Snellen et al. (2009) is $4.5 \pm 1.5\,\mathrm{M_J}$. Even though the semi-amplitude and therefore the mass derived here are not well constrained, the results are still consistent with the discussed work.

Table 4: Expected occultation depths and RMS_w of the data sets of the systems studied in this section. The superscripts III and V at OGLE-9 denote to March and May data, respectively. *Notes*: $^{(a)}$: calculated from Equation 7 supposing blackbody radiation of both the objects; $^{(b)}$: calculated from Equation 8 supposing $A_g = 1$ or $A_g = 0.1$; $^{(c)}$: binned per 30 seconds.

Occultation depth (ppt)	WASP-18 NB1060	WASP-18 NB2090	WASP-36 NB2090	WASP-43 NB1060	WASP-50 NB2090
Expected depth due to thermal emission$^{(a)}$	0.279	1.131	0.844	0.039	0.372
$\boldsymbol{A_g = 1}$:					
Expected depth due to reflected light$^{(b)}$	0.791	0.791	0.576	1.049	0.349
Total expected depth$^{(a)(b)}$	1.069	1.922	1.420	1.088	0.721
$\boldsymbol{A_g = 0.1}$:					
Expected depth due to reflected light$^{(b)}$	0.079	0.079	0.058	0.105	0.035
Total expected depth$^{(a)(b)}$	0.358	1.210	0.902	0.144	0.407
Data used for RMS_w calculation (ppt)					
Unbinned data, all	22.532	22.623	256.527	26.502	9.764
Unbinned, out-of-occultation data	23.850	22.730	279.233	34.734	10.287
Binned per 3 minutes, all	11.755	10.465	41.720	4.471$^{(c)}$	3.304
Binned per 3 minutes, out-of-occultation data	12.045	8.840	39.814	6.778$^{(c)}$	3.765
Binned (3 min), best-fitting model residuals	5.488	4.494	4.210	3.041$^{(c)}$	1.360

Occultation depth (ppt)	WASP-51 NB2090	WASP-51 *TESS*	OGLE-9 NB1190	OGLE-9^{III} z_G.+78	OGLE-9^{V} z_G.+78	OGLE-9 *TESS*
Expected depth, thermal emission$^{(a)}$	0.455	0.007	0.151	0.062	0.062	0.022
$\boldsymbol{A_g = 1}$:						
Expected depth, reflected light$^{(b)}$	0.272	0.272	0.365	0.365	0.365	0.365
Total expected depth$^{(a)(b)}$	0.726	0.278	0.516	0.426	0.426	0.386
$\boldsymbol{A_g = 0.1}$:						
Expected depth, reflected light$^{(b)}$	0.027	0.027	0.036	0.036	0.036	0.036
Total expected depth$^{(a)(b)}$	0.482	0.034	0.188	0.098	0.098	0.058
Data used for RMS_w calculation (ppt)						
Unbinned data, all	17.076	1.023	6.383	12.989	4.503	55.728
Unbinned, out-of-occultation data	18.638	—	6.534	9.752	4.672	—
Unbinned data, 1-min intervals	—	0.929	—	—	—	52.923
Binned per 3 minutes, all	5.355	—	2.838	6.088	2.213	—
Binned per 3 minutes, out-of-occ.	5.274	—	3.377	5.927	2.339	—
Binned per 5/20 minutes	—	0.158	—	—	—	3.958
Binned per 5/20 min, 20/60-min int.	—	0.054	—	—	—	2.407
Un/-binned, best-fitting model res.	1.206	0.004	0.016	2.298	0.044	0.005

Table 5: The input and derived parameters by ALLESFITTER of the data sets analysed in this section. Parameters with no given uncertainties were fixed during the fit.

Parameter (Unit)	WASP-18 NB1060	WASP-18 NB2090	WASP-36 NB2090	WASP-43 NB1060	WASP-50 NB2090
Planet–star radii ratio, $R_\mathrm{b}/R_\star$	0.0967	0.0967	0.1327	0.1574	0.1404
Sum of radii over semi-major axis, $(R_\star + R_\mathrm{b})/a_\mathrm{b}$	0.3131	0.3131	0.1952	0.2335	0.1552
Cosine of inclination angle, $\cos i_\mathrm{b}$	0.0997	0.0997	0.1193	0.1281	0.0917
Epoch of transit, $T_{0;\mathrm{b}}$ (d; $\mathrm{BJD_{TDB}}$)	2,456,558.165 845	2,456,507.326 997	2,455,926.510 538	2,456,688.073 797	2,455,900.748 725
Planetary orbital period, P_b (d)	0.941 457 6	0.941 457 6	1.537 365 3	0.813 474 4	1.955 090 5
Orbital eccentricity term, $\sqrt{e_\mathrm{b}}\cos\omega_\mathrm{b}$	-0.0016	-0.0016	0.0	0.0200	0.0420
Orbital eccentricity term, $\sqrt{e_\mathrm{b}}\sin\omega_\mathrm{b}$	-0.0938	-0.0938	0.0	-0.0250	0.0380
Surface brightness ratio, J_b	0.052 ± 0.031	0.051 ± 0.031	0.049 ± 0.034	$0.047^{+0.035}_{-0.033}$	$0.054^{+0.031}_{-0.036}$
Limb darkening coefficient, q_1	0.0	0.0	0.0	0.0	0.0
Limb darkening coefficient, q_2	0.0	0.0	0.0	0.0	0.0
White noise error scaling, $\ln\sigma_F$	-5.039 ± 0.080	$-4.852^{+0.074}_{-0.071}$	$-3.652^{+0.097}_{-0.102}$	$-5.033^{+0.077}_{-0.072}$	$-6.325^{+0.097}_{-0.099}$
Baseline offset, ΔF (rel. flux)	$-0.0001^{+0.0070}_{-0.0067}$	$-0.0001^{+0.0068}_{-0.0069}$	$0.022^{+0.026}_{-0.028}$	$0.003^{+0.010}_{-0.012}$	0.000 ± 0.007
GP, height scale, $\ln\sigma$	$-0.35^{+0.21}_{-0.25}$	$-0.55^{+0.29}_{-0.28}$	$-2.66^{+0.25}_{-0.20}$	$-4.13^{+1.14}_{-0.73}$	$-5.56^{+0.24}_{-0.19}$
GP, length scale, $\ln\rho$	$-0.85^{+0.15}_{-0.10}$	$-0.81^{+0.20}_{-0.13}$	$-4.05^{+0.22}_{-0.19}$	$-3.37^{+0.95}_{-0.78}$	$-4.24^{+0.34}_{-0.30}$
Derived parameter					
Occultation depth, $\delta_{\mathrm{occ;b}}$ (ppt)	$0.463^{+0.278}_{-0.284}$	$0.490^{+0.267}_{-0.281}$	$0.859^{+0.611}_{-0.616}$	$1.187^{+0.927}_{-0.825}$	$1.072^{+0.590}_{-0.700}$

Parameter (Unit)	WASP-51 NB2090	OGLE-9 NB1190	OGLE-9$^{\mathrm{III}}$ z_GUNN+78	OGLE-9$^{\mathrm{V}}$ z_GUNN+78	OGLE-9$^{\mathrm{III+V}}$ z_GUNN+78
Planet–star radii ratio, $R_\mathrm{b}/R_\star$	0.1134	0.1104	0.1104	0.1104	0.1104
Sum of radii over semi-major axis, $(R_\star + R_\mathrm{b})/a_\mathrm{b}$	0.1667	0.1921	0.1921	0.1921	0.1921
Cosine of inclination angle, $\cos i_\mathrm{b}$	0.1309	0.1380	0.1380	0.1380	0.1380
Epoch of transit, $T_{0;\mathrm{b}}$ (d; $\mathrm{BJD_{TDB}}$)	2,455,948.319 735	2,455,223.547 874	2,455,258.345 336	2,455,340.367 925	2,455,258.345 336
Planetary orbital period, P_b (d)	2.810 595 0	2.485 533 5	2.485 533 5	2.485 533 5	2.485 533 5
Orbital eccentricity term, $\sqrt{e_\mathrm{b}}\cos\omega_\mathrm{b}$	-0.0578	0.0	0.0	0.0	0.0
Orbital eccentricity term, $\sqrt{e_\mathrm{b}}\sin\omega_\mathrm{b}$	-0.1779	0.0	0.0	0.0	0.0
Surface brightness ratio, J_b	$0.044^{+0.036}_{-0.031}$	$0.022^{+0.031}_{-0.016}$	0.051 ± 0.034	$0.018^{+0.027}_{-0.014}$	$0.049^{+0.035}_{-0.033}$
Limb darkening coefficient, q_1	0.0	0.0	0.0	0.0	0.0
Limb darkening coefficient, q_2	0.0	0.0	0.0	0.0	0.0
White noise error scaling, $\ln\sigma_F$	-6.233 ± 0.100	$-8.008^{+1.267}_{-1.358}$	$-5.326^{+0.115}_{-0.141}$	$-8.014^{+1.253}_{-1.352}$	-5.647 ± 0.079
Baseline offset, ΔF (rel. flux)	0.000 ± 0.007	0.000 ± 0.007	$0.0001^{+0.0067}_{-0.0068}$	$0.0004^{+0.0070}_{-0.0066}$	$0.0001^{+0.0069}_{-0.0068}$
GP, height scale, $\ln\sigma$	$-5.01^{+0.21}_{-0.17}$	$-5.413^{+0.094}_{-0.097}$	$-4.701^{+0.277}_{-0.217}$	$-5.936^{+0.123}_{-0.121}$	$-5.045^{+0.204}_{-0.168}$
GP, length scale, $\ln\rho$	$-4.27^{+0.23}_{-0.22}$	$-6.146^{+0.157}_{-0.156}$	$-4.251^{+0.386}_{-0.396}$	$-5.962^{+0.268}_{-0.184}$	$-4.207^{+0.239}_{-0.218}$
Derived parameter					
Occultation depth, $\delta_{\mathrm{occ;b}}$ (ppt)	$0.589^{+0.426}_{-0.397}$	$0.264^{+0.394}_{-0.188}$	$0.621^{+0.423}_{-0.390}$	$0.225^{+0.347}_{-0.166}$	$0.594^{+0.424}_{-0.423}$

Table 6: The input and derived parameters by ALLESFITTER of the *TESS* and UVES data sets analysed in this section. *Notes*: $^{(a)}$: −2,457,000; $^{(b)}$: −2,454,000.

Parameter (Unit)	WASP-51	OGLE-9
Planet–star radii ratio, $R_\mathrm{b}/R_\star$	$0.109\,07 \pm 0.000\,44$	$0.1315^{+0.0088}_{-0.0092}$
Sum of radii over semi-major axis, $(R_\mathrm{b}+R_\star)/a_b$	$0.1694^{+0.0037}_{-0.0031}$	$0.1900^{+0.0135}_{-0.0103}$
Cosine of inclination angle, $\cos i_b$	$0.1373^{+0.0064}_{-0.0050}$	$0.1218^{+0.0178}_{-0.0159}$
Epoch of transit, $T_{0;\mathrm{b}}$ (d; $\mathrm{BJD_{TDB}}$)	$1491.915\,702^{+0.000\,148\,(a)}_{-0.000\,151}$	$465.422\,137^{+0.025\,502\,(b)}_{-0.015\,972}$
Planetary orbital period, P_b (d)	$2.810\,600\,32^{+0.000\,000\,77}_{-0.000\,000\,79}$	$2.485\,554\,28^{+0.000\,009\,27}_{-0.000\,015\,14}$
Host star RV semi-amplitude, K_b ($\mathrm{km\,s^{-1}}$)	—	$0.333\,555^{+0.130\,907}_{-0.143\,520}$
RV jitter term, $\ln\sigma_\mathrm{jitter}$	—	$-10.238^{+6.108}_{-6.555}$
Orbital eccentricity term, $\sqrt{e_\mathrm{b}}\cos\omega_\mathrm{b}$	$-0.372^{+0.041}_{-0.040}$	0.0
Orbital eccentricity term, $\sqrt{e_\mathrm{b}}\sin\omega_\mathrm{b}$	0.054 ± 0.055	0.0
Surface brightness ratio, J_b	$0.0037^{+0.0034}_{-0.0024}$	$0.047^{+0.028}_{-0.030}$
Limb darkening coefficient, q_1	0.3749 ± 0.0019	$0.232\,76^{+0.000\,98}_{-0.000\,92}$
Limb darkening coefficient, q_2	$0.1478^{+0.0039}_{-0.0037}$	$0.2492^{+0.0019}_{-0.0020}$
Doppler-boosting semi-ampl., $A_\mathrm{b;beaming}$ (ppt)	$0.0151^{+0.0079}_{-0.0073}$	$0.688^{+0.204}_{-0.272}$
Atmosph. modulat. ampl., $A_\mathrm{b;atmospheric}$ (ppt)	$0.0051^{+0.0065}_{-0.0037}$	$0.314^{+0.332}_{-0.216}$
Ellipsoidal modulat. ampl., $A_\mathrm{b;ellipsoidal}$ (ppt)	$0.0737^{+0.0095}_{-0.0096}$	$0.452^{+0.314}_{-0.257}$
White noise error scaling, $\ln\sigma_F$	$-9.586^{+0.448}_{-0.591}$	$-6.368^{+0.968}_{-2.434}$
Baseline offset, ΔF (rel. flux)	$0.000\,032^{+0.000\,645}_{-0.000\,678}$	$0.000\,22^{+0.006\,10}_{-0.006\,58}$
GP, height scale, $\ln\sigma$	$-6.8956^{+0.0042}_{-0.0047}$	$-3.916^{+0.014}_{-0.019}$
GP, length scale, $\ln\rho$	$-7.8506^{+0.0645}_{-0.0964}$	$-4.857^{+0.031}_{-0.032}$
GP, amplitude, $\ln a$	—	$0.136^{+1.278}_{-1.013}$
GP, time scale, $\ln c$	—	$-9.659^{+3.709}_{-3.345}$
Host radius over semi-major axis; $R_\star/a_\mathrm{b}$	$0.1527^{+0.0034}_{-0.0028}$	$0.1680^{+0.0115}_{-0.0088}$
Planetary radius; R_b ($\mathrm{R_J}$)	1.412 ± 0.033	$1.917^{+0.177}_{-0.176}$
Semi-major axis; a_b (AU)	0.0405 ± 0.0012	$0.0414^{+0.0034}_{-0.0033}$
Inclination; i_b (deg)	$82.11^{+0.29}_{-0.37}$	$83.01^{+0.92}_{-1.04}$
Eccentricity; e_b	$0.1449^{+0.0307}_{-0.0283}$	—
Argument of periastron; ω_b (deg)	$171.7^{+8.5}_{-8.7}$	—
Mass ratio; q_b	—	$0.00186^{+0.00077}_{-0.00081}$
Planetary mass; M_b ($\mathrm{M_J}$)	—	$2.949^{+1.242}_{-1.281}$
Impact parameter; $b_\mathrm{tra;b}$	0.8631 ± 0.0029	$0.726^{+0.060}_{-0.067}$
Total transit duration; $T_\mathrm{tot;b}$ (h)	$2.2424^{+0.0103}_{-0.0105}$	$2.803^{+0.139}_{-0.128}$
Full-transit duration; $T_\mathrm{full;b}$ (h)	$0.7101^{+0.0345}_{-0.0373}$	$1.544^{+0.256}_{-0.307}$
Epoch occultation; $T_\mathrm{0;occ;b}$ (d; $\mathrm{BJD_{TDB}}$)	$1493.067\,677^{+0.051\,093\,(a)}_{-0.055\,407}$	$466.664\,915^{+0.025\,690\,(b)}_{-0.016\,011}$
Impact parameter occultation; $b_\mathrm{occ;b}$	$0.8983^{+0.0383}_{-0.0356}$	$0.726^{+0.060}_{-0.067}$
Transit depth; $\delta_\mathrm{tra;b}$ (ppt)	$10.838^{+0.053}_{-0.051}$	$17.502^{+2.043}_{-2.162}$
Occultation depth; $\delta_\mathrm{occ;b}$ (ppt)	$0.047^{+0.036}_{-0.029}$	$1.153^{+0.527}_{-0.501}$
Nightside flux; $F_\mathrm{nightside;b}$ (ppt)	$0.040^{+0.038}_{-0.028}$	$0.743^{+0.535}_{-0.455}$
Equilibrium temperature ($A_\mathrm{B}=0.3$); $T_\mathrm{eq;b}$ (K)	1594^{+28}_{-27}	1838^{+63}_{-51}
Combined host density from all orbits; $\rho_\mathrm{\star;combined}$ (cgs)	$0.672^{+0.038}_{-0.043}$	$0.646^{+0.113}_{-0.116}$
Planetary density; ρ_b (cgs)	—	$0.501^{+0.301}_{-0.214}$
Planetary surface gravity; g_b (cgs)	—	$1947.1^{+951.9}_{-796.7}$

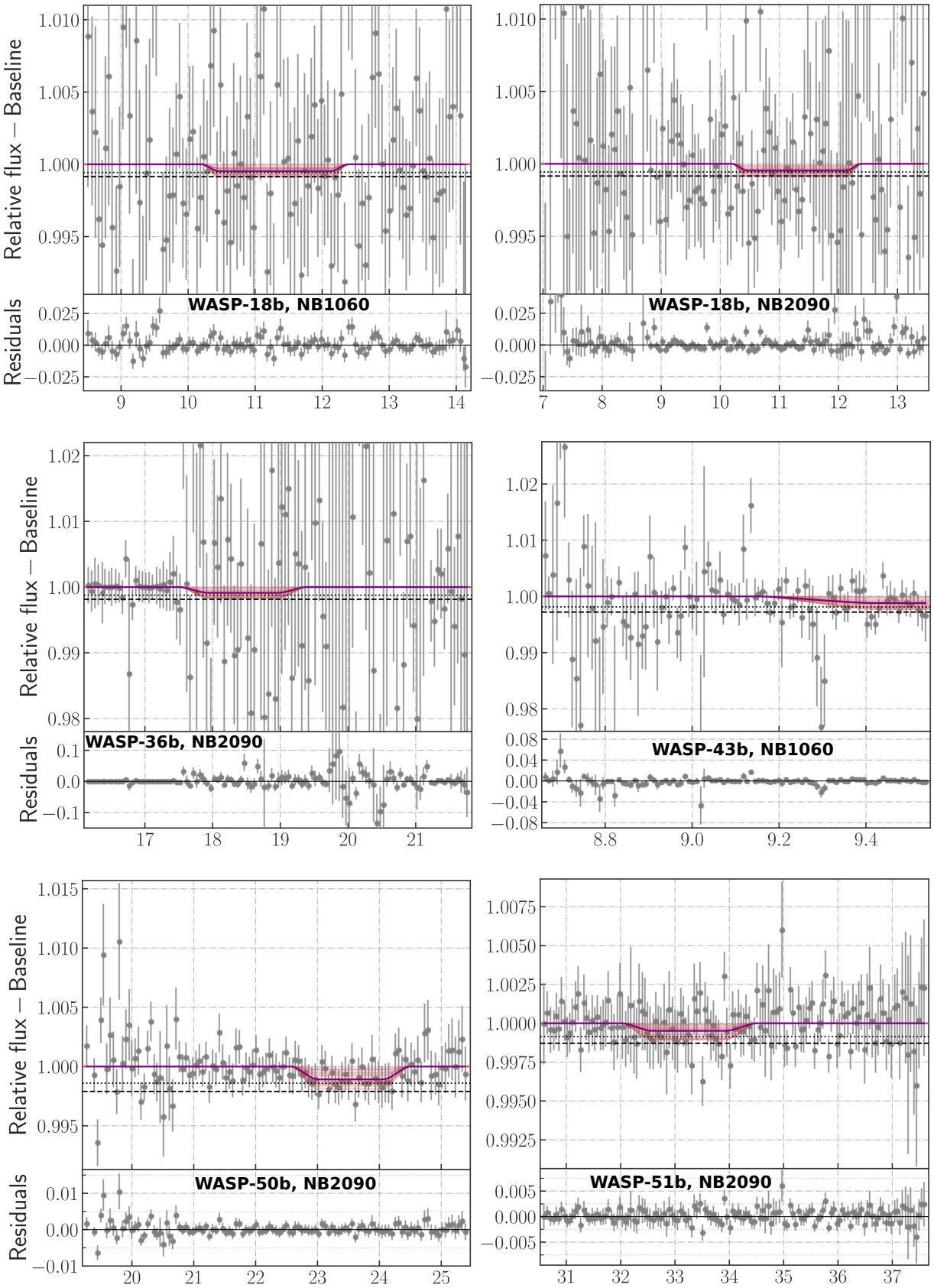
Relative flux − Baseline
Residuals
WASP-18b, NB1060
WASP-18b, NB2090
WASP-36b, NB2090
WASP-43b, NB1060
WASP-50b, NB2090
WASP-51b, NB2090

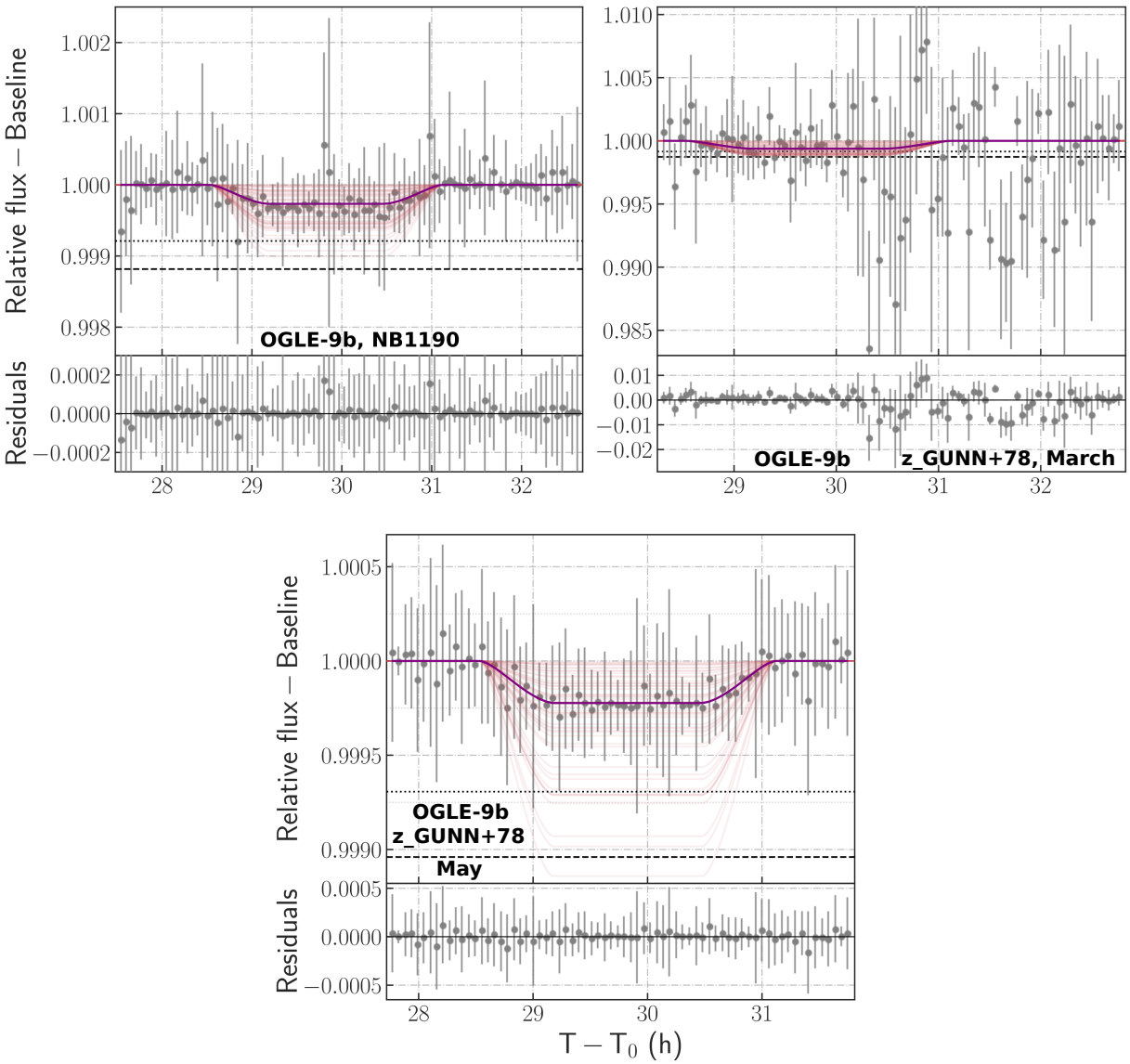

Figure 12: Fitted and GP-baseline detrended occultation light curves and residuals of the ground-based data sets analysed in this section. The dark-grey bullets with the error bars show the binned data. The red curves and the purple curve show 50 models randomly drawn and the median drawn from the posteriors, respectively. The black dotted and dashed horizontal lines show 2σ and 3σ upper limits on the occultation depth, respectively.

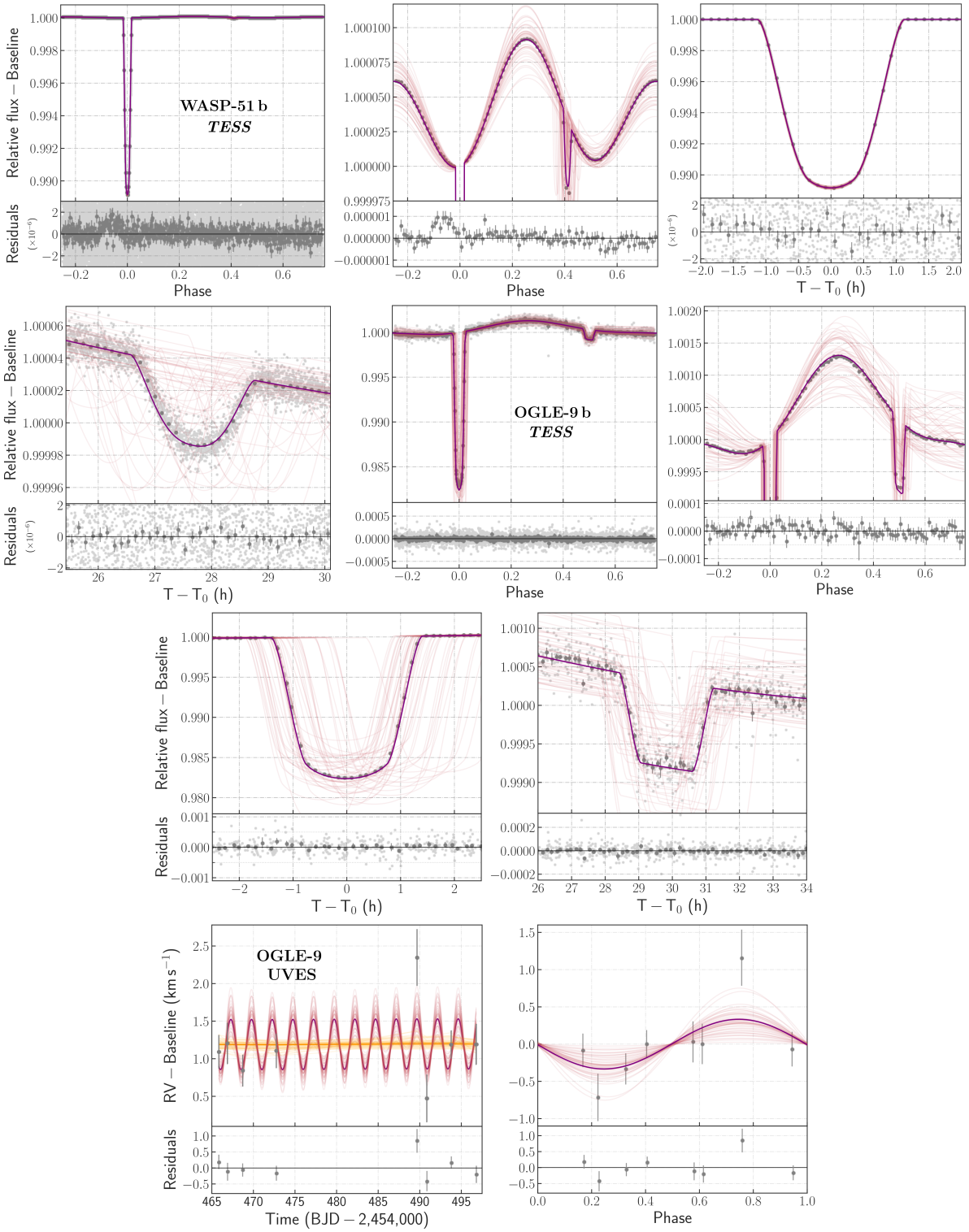

Figure 13: *From left to right and from top to bottom*: Fitted and phased light curves and the RV curve including residuals of the systems observed by *TESS* and UVES analysed in this section. The *TESS* curves show the whole phase curve, phase variations, and the transit and occultation events, respectively. Further, the light-grey dots show the original unbinned data whilst the dark-grey bullets with the error bars (not always visible) show the forced-binned data. In the UVES plots, the grey bullets with the error bars show the adopted radial velocities of the host star and the orange curve is the baseline model. The meaning of the remaining curves is as in Figure 12. The forced bins of the *TESS* data of WASP-51/OGLE-9 are: $\approx 8.1/7.2$ min (50 points = 0.1 phase), $\approx 40.5/35.8$ min (10 points = 0.1 phase), 7.5/8.6 minutes and 7.5/8.6 minutes, in the order of the listed plots.

5.3. Atmospheric properties

The derived occultation depths and especially the placed upper limits allowed to get estimates of some parameters of the planetary atmosphere. These included measuring of reflectivity by calculating the geometric albedo (Equation 2), finding the brightness temperature (Equation 4) of the dayside—and also the nightside if nightside flux is detected—and deriving the heat redistribution factor (Equation 6). Besides, the equilibrium temperature (Equation 3) was deduced from the adopted stellar and orbital parameters and assuming a zero Bond albedo and the heat redistribution factor of 1/4.

Some of the characteristics, especially the occultation depth itself, can be subsequently used as inputs into modelling routines developed to compute models (spectra) of planetary atmospheres. This was done for WASP-18 b and WASP-43 b using results obtained by the described analyses of the data. Nevertheless, even without modelling we are able to learn something about the atmospheres and compare each other. The atmospheric characteristics derived and discussed in this chapter are listed in Table 7.

Geometric albedo and thermal emission

WASP-18 b, HAWK-I/NB1060: The calculated reflected light component is 0.184 ppt which leads to an estimate of the near-infrared geometric albedo, $A_g = 0.233^{+0.358}_{-0.365}$. When using the occultation upper limit, a value of 0.574 ppt of the reflected light is obtained. This leads to a 3σ upper limit on the NIR geometric albedo, $A_g^{3\sigma\mathrm{UL}} < 0.726$. Even though this is not a strict constraint, it is consistent with an expected low geometric albedo. However, it must be noted that (near-) infrared observations should be rather translated into thermal emission than to reflected light and, thus, an albedo as scattering from clouds and hazes is pronounced in the optical band. Moreover, to estimate the thermal emission of the planet a blackbody form of the radiation was assumed. This need not be true for real atmospheres of planets and to interpret infrared observations atmospheric models are required.

WASP-18 b, HAWK-I/NB2090: The situation becomes different here than in the case of the NB1060 data set. The placed upper limit on δ_{occ} of 0.844 ppt is lower than the expected thermal emission of 1.131 ppt. Hence, subtracting the thermal emission from the derived depth or from the upper limit results in a negative value of the contribution due to reflected light. That is a naturally and physically impossible scenario and therefore a zero reflected light contribution can only be stated. This would imply that all the radiation at this wavelength is of thermal-radiation origin which is consistent with the already mentioned fact that infrared observations probe thermal radiation of planets rather than scattered light. The scenario of the lower upper limit than the expected thermal emission would mean that the planetary (and stellar) radiation does not take a form of a blackbody resulting in a lower temperature at this wavelength.

WASP-36 b, HAWK-I/NB2090: The obtained upper limit on the reflected light component is 1.002 ppt which implies $A_g^{3\sigma\mathrm{UL}} < 1.795$. This is a physically impossible value and can not constrain the near-infrared geometric albedo anyhow. Moreover, as already noted, the upper limit on the NIR occultation depth describes rather thermal emission than the light reflected by the planetary atmosphere.

WASP-43 b, HAWK-I/NB1060: To estimate the near-infrared geometric albedo, the reflected light of 2.742 ppt obtained from the occultation the upper limit was used. It leads to an upper limit on the NIR geometric albedo, $A_g^{3\sigma\mathrm{UL}} < 2.615$. This is, however, beyond a physically meaningful value and in addition not obtained from data acquired in the visible band. The high values of the occultation depth and the upper limit may

suggest that the thermal emission contributes to the overall flux more than it is expected theoretically supposing blackbody radiation of the planet (and the star).

WASP-50 b, HAWK-I/NB2090: The reflected light contribution of 1.728 ppt was obtained from the occultation upper limit. This leads to a 3σ upper limit on the near-infrared geometric albedo, $A_{\rm g}^{3\sigma{\rm UL}} < 4.957$. This is a physically impossible value for an albedo. Thus, it can only be claimed that considering the high occultation upper limit strong thermal radiation of the planet may exist.

WASP-51 b, HAWK-I/NB2090: The obtained upper limit on the contribution of the reflected light is 0.823 ppt which leads to a 3σ upper limit on the geometric albedo, $A_{\rm g}^{3\sigma{\rm UL}} < 3.032$. Such a value is beyond possible values of albedos. Hence, the conclusion is the same as for the previous planets/data sets.

WASP-51 b, TESS: The theoretical thermal emission was subtracted from the occultation depth or from the upper limit. The obtained reflected light and its upper limit of 0.04 and 0.102 ppt led to the geometric albedo of $0.144^{+0.131}_{-0.106}$ or a 3σ upper limit, $A_{\rm g}^{3\sigma{\rm UL}} < 0.367$. The result is consistent with that obtained by Blažek et al. (2022) and also agrees with typically low albedo values of hot Jupiters.

OGLE-9 b, HAWK-I/NB1190: To estimate the near-infrared geometric albedo, the reflected light of 1.032 ppt was used to obtain $A_{\rm g}^{3\sigma{\rm UL}} < 2.832$ which is a physically impossible value. It does not enable to put any constraint on the NIR geometric albedo. In any case, for an ultra-hot Jupiter like OGLE-9 b the albedo is expected to be very low or zero and hence the radiation from the planet is supposed to be of thermal-emission origin.

OGLE-9 b, FORS2/z_GUNN+78: The upper limit on the reflected light of 0.978 ppt was used to derive the near-infrared geometric albedo. This implies $A_{\rm g}^{3\sigma{\rm UL}} < 2.683$ and also in this case, it is not a valuable constraint and leads to the same conclusion like in the previous near-infrared data sets.

OGLE-9 b, TESS: The low theoretical value of thermal emission together with the high upper limit on the occultation depth resulted in a high upper limit on the reflected light of 1.56 ppt. This does not result in a valuable constraint on the geometric albedo as $A_{\rm g}^{3\sigma{\rm UL}} < 3.188$, allowing thus any value of the albedo. Since planets of this type typically exhibit low or zero geometric albedos, the high occultation upper limit suggests that the planetary thermal emission is stronger than theoretically estimated. That would mean that the radiation deflects from the blackbody radiation. To unveil this, clear occultation detections obtained at different wavelengths are needed.

Temperatures

WASP-18 b, HAWK-I/NB1060: The derived equilibrium temperature of the planet is $T_{\rm eq} = 2504^{+63}_{-65}$ K which categorises the planet as an ultra-hot Jupiter. Further, the brightness temperature for this wavelength (range) was estimated. For this filter, it is $T_{\rm br} = 2761^{+295}_{-458}$ K. If the occultation depth is substituted with its upper limit, then a 3σ upper limit on the brightness temperature can be placed, $T_{\rm br}^{3\sigma{\rm UL}} < 3150$ K. The temperature and the upper limit are consistent with the obtained equilibrium temperature. On the other hand, they may be indicative of temperature contrast between the planetary hemispheres. It is not rare to observe a hot dayside and a cooler nightside on such close-in planets.

WASP-18 b, HAWK-I/NB2090: For this filter, using the derived occultation depth and the upper limit, we obtain $T_{\rm br} = 1939^{+265}_{-380}$ and $T_{\rm br}^{3\sigma{\rm UL}} < 2274$ K, respectively. This is a significantly lower value than the upper limit of 3150 K obtained from NB1060 data as well as the equilibrium temperature of 2504 K. Although the definitions of these temperatures ($T_{\rm br}$ as a measured quantity vs $T_{\rm eq}$ as a theoretical quantity) do not exclude a result of

$T_{\rm br} < T_{\rm eq}$, the occultation non-detection and the upper limit do not lead to any convincing conclusion on the temperature.

WASP-36 b, HAWK-I/NB2090: The calculated equilibrium temperature is $T_{\rm eq} = 1754 \pm 42$ K. Furthermore, the brightness temperature was derived. Using the inferred occultation depth we come to $T_{\rm br} = 1761^{+274}_{-428}$ K and from the upper limit we obtain $T_{\rm br}^{3\sigma{\rm UL}} < 2176$ K. The temperature may suggest a hot dayside of the planet even though the real value can be hundreds of kelvins lower and, thus, consistent with the equilibrium temperature.

WASP-43 b, HAWK-I/NB1060: The equilibrium temperature was calculated to be $T_{\rm eq} = 1438^{+33}_{-30}$ K. From the upper limit on the occultation depth a brightness temperature upper limit was derived, $T_{\rm br}^{3\sigma{\rm UL}} < 2620$ K, or using the derived occultation depth we come to $T_{\rm br} = 2251^{+239}_{-373}$ K. This admits a scenario in which there is a non-negligible temperature difference between the dayside and the nightside of the planet.

WASP-50 b, HAWK-I/NB2090: The obtained equilibrium temperature of this planet is $T_{\rm eq} = 1411 \pm 33$ K. The inferred occultation depth leads to the brightness temperature of $T_{\rm br} = 1795^{+227}_{-389}$ K whilst the occultation upper limit implies a 3σ upper limit on the brightness temperature, $T_{\rm br}^{3\sigma{\rm UL}} < 2165$ K. The limit does not set a strict constraint on the brightness temperature but if $T_{\rm br}$ really exceeds $T_{\rm eq}$ by a few hundred kelvins as the results allow, then a temperature contrast exists between the dayside and the nightside of the planet.

WASP-51 b, HAWK-I/NB2090: The planetary equilibrium temperature was calculated to be $T_{\rm eq} = 1728 \pm 32$ K. Further, the brightness temperature and its upper limit were inferred and resulted in $T_{\rm br} = 1845^{+306}_{-425}$ K and $T_{\rm br}^{3\sigma{\rm UL}} < 2309$ K, respectively. Since the limit allows the brightness temperature to be equal to the $T_{\rm eq}$ as well as greater than it, any statement about if there is a temperature contrast between the hemispheres can not be done, similarly as in the previous cases.

WASP-51 b, TESS: The equilibrium temperature obtained for the herein inferred semi-major axis is 1743 ± 41 K. It is in good agreement with that obtained using the adopted value of the semi-major axis. The brightness temperature derived for this bandpass is $T_{\rm br} = 2166^{+169}_{-246}$ K, and $T_{\rm br}^{3\sigma{\rm UL}} < 2423$ K when the upper limit on the occultation depth is used. This limit is about 100 K higher than that obtained in the near-infrared filter of HAWK-I. This could mean that there is a source of absorption about 2.09 μm which causes the brightness temperature to be lower than in the *TESS* visible band. To show a possible temperature contrast between the dayside and the nightside, precise measurement of the occultation or/and the nightside flux is needed. In this case, the upper limit on the occultation depth and the nightside flux are roughly the same and, thus, does not allow us to prove or reject the existence of the temperature contrast between the planetary hemispheres.

OGLE-9 b, HAWK-I/NB1190: The equilibrium temperature of the planet was obtained to be $T_{\rm eq} = 2039 \pm 65$ K, a temperature categorising the planet to be an ultra-hot Jupiter. The derived planetary brightness temperature for this bandpass is $T_{\rm br} = 2249^{+456}_{-436}$ K and $T_{\rm br}^{3\sigma{\rm UL}} < 3102$ K when using the upper limit on the occultation depth. The large uncertainties of the brightness temperature and the high value of the upper limit do not lead to some clear conclusion about the planetary temperatures and a possible temperature contrast between the hemispheres.

OGLE-9 b, FORS2/z_GUNN+78: The derived brightness temperature for this filter is $T_{\rm br} = 2482^{+458}_{-473}$ K and when the upper limit on the occultation depth is used, we come to $T_{\rm br}^{3\sigma{\rm UL}} < 3326$ K. This temperature is much higher than the equilibrium temperature as above) and about 200 K higher than for the HAWK-I data obtained in a farther infrared bandass (1186 nm compared to 910 nm here). Due to high uncertainties and the high

upper limit it can not claimed with confidence that for the shorter near-infrared bandpass the brightness temperature is really higher suggesting an absorption source about 1.19 µm. Nevertheless, the results of the temperature differences are consistent with those obtained from the HAWK-I data, i.e. a temperature contrast may be present between the dayside and the nightside of the planet.

OGLE-9 b, TESS: When the value of the semi-major axis derived from the *TESS* data here is applied, we come to $T_{\rm eq} = 2014^{+101}_{-100}$ K which matches well $T_{\rm eq}$ using the adopted value (as in HAWK-I and FORS2). The obtained brightness temperature is $T_{\rm br} = 3511^{+296}_{-398}$ and when inferred from the upper limit, then $T_{\rm br}^{3\sigma{\rm UL}} < 3736$ K. It is a few hundred kelvins higher value than for the near-infrared wavelengths. If the brightness and equilibrium temperature are compared, we can see that $T_{\rm br}$ is about 1500 K higher than $T_{\rm eq}$. The results indicate that there may be a temperature contrast between the planetary hemispheres. Furthermore, an increasing trend of the brightness temperature with decreasing wavelength can be seen. Regrettably, the upper limit do not allow us to make a clear conclusion. The brightness temperature obtained in those three bandpasses, nevertheless, suggests that there is/are sources of absorption in the near-infrared, or possibly a source of emission in the *TESS* band resulting in the observed different brightness temperatures. In any case, the derived $T_{\rm br}$ from the *TESS* data remains consistent with those obtained for the longer wavelengths.

Heat redistribution

WASP-18 b, HAWK-I/NB1060: Knowing the brightness temperature, we can derive the heat redistribution (or flux correction) factor, which is $f = 0.370^{+0.248}_{-0.162}$. Using the upper limit on the brightness temperature, we come to a 3σ upper limit on the redistribution factor, $f^{3\sigma{\rm UL}} < 0.626$. This value lies between 1/4 and 2/3 for uniform redistribution and instantaneous reradiation, respectively. Albeit not to be a strict constraint, a physically plausible value was obtained. The value itself suggests nearly absolute instantaneous reradiation of heat between the planetary hemisphere and on the dayside but since it is an upper limit, it allows the real value to reach the possible minimum at the same time.

WASP-18 b, HAWK-I/NB2090: The brightness temperature implies the heat redistribution factor to be only $0.090^{+0.050}_{-0.071}$, or lower than 0.170 when the upper limit on the brightness temperature is used. This is not a physically reasonable value—it can be used to deduce that the redistribution factor lies on the lower end of the two limiting values, i.e. $f \approx 0.25$, but from these poor data no conclusion can be derived. Moreover, same as the previous derived atmospheric properties, the value indicates that the occultation depth itself is underestimated.

WASP-36 b, HAWK-I/NB2090: The 3σ upper limit on the brightness temperature leads to an upper limit on the heat redistribution factor, $f^{3\sigma{\rm UL}} < 0.592$. This is a reasonable result lying between the possible values. The value itself is close to the case of instantaneous reradiation of heat ($f = 2/3$) but as it is an upper limit, in real it can reach any value below the derived limit. If the heat redistribution factor is inferred from the obtained brightness temperature instead of its upper limit, we get $f = 0.254^{+0.160}_{-0.248}$ leading to no clear conclusion due to the high uncertainties.

WASP-43 b, HAWK-I/NB1060: The derived 3σ upper limit on the heat redistribution factor is $f^{3\sigma{\rm UL}} < 2.750$. This is a meaningless result implying that all reasonable values are allowed, i.e. $0.25 \lessapprox f \lessapprox 0.667$. This does not constrain the factor anyhow and therefore no conclusion can be deduced.

WASP-50 b, HAWK-I/NB2090: The derived brightness temperature leads to the heat redistribution factor $f = 0.655^{+0.338}_{-0.571}$ whilst the upper limit on $T_{\rm br}$ results in $f^{3\sigma{\rm UL}} < 1.386$.

This number is higher than an acceptable value and $f \lessapprox 0.667$ can only be claimed. Thus, no valuable constraint on f can be placed.

WASP-51 b, HAWK-I/NB2090: The obtained heat redistribution factor and its 3σ upper limit are $f = 0.325^{+0.217}_{-0.301}$ and $f^{3\sigma\mathrm{UL}} < 0.798$, respectively. Although the upper limit is not far from the maximum possible value, it gives us no specific result and it can be concluded that $f \lessapprox 0.667$.

WASP-51 b, TESS: The derived brightness temperature leads to the heat redistribution factor $f = 0.597^{+0.195}_{-0.277}$ and when using its upper limit, it results in $f^{3\sigma\mathrm{UL}} < 0.934$. This is, however, an unreasonable value and implies $f \lessapprox 0.667$ which is not a useful constraint.

OGLE-9 b, HAWK-I/NB1190: The heat redistribution factor of the planetary atmosphere is $f = 0.370^{+0.304}_{-0.291}$, or $f^{3\sigma\mathrm{UL}} < 1.340$ when the 3σ upper limit on the brightness temperature is applied in the derivation. The obtained upper limit on f is beyond the maximum meaningul value and it can only be concluded that $f \lessapprox 0.667$.

OGLE-9 b, FORS2/z_GUNN+78: The derived heat redistribution factor is $f = 0.549^{+0.411}_{-0.424}$ when using the derived brightness temperature. If its upper limit is used instead, it results in $f^{3\sigma\mathrm{UL}} < 1.770$. Since this upper limit is beyond the maximum possible value, no useful constraint can be placed and $f \lessapprox 0.667$ can only be claimed.

OGLE-9 b, TESS: The obtained 3σ upper limit on the heat redistribution factor is $f^{3\sigma\mathrm{UL}} < 2.961$. This is far from an acceptable value and it is a result of the high brightness temperature. Hence, also in this case $f \lessapprox 0.667$ can be claimed. To obtain a reasonable value of the redistribution factor, i.e. between 1/4 and 2/3, one would need to get T_{br} lying between ≈ 2000 and 2600 K for the uniform redistribution and instantaneous reradiation of heat, respectively. Although this is theoretially reachable considering the large uncertainties of the brightness temperature, it would be still based on the occultation non-detection.

Table 7: Derived 3σ upper limits on the occultation depths and atmospheric properties obtained from them, except for T_{eq}. These are shown for the systems analysed in this section. *Notes*: $^{(a)}$: calculated using Equation 2; $^{(b)}$: calculated using Equation 3 assuming $f = 1/4$ and $A_{\mathrm{B}} = 0$; $^{(c)}$: calculated using Equation 4; $^{(d)}$: calculated using Equation 6 assuming $A_{\mathrm{B}} = 0$. Quantities which resulted in unacceptable values are denoted with a dash.

Parameter (Unit)	WASP-18 NB1060	WASP-18 NB2090	WASP-36 NB2090	WASP-43 NB1060	WASP-50 NB2090
3σ up. limit on the depth, $\delta^{3\sigma\mathrm{UL}}_{\mathrm{occ;b}}$ (ppt)	< 0.853	< 0.844	< 1.847	< 2.781	< 2.100
Geometric albedo$^{(a)}$, $A_{\mathrm{g;b}}$	$\left(0.233^{+0.358}_{-0.365}\right)$	—	$\left(0.027^{+1.107}_{-1.114}\right)$	—	—
3σ upper limit on $A^{(a)}_{\mathrm{g;b}}$, $A^{3\sigma\mathrm{UL}}_{\mathrm{g;b}}$	(< 0.726)	(0)	—	—	—
Equilibrium temperature$^{(b)}$, $T_{\mathrm{eq;b}}$ (K)	2504^{+63}_{-65}	2504^{+63}_{-65}	1754 ± 42	1438^{+33}_{-30}	1411 ± 33
Brightness temperature$^{(c)}$, $T_{\mathrm{br;b}}$ (K)	2761^{+295}_{-458}	1939^{+265}_{-380}	1761^{+274}_{-428}	2251^{+239}_{-373}	1795^{+227}_{-389}
3σ upper limit on $T^{(c)}_{\mathrm{br;b}}$, $T^{3\sigma\mathrm{UL}}_{\mathrm{br;b}}$ (K)	< 3150	< 2274	< 2176	< 2620	< 2165
Heat redistribution factor$^{(d)}$, f_{b}	$0.370^{+0.248}_{-0.162}$	—	$0.254^{+0.160}_{-0.248}$	—	$0.655^{+0.338}_{-0.571}$
(3σ) upper limit on $f^{(d)}_{\mathrm{b}}$, $f^{(3\sigma)\mathrm{UL}}$	< 0.626	≈ 0.250	< 0.592	$\lessapprox 0.667$	$\lessapprox 0.667$

Parameter (Unit)	WASP-51 NB2090	WASP-51 *TESS*	OGLE-9 NB1190	OGLE-9 z_G.+78	OGLE-9 *TESS*
3σ up. limit on the depth, $\delta^{3\sigma\mathrm{UL}}_{\mathrm{occ;b}}$ (ppt)	< 1.278	< 0.109	< 1.183	< 1.040	< 1.582
Geometric albedo$^{(a)}$, $A_{\mathrm{g;b}}$	$\left(0.494^{+1.578}_{-1.471}\right)$	$0.144^{+0.131}_{-0.106}$	—	$\left(0.449^{+0.954}_{-0.461}\right)$	—
3σ upper limit on $A^{(a)}_{\mathrm{g;b}}$, $A^{3\sigma\mathrm{UL}}_{\mathrm{g;b}}$	—	< 0.367	—	—	—
Equilibrium temperature$^{(b)}$, $T_{\mathrm{eq;b}}$ (K)	1728 ± 32	1743 ± 41	2039 ± 65	2039 ± 65	2014^{+101}_{-100}
Brightness temperature$^{(c)}$, $T_{\mathrm{br;b}}$ (K)	1845^{+306}_{-425}	2166^{+169}_{-246}	2249^{+456}_{-436}	2482^{+458}_{-473}	3511^{+296}_{-398}
3σ upper limit on $T^{(c)}_{\mathrm{br;b}}$, $T^{3\sigma\mathrm{UL}}_{\mathrm{br;b}}$ (K)	< 2309	< 2423	< 3102	< 3326	< 3736
Heat redistribution factor$^{(d)}$, f_{b}	$0.325^{+0.217}_{-0.301}$	$0.597^{+0.195}_{-0.277}$	$0.370^{+0.304}_{-0.291}$	$0.549^{+0.411}_{-0.424}$	—
Upper limit on $f^{(d)}_{\mathrm{b}}$, f^{UL}	$\lessapprox 0.667$	$\lessapprox 0.667$	$\lessapprox 0.667$	$\lessapprox 0.667$	$\lessapprox 0.667$

Conclusions

WASP-18, HAWK-I/NB1060: The data revealed big systematics which caused the strong flux variance seen in the light curve. Hence, the occultation has not been clearly detected. From the uncertainties of the measurement a 3σ upper limit on the depth was placed and this was applied to derive upper limits on the NIR geometric albedo, the brightness temperature and the heat redistribution factor. The constraint placed on the albedo is consistent with a high value but rather than of reflected light, results obtained from measurements in the infrared are indicators of planetary thermal emission. The derived constraints on the remaining characteristics resulted in no valuable information since they allow more scenarios depending on the processes and the composition of the planetary atmosphere.

WASP-18, HAWK-I/NB2090: Strong systematics, same as in NB1060 data, caused that the occultation has not been detected with sufficient significance. Thus, 3σ upper limits on the occultation depth and the atmospheric properties were derived. However, they revealed that the resulting brightness temperature, the heat redistribution factor and even the occultation depth itself are ambiguous and contradict what is theoretically supposed. Moreover, the results do not fit what is expected considering the outcome of NB1060 data. The unexpected and underestimated occultation depth is presumably caused by the high level of red noise.

WASP-36 b, HAWK-I/NB2090: Since the the data suffer from strong systematics, the occultation has not been detected. From the fit an upper limit on the occultation depth was placed as well as on the brightness temperature and the heat redistribution factor. Regrettably, no conclusion about the planetary atmosphere could be derived from this data set.

WASP-43 b, HAWK-I/NB1060: Although the flux was relatively stable during the occultation, the event itself has not been detected. The systematics were still strong enough to measure the flux drop. Moreover, the occultation was observed only until the first third of its duration and thus the second part of the baseline is missing too. Despite this, upper limits on the occultation depth and the brightness temperature were placed, but they do not lead to any clear conclusion on an atmospheric property.

WASP-50 b, HAWK-I/NB2090: Even though the systematics were not so strong as in the HAWK-I data of WASP-18 and WASP-36, the occultation has not been clearly detected. An upper limit on the occultation depth was placed and consequently on the atmospheric properties, as for the previous planets. Nevertheless, they did not lead to any strict constraints.

WASP-51 b, HAWK-I/NB2090: The occultation has not been clearly detected due to systematics larger than the maximum expected depth. A strong effect of the variable seeing is obvious. From the uncertainties of the occultation model an upper limit on the depth was placed. This constraint then served to derive upper limits on the brightness temperature and the heat redistribution factor. Yet, the results did not give us any valuable and lucid information about the planetary atmosphere.

WASP-51 b, TESS: The measurement of the occultation has not resulted in a clear detection although the level of the contained noise is much lower than in the ground-based data. Thus, the non-detection is rather a result of the shallow occultation depth than of the contained noise. 3σ upper limits on the occultation depth, the geometric albedo and the brightness temperature were placed. The results allow that a temperature contrast between the planetary hemispheres may exist and that some part of the stellar radiation could be reflected by the planetary atmosphere.

OGLE-9 b, HAWK-I/NB1190: The occultation measurement led to placing a 3σ upper limit on its depth. In this case the non-detection was caused by both red noise and time-uncorrelated white noise—the parent star is the faintest of all the planetary systems studied in this thesis. Since the occultation upper limit is considerably greater than the expected depth, the derived geometric albedo, the brightness temperature and the heat redistribution factor did not result in valuable constraints.

OGLE-9 b, FORS2/z_ GUNN+78: Two particular data sets obtained in this filter were analysed but none of them led to a clear detection of the occultation due to correlated red noise. Moreover, uncorrelated white noise also played a role in the non-detection. A 3σ upper limit on the occultation depth for each of the data sets was placed and the lower one was applied to derive the atmospheric properties. But also here, no valuable constraints on the investigated characteristics could be placed.

OGLE-9 b, TESS: The photometric data are highly dominated by uncorrelated white noise. The *TESS* light curves were fitted together with adopted radial velocity data. The results show that the planetary orbit is consistent with a circular orbit. Concerning the occultation, a clear detection has not been reached. Therefore, a 3σ upper limit on the occultation depth and the studied atmospheric properties were placed. The upper limit on the occultation is relatively high and if the depth is truly of this order, it can not be explained purely by reflected light even if the planetary geometric albedo was at its peak value. This is not, however, what is expected for this planet type—an ultra-hot Jupiter. Rather, instead of the high albedo strong thermal emission is expected.

6. Determination of atmospheric properties

This section describes data sets which led to a successful occultation detection or resulted in a stringent constraint on the occultation depth. From the acquired depths, the same characteristics of the planetary atmospheres as in the previous section have been derived. Since most of the detections were reached from *TESS* data, studying the geometric albedo is an important part of the analysis of the atmosphere. An exception is WASP-43 system observed in the NIR bandpass. In this case, instead about the albedo, the successful detection gives us some information about the thermal emission of the planet.

6.1. The data sets

Data reduction and aperture photometry of the introduced data sets have been performed as described in Section 4.2.3 (*TESS*) and Section 4.3.1 (HAWK-I). For calculations of the RMS_w and the display purpose, the *TESS* data sets were period-folded resulting into phase curves. Basic characteristics of all the observational runs described below are shown in Table 8, raw *TESS* light curves are displayed in Figure 14 and binned phased light curves in Figure 15. All important measures of the observation of WASP-43/HAWK-I together with the binned light curve are plotted in Figure 16.

WASP-18 b, *TESS*

The *TESS* data set counts in total four individual data sets obtained between August 2018 and October 2020, observed in *TESS* sectors 2, 3, 29 and 30. They include 95 orbits of the planet around its host star. There is a feature suggestive of a stellar flare in the transit. However, after some inspection it was found that it is not of stellar origin—during the observed 82^{nd} and 83^{rd} transit, at JD $\approx$ 2127.37 and JD $\approx$ 2130.24, *TESS* stopped to observe (to transmit data to the Earth at the perigee of its orbit) and this observational gap corresponds to exactly three orbital periods. The resulting feature is, thus, an instrumental feature plus the transit events.

WASP-36 b, *TESS*

The data set counts two individual data sets obtained between February 2019 and February 2021 and observed in *TESS* sectors 8 and 34. The data include about 27 orbits of the planet around its parent star.

WASP-43 b, HAWK-I/NB2090

This data set was obtained during an observational night on 9^{th} December 2010 (JD = 2,455,539) by using Generic Offset Mode/Template of HAWK-I through NB2090 filter. Three comparison stars were observed together with the target star.

During the observation airmass was decreasing as the target star was rising through the whole observation and almost reaching the zenith. Coherence time and seeing were strongly varying, especially in the second half corresponding to the occultation itself, albeit in acceptable values (seeing around 1″). Positions of the target star on the detector were fluctuating only slightly—within a range of six pixels for both X and Y axis, but they did not have a significant effect on the obtained light curve. What did have an effect on

the light curve was the decreasing airmass leading to gradual increasing of the measured flux.

WASP-43 b, *TESS*

This data set counts two individual data sets which were obtained between February 2019 and March 2021 and observed in *TESS* sectors 9 and 35. The overall data set includes about 50 orbits of the planet around its star.

WASP-50 b, *TESS*

The two individual data sets contained in these data were obtained between October 2018 and November 2020 and observed in *TESS* sectors 4 and 31. The whole data set includes about 23 orbits of the planet around its parent star.

Table 8: Properties of the data sets studied in this section. The designation is the same as in Table 3.

Sector	N_{dp}	$\mathrm{Date}_{\mathrm{beg}}$	$\mathrm{Date}_{\mathrm{end}}$	$\mathrm{JD}_{\mathrm{beg}}$	$\mathrm{JD}_{\mathrm{end}}$	Days
			WASP-18, TESS			
2	18,316	23/08/18	20/09/18	2,458,353.5	2,458,382.5	29
3	12,864	21/09/18	17/10/18	2,458,382.5	2,458,409.5	27
29	14,361	26/08/20	21/09/20	2,459,087.5	2,459,114.5	27
30	16,573	23/09/20	20/10/20	2,459,115.5	2,459,143.5	28
All:	**62,114** |			**Days of the observation in total:**		**111**
			WASP-36, TESS			
8	13,420	02/02/19	27/02/19	2,458,516.5	2,458,542.5	26
34	16,838	14/01/21	08/02/21	2,459,228.5	2,459,254.5	26
All:	**30,258** |			**Days of the observation in total:**		**52**
			WASP-43, TESS			
9	15,602	28/02/19	25/03/19	2,458,542.5	2,458,568.5	26
35	13,661	09/02/21	06/03/21	2,459,254.5	2,459,280.5	26
All:	**29,263** |			**Days of the observation in total:**		**52**
			WASP-50, TESS			
4	14,658	19/10/18	14/11/18	2,458,410.5	2,458,437.5	27
31	16,155	22/10/20	18/11/20	2,459,144.5	2,459,172.5	28
All:	**30,813** |			**Days of the observation in total:**		**55**

WASP-43, HAWK-I/NB2090

τ_{int} (s)	N_{FF}	N_{ax1} (px)	N_{ax2} (px)	t_{first} (UTC)	t_{last} (UTC)
1.7	184	2048	2048	05.37:57	09.06:27
				$\boldsymbol{t_{\mathrm{total}} = 3\,\mathrm{h}\ 28\,\mathrm{min}\ 30\,\mathrm{s}}$	

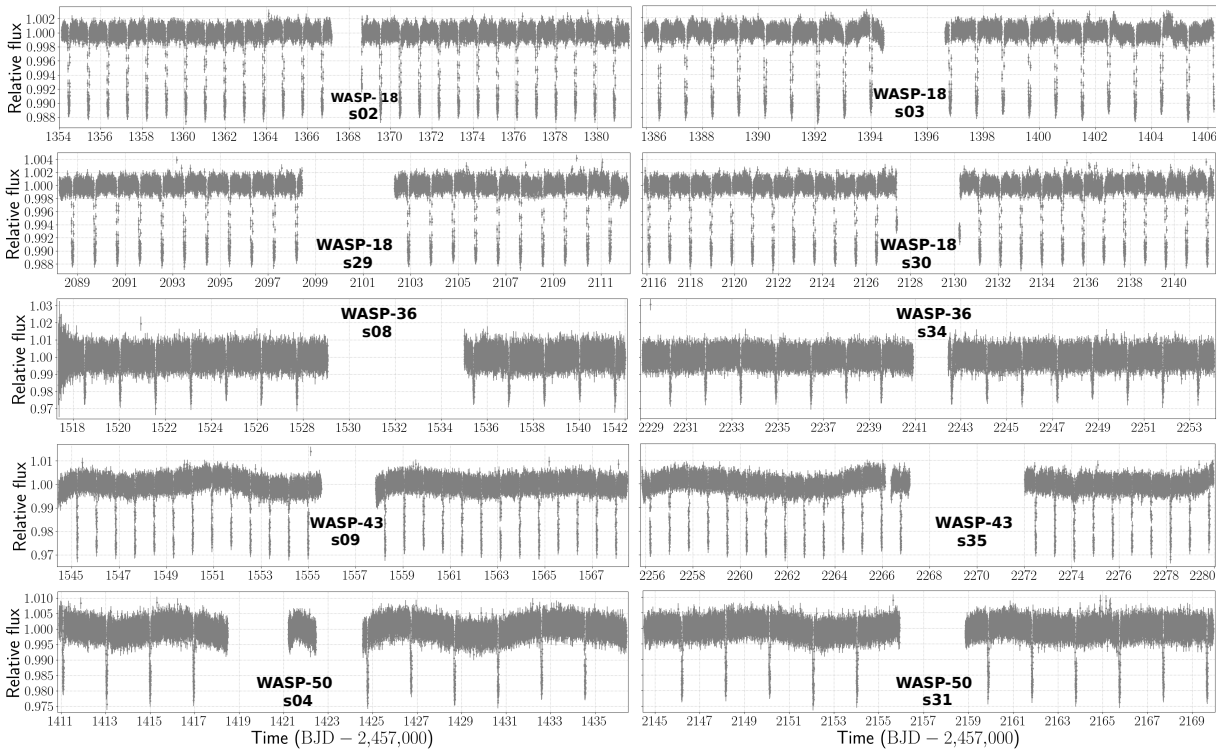

Figure 14: Raw light curves of the systems studied in this section, obtained by *TESS*. Primary transits are clearly visible as well as flux modulation of WASP-43 and WASP-50.

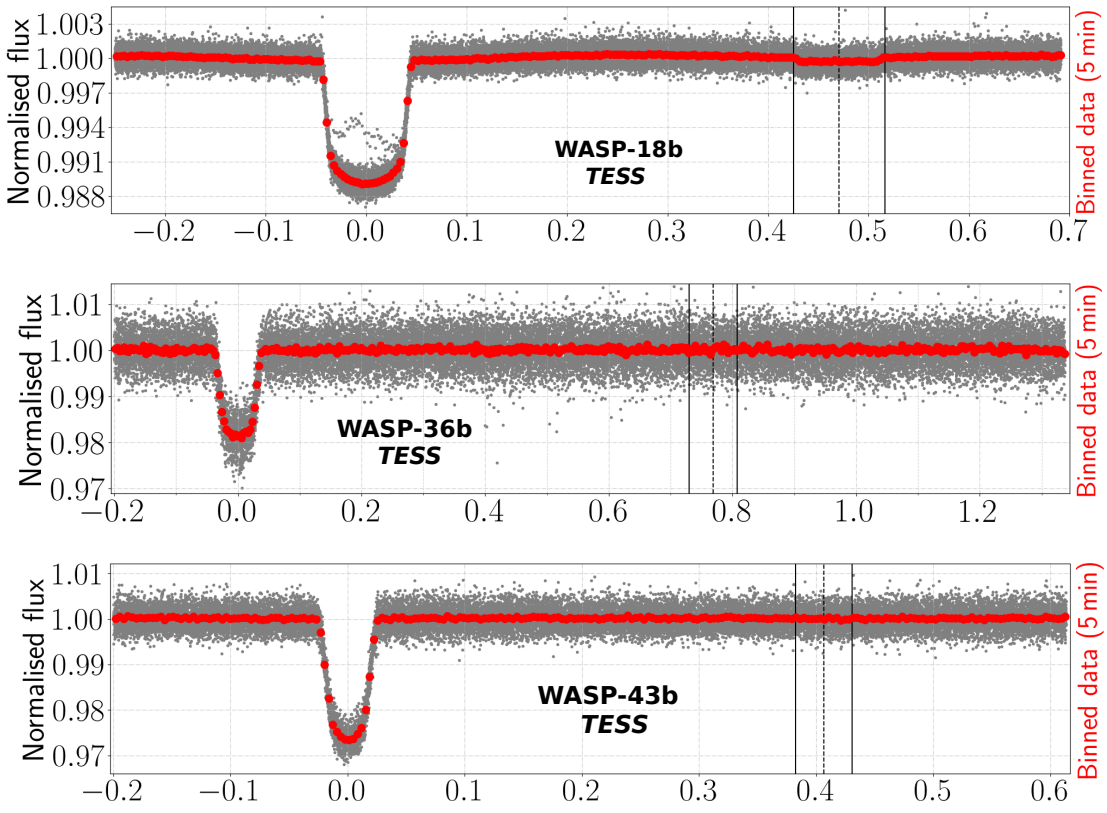

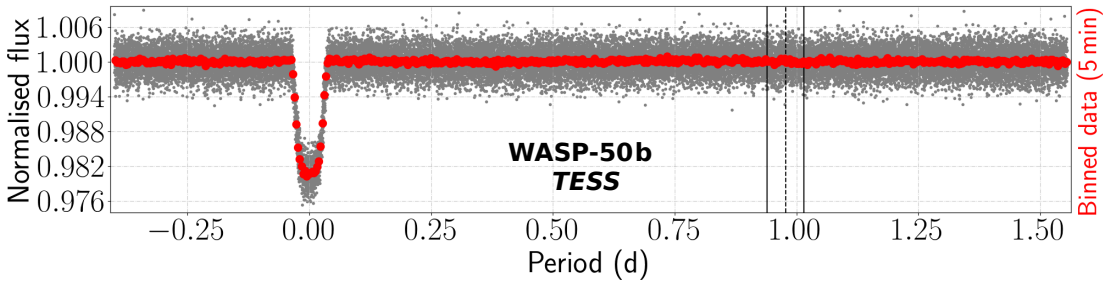

Figure 15: Period-folded *TESS* light curves of the systems studied in this section. Meaning of the used symbols and curves is the same as in Figure 11.

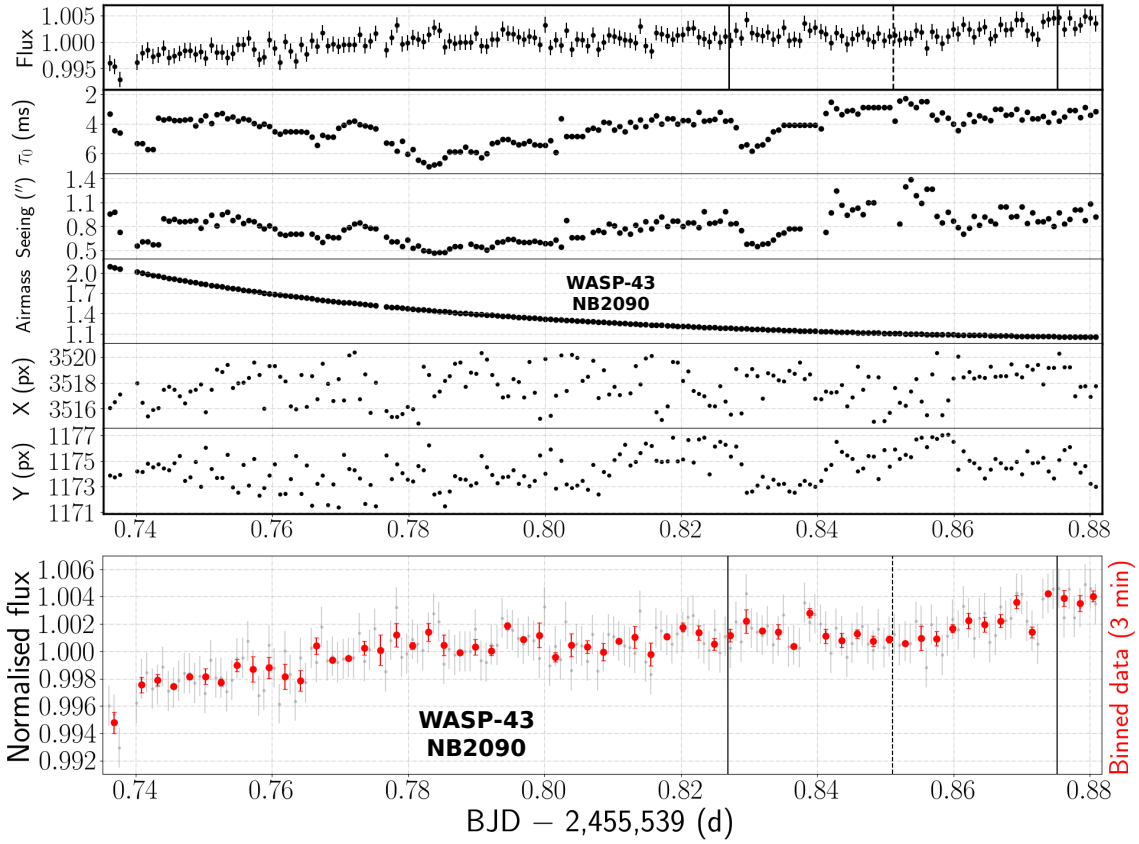

Figure 16: WASP-43, HAWK-I/NB2090. *The upper plot*: the panels are as in Figure 9; *the bottom plot*: the meaning of the symbols is as in Figure 11.

6.2. Data analysis and results

In what follows, the results obtained for each planetary system are described. A possible detection of the occultation in the analysed data sets was theoretically estimated as described in Section 4.5. The resulting values are listed in Table 9. The posterior values of the fitted and derived parameters are summarised in Table 10. Eventually, plots of the analysed light curves together with their best-fitting models are shown in Figure 17.

Stellar variability

The data sets of WASP-43 and WASP-50 reveal noticable flux modulation not caused by their planet or by the interaction between the star and the planet. Therefore, besides the default kernel (GP Matérn 3/2) Simple Harmonic Oscillator (SHO) kernel was also used to fit the baseline, depending on the approach of the individual fit. The supposed stellar

variability was investigated using three approaches: each of the two sectors analysed individually, both sectors together considered as from two instruments, and both sectors regarded as a single data set. For each of the *TESS* sectors, plots representing fits of the flux modulation due to stellar variation of these stars are shown in Figure 18.

WASP-43 b, TESS: When the data of each sector were fitted separately, the resulting values of the stellar rotational period using broad priors differed significantly—$P_{\mathrm{rot}} = 7.373$ and 1.307 days for sector 9 and 35, respectively. The fits of both the sectors altogether gave P_{rot} of 1.32 and 1.256 d, respectively for fits of data as from two instruments and as a single data set. We can see the the period of ≈ 1.3 d is prevailing; however, values of the amplitude of the flux modulation are not so consistent.

The fits were also performed with prior-constrained amplitude and period according to the work of Hellier et al. (2011) who found with very high significance a modulation period of 15.6 ± 0.4 d together with the first harmonic of 7.8 d in WASP-South data. The amplitude of the modulation presented in their work is $\Delta m = 0.006 \pm 0.001$ mag which corresponds to $\Delta F = 0.0055 \pm 0.0009$ of the relative flux. The supposed periods were found in particular fits herein too but these fits were not favoured over those with broad priors. Especially the fits with the supposed stellar rotational period of 15.6 d are unfavoured. Regarding the amplitude of the flux modulation, for the prior-constrained periods the obtained amplitude is consistent with what has been found by the authors of the mentioned work. Yet, it must be noted that the prior bounds were set relatively narrow as they were estimated from the shape of the phase curve.

To conclude the results of the analyses from all the relevant fits, no convincing detections of the rotational period and the amplitude of the stellar variability were obtained. In the work of Hellier et al. (2011) a possibility of a beat period between the true period and the one-day sampling is mentioned. However, the period/first harmonic are most likely real and the fact that a periodical flux-modulation pattern caused by the star was not clearly detected in these data is caused by several factors: the stellar variability is not strong and hence not the amplitude, the scatter of the photometric data is relatively high, and there is little data (short time range of the observations) to accurately determine the stellar rotational period, supposing it is not shorter than 7.8 days.

The results of the individual fits of each sector suggest that the *TESS* observations did not measure the star during the same phase of its variability as the derived values of S_0, Q and also ω_0 differ significantly. This could also explain the slight inconsistency of the derived transit depth with those published in some works where different data obtained in a different phase of the stellar variabilty were used. What stands against this explanation is the fact that the measured transit depths of both the sectors match well. If the brightness of the star changed from the first *TESS* measurement to the second one, the transit depth would be therefore expected to change as well. The activity of the star using *TESS* data was also studied by Scandariato et al. (2022) who came to a similar conclusion. On the other hand, Gillon et al. (2012) pointed out an apparent transit variability that may be caused by the variability of the parent star.

A more detailed analysis, supposing e.g. stellar spots, present at different latitudes, could solve this issue and find the main variability characteristics of the star. Yet, such an analysis is beyond the scope of this thesis. What can be claimed without any doubts is that moderate variability of the star really exists.

WASP-50 b, TESS: When the light curve of each *TESS* sector was fitted separately, then using broad priors on stellar-variability parameters the obtained stellar rotational period is 5.3 and 0.057 days for sector 4 and 31, respectively. If the light curves of both the sectors were fitted together, then the period is 4.63 and 22.32 days, respectively for fits as data of two instruments and of only one. These are strongly inconsistent

results. Moreover, the derived amplitude of the last mentioned fit is inconsistent with the amplitude obtained from the other fits.

This non-detection does not necessarily imply that no stellar variation of this star exists. Rather, it is a consequence of the relatively long rotational period combined with noise included in the data. Since a stellar rotational period of 16.3 ± 0.5 d has already been found (Gillon et al., 2011), it was used to constrain its prior value and bounds for other fits. These resulted in $P_{\rm rot}$ of 16.32, 16.28, 16.30 and 16.33 days for the fits of the same order as in the previous paragraph. The obtained periods match very well and also with the published period. The derived amplitudes does not perfectly match but they are still consistent within 2σ.

The fits with broad priors were mostly preferred over those with narrow priors albeit very slightly. A clear conclusion about the stellar rotational period, therefore, can not be made from these outcomes although the period of 16.3 d seems probable. This analysis is based on two 28-days data sets within 762 days. In contrast to this, the team of the above-mentioned publication analysed data of 110- and 80-days observing seasons within 460 days. This points that their data had much better prospect to reveal the stellar period than these *TESS* data.

Planetary orbit

WASP-18 b, TESS: To fit this data set, Sample Offset baseline kernel was applied. The obtained value of eccentricity is $e = 0.0024^{+0.0023}_{-0.0011}$ which is not well constrained, only around 1σ significance. Using *Spitzer* infrared data, Nymeyer et al. (2011) derived $e = 0.0091 \pm 0.0012$. If a 3σ upper limit on the herein derived eccentricity is considered, we obtain $e < 0.0069$ which is still within 3σ with their value. The obtained value of the argument of periastron is well constrained, $\omega = 266.9^{+2.0}_{-2.2}$ deg, and is consistent with $\omega = 269 \pm 3$ deg of Nymeyer et al. (2011) at 1σ significance level.

WASP-36 b, TESS: The fits were performed on the unbinned and on 20-min-binned data—with eccentricity both as a free and as a fixed parameter. The two fits were then compared using the Bayesian evidence. For the unbinned data, the fit with the zero-fixed eccentricity was favoured whilst for the binned data this setting was slightly unfavoured. The resulting values of the orbital parameters are $e = 0.00025^{+0.00018}_{-0.00017}$ and $\omega = 181.4^{+123.2}_{-128.6}$ deg. This leads to a 3σ upper limit on the eccentricity, $e^{3\sigma{\rm UL}} < 0.00055$, but for the argument of periastron no reasonable constraint can be placed. This is consistent the with zero eccentricity obtained from the unbinned data and also found by Maciejewski et al. (2016) as well as with $e^{3\sigma{\rm UL}} < 0.0663$ of Smith et al. (2012b).

WASP-43 b, TESS: The original unbinned data did not lead to a clear detection of the planetary orbital eccentricity and the argument of periastron. The derived values from the fit are $e = 0.0059^{+0.0140}_{-0.0047}$ and $\omega = 278^{+\ 26}_{-190}$ deg. The uncertainty of the eccentricity implies a 3σ upper limit, $e^{3\sigma{\rm UL}} < 0.042$, whilst for the argument of periastron no constraint can be placed. When the GP baseline was used to fit the binned data per 20 minutes, both these parameters were detected with higher than 3σ significance: $e = 0.050^{+0.014}_{-0.011}$ (consistent with $e^{3\sigma{\rm UL}}$) and $\omega = 280.8^{+5.2}_{-4.4}$ deg.

For a comparison of the obtained results with already published values of e and ω, several works can be chosen: Hellier et al. (2011) claim compatibility with zero eccentricity and put $e^{3\sigma{\rm UL}} < 0.04$, Smith et al. (2012b) put $e^{3\sigma{\rm UL}} < 0.0663$, Gillon et al. (2012) derived $e = 0.0035^{+0.0060}_{-0.0025}$, put $\mathrm{e}^{3\sigma{\rm UL}} < 0.0298$ and inferred $\omega = 328^{+115}_{-\ 34}$ deg, and Davoudi et al. (2021) admitted that very small eccentricity is possible. The results of these works agree with the low eccentricity derived herein showing that the orbit is not perfectly circularised.

WASP-50 b, TESS: The most precise value of the eccentricity of the planetary orbit obtained from the performed fits is $e = 0.0309^{+0.0089}_{-0.0073}$. The value is consistent with upper limits derived from fits where the eccentricity was not clearly detected as well as with the poor detection of Gillon et al. (2011) having inferred $e = 0.009^{+0.011}_{-0.006}$. Regarding the argument of periastron, it was not inferred with sufficient significance. For the discussed fit, $\omega = 38.5^{+299.4}_{-24.8}$ deg. This parameter has not been precisely measured yet as the only study (above) led to $\omega = 44^{+62}_{-80}$ deg.

The analysis implies that the planetary orbit is not perfectly circularised as usually expected in studies of this system. This assumption is reasonable in some cases but it is not appropriate for searching for occultation events. Indeed, the difference between the time of the occultation for zero and the non-zero eccentricity for the given planetary orbital period is about 45 minutes ($\Delta t_{\mathrm{occ}} = \frac{P}{2}\left[\frac{4e\cos\omega}{\pi}\right] \approx 0.0314$ d).

Phase curve variations

WASP-18 b, TESS: As seen in the light curve, the phase curve exhibits obvious phase variations. A phase curve can be generally modulated by three main contributors: Doppler-boosting (or beaming), atmospheric modulation and ellipsoidal modulation. Each of them contributed to the resulting shape of the phase curve but the ellipsoidal and the atmospheric modulation had the strongest effect. The former indicates that there is an obvious interaction between the star and the planet. The latter, which is important for the scope of this thesis, implies a semi-amplitude of 0.1535 ± 0.0044 ppt. The resulting number is generally a sum of the reflected light plus the thermal emission and a more thorough study can provide insight into the planetary atmosphere. But for a hot-Jupiter type planet, the thermal radiation is expected to dominate. The value itself is consistent with that of Günther & Daylan (2021) and slightly inconsistent with that of Shporer et al. (2019).

WASP-36 b, TESS: Two of the phase curve modulators have been detected: the atmospheric and the ellipsoidal modulation; the latter has a higher amplitude and implies an interaction between the planet and the star causing the star to deform. The semi-amplitude of the flux variation due to the planetary atmosphere is $0.074^{+0.018}_{-0.023}$ ppt. This is a half of the amplitude of WASP-18 b and it is probably a result of the much higher temperature than of WASP-36 b.

WASP-43 b, TESS: None of the contributors to the phase curve modulation was found with 3σ or higher significance when using SHO kernel to fit the baseline. If the GP-baseline was applied on the 20-min-binned data, it resulted in the detection of the ellipsoidal modulation of 0.155 ± 0.040 ppt. This shows that the parent star is tidally distorted by the gravity of the planet due to their mutual closeness. The distance between the planet and the star is the shortest of all the systems studied in this thesis ($a \approx 0.015$ AU).

WASP-50 b, TESS: In this case, no fit led to a convincing detection of a contributor to the phase curve modulation.

Occultation and transit depth

WASP-18 b, TESS: The expected occultation depth was calculated as the sum of the reflected light and thermal emission. The theoretical value of the thermal emission is 0.093 ppt. However, Shporer et al. (2019) in their work used the atmospheric model of Arcangeli et al. (2018) to get the thermal contribution of 0.327 ppt. They obtained this value by fitting *HST* and *Spitzer* occultation data. As this is a more proper procedure, their value was adopted for the further analysis. Furthermore, since hot Jupiters generally

exhibit low geometric albedos, the assumed $A_g = 0.1$ implying a total expected occultation depth of 0.406 ppt is a more appropriate value than $A_g = 1$.

The theoretical depth was compared with RMS_w of the unbinned and binned data. Since the phase curve exhibits strong phase variations of real physical origin, the RMS_w derived on some time intervals is significantly lower. The estimated expected depth and the obtained RMS_w of the data suggest that the occultation should be clearly detected in the data.

The inferred values of the transit and occultation depth are $\delta_{tra} = 10.614 \pm 0.015$ ppt and $\delta_{occ} = 0.346 \pm 0.011$ ppt, respectively, which are clear detections. The obtained values are consistent with results obtained by Shporer et al. (2019) at 3σ or better. Note that the derived occultation depth is very close to the theoretical estimate. There is a difference between the values of the transit depth—the authors inferred $\delta_{tra} = 9.439^{+0.027}_{-0.026}$ ppt which is 89 % of the value obtained herein. However, since they calculated the transit depth as $R_b^2/R_\star^2$, the obtained depths are not contradictory as for non-equatorial transits they may differ. Moreover, the discrepancy between the obtained values may come from using different methods and also from the fact that they used data only from two *TESS* sectors (2+3) whilst for the analysis in this thesis data of four sectors were used.

WASP-36 b, TESS: The comparison of the obtained RMS_w with the expected value of the occultation depth implies that the occultation may be detected in the data but only when they are binned. Further, A_g equal to one was supposed for this possible detection. On the other hand, a scenario with a negligible albedo but with thermal radiation stronger than of a blackbody is possible. Indeed, an example of this scenario is WASP-18 b.

The derived occultation depth of the unbinned data is $\delta_{occ} = 0.121^{+0.064}_{-0.059}$ ppt which leads to a 3σ upper limit on the occultation depth, $\delta_{occ}^{3\sigma UL} < 0.192$ ppt. Fitting of the 20-min-binned data, however, resulted in $\delta_{occ} = 0.180^{+0.047}_{-0.053}$ ppt which is the first clear detection in the *TESS* band (3.4σ). Wong et al. (2020) derived from *TESS* (using data of only sector 8, available at that time) an occultation depth of $0.09^{+0.10}_{-0.07}$ ppt which is consistent with the inferred depth and also with the placed upper limit. The flux drop in this bandpass is typically caused by optical scattering of incident radiation. The planetary thermal emission was detected at a NIR wavelength of 2.144 µm by Zhou et al. (2015) who derived, using Ks band, an occultation depth of 1.3 ± 0.4 ppt. The above-mentioned results suggest that the occultation depth is more pronounced in the NIR than in the visible band. This is in agreement with what is expected for hot Jupiters.

The inferred transit depth is $\delta_{tra} = 18.305^{+0.145}_{-0.147}$ ppt. This value is lower than 19.16 ± 0.20 ppt of Smith et al. (2012b) obtained in the visible band and also than 19.35 ± 0.32 ppt of Maciejewski et al. (2016), however obtained in the R band. Yet, the value inferred here is consistent with that of the unbinned data and with 18.71 ± 0.15 ppt of Mancini et al. (2016) obtained with using Sloan filters g', r', i', z'. This photometric systems covers a similar wavelength range (475–905 nm) to the range of *TESS*. As was pointed out by Mancini et al. (2016), observations show variation of the planetary radius with wavelength. This is probably the primary reason of the differences in the derived transit depths.

WASP-43 b, HAWK-I/NB2090: Since these data are less affected by systematics than the remaining ground-based data, the comparison of the expected depth with RMS_w of the binned data implies that the occultation could be detected, even for a low albedo value. As the measured flux exhibits a constant increase with time, a more relevant approach is to calculate the RMS_w at some short time intervals. By doing that, the derived RMS_w is reduced to roughly a third of the expected depth.

The best fit of the 3-min-binned light curve resulted in an occultation depth $\delta_{occ} = 1.473^{+0.213}_{-0.214}$ ppt. It is is nearly a 7σ detection and is consistent with the result of the unbinned curve within 0.5σ, within 1σ with the work of Blažek et al. (2022), or within

0.4σ with the work of Gillon et al. (2012), both using 2-min bins. The derived depth also matches between the expected depths for a low and high geometric albedo. But for this wavelength of observation, instead of the high level of reflected light strong thermal emission is presumed.

WASP-43 b, TESS: When the calculated $\mathrm{RMS_w}$ values are compared with the highest expected occultation depth, we see that using binned data we could reach detection of the occultation as the expected depth is roughly an order greater than the $\mathrm{RMS_w}$. Nevertheless, a more realistic assumption of the albedo, i.e. $A_\mathrm{g} = 0.1$, leads to similar values of the expected depth and the $\mathrm{RMS_w}$ of the binned data and, thus, marginal detection depending on the exact physical depth.

The used approaches to fit the data resulted in occultation depths varying between 0.136 and 0.193 ppt but all were derived with low sigma significance. The best obtained posterior value of the occultation depth was reached from a fit applying SHO (stellar variability) baseline and fitting all the data as a single data set. It led to $\delta_\mathrm{occ} = 0.153^{+0.058}_{-0.053}$ ppt. Since it is only $\approx 2.6\sigma$ significance, a 3σ upper limit was placed, $\delta_\mathrm{occ}^{3\sigma\mathrm{UL}} < 0.175$ ppt.

The measured occultation depth varies when values of individual sectors are compared, showing that the value of the depth for sector 9 is lower than for sector 35. Regrettably, the occultation detections are poor and, thus, it can not be claimed that this variance is of astrophysical origin. Rather, the inconsistency in the occultation depths should be supposed as a result of noise present in the data and/or the stellar variability.

The derived upper limit is consistent with the published works: using *TESS* data, Wong et al. (2020) derived $\delta_\mathrm{occ} = 0.17 \pm 0.07$ ppt (sector 9) and Blažek et al. (2022) obtained $\delta_\mathrm{occ} = 0.12^{+0.06}_{-0.05}$ ppt and placed $\delta_\mathrm{occ}^{3\sigma\mathrm{UL}} < 0.161$ ppt (sectors 9 and 35). For the i' band (similar central wavelength as *TESS*), Chen et al. (2014) derived $\delta_\mathrm{occ} = 0.37 \pm 0.22$ ppt.

The derived transit depth is $\delta_\mathrm{tra} = 26.617^{+0.078}_{-0.073}$ ppt and matches the transit depths obtained using all approaches within 1σ. Even though slight transit-depth variability was found in this planetary system by Gillon et al. (2012), no indication of such a phenomenon was found here. But as previously mentioned, the possible modulation in transit depths depends on the current phase of the variability cycle of the host star.

WASP-50 b, TESS: The comparison of the expected depth with the obtained $\mathrm{RMS_w}$ shows that we could detect the occultation in a case of a high geometric albedo and using binned data since the values are comparable. However, a lower albedo is more likely (theoretical thermal emission is negligible) and thus an occultation depth of a tenth of ppt is preferred to expect. Therefore, a clear detection can not be achieved unless the contribution of scattered light is significant.

The best obtained value of the occultation depth is $\delta_\mathrm{occ} = 0.199^{+0.057}_{-0.060}$ ppt. This is the only case when the value itself exceeded 3σ and thus reached sufficient significance. In this fit the GP baseline instead of SHO baseline was applied. From other fits 3σ upper limits were placed. The inferred values of the occultation depth for each sector slightly indicate that the depth could have changed between the *TESS* observational runs or that it varies with time. However, the signal is too weak to prove such variations.

The occultation depth and the upper limits are consistent with the work of Blažek et al. (2022) who, using the same *TESS* data, placed $\delta_\mathrm{occ}^{3\sigma\mathrm{UL}} < 0.149$ ppt from the obtained $\delta_\mathrm{occ} = 0.117^{+0.051}_{-0.048}$ ppt. The difference comes mainly from the applied noise model as they did not use a GP baseline to model the noise. Secondly, they fitted a phase-folded light curve whilst in this analysis the original (unfolded) light curve was modelled. There are no other works studying occultations of WASP-50 b which could be used for a more thorough comparison of the obtained depths.

The obtained transit depth of the GP-baseline fit is $19.586^{+0.090}_{-0.091}$ ppt. It agrees very well with each transit depth derived using other approaches (SHO kernel). It is also

consistent with previous studies of this system, such as Gillon et al. (2011) and Blažek et al. (2022). It is not perfectly consistent with the result of Tregloan-Reed & Southworth (2013) since they inferred $R_b/R_\star$ and the transit depth was calculated from this ratio.

Table 9: Expected occultation depths of planet 'b' and RMS_w of the data sets of the systems studied in this section. *Notes*: [(a)]: calculated from Equation 7 supposing blackbody radiation of both the objects; [(b)]: calculated from Equation 8 supposing $A_g = 1$ or $A_g = 0.1$; [(c)]: adopted from Arcangeli et al. (2018) as in Shporer et al. (2019); [(d)]: binned per 20 minutes; [(e)]: 3-min intervals; [(f)]: binned per 3 minutes; [(g)]: 9-min intervals.

Occultation depth (ppt)	WASP-18 *TESS*	WASP-36 *TESS*	WASP-43 NB2090	WASP-43 *TESS*	WASP-50 *TESS*
Expected depth due to thermal emission[(a)]	0.093	0.014	0.781	0.007	0.002
Expected depth due to thermal emission[(c)]	0.327	—	—	—	—
$A_g = 1$:					
Expected depth due to reflected light[(b)]	0.791	0.576	1.049	1.049	0.349
Total expected depth[(a)(b)]	0.884	0.590	1.830	1.055	0.351
Total expected depth[(b)(c)]	1.118	—	—	—	—
$A_g = 0.1$:					
Expected depth due to reflected light[(b)]	0.079	0.058	0.105	0.105	0.035
Total expected depth[(a)(b)]	0.172	0.072	0.886	0.112	0.037
Total expected depth[(b)(c)]	0.406	—	—	—	—
Data used for calculation (ppt)					
Unbinned data, all	—	—	1.962	—	—
Unbinned data (out of transit & occultation)	0.607	3.417	2.013	2.208	2.057
Unbinned data (—"—), 1-min intervals	0.540	3.227	0.757[(e)]	2.153	1.935
Binned per 3 minutes, all	—	—	0.859	—	—
Binned per 5 minutes (out of trans & occult)	0.149	0.408	0.604[(f)]	0.181	0.257
Binned per 5 minutes (—"—), 20-min interv.	0.024	0.257	[(f)]0.312[(g)]	0.125	0.164
Unbinned data, best-fitting model residuals	0.599	0.205[(d)]	0.017[(f)]	2.205	1.815

Table 10: The input parameters and posterior values of the derived parameters of the *TESS* data sets analysed in this section, with the exception of $^{(H)}$ superscripted set which denotes HAWK-I/NB2090 data. Parameters with no given uncertainties were fixed during the fit.

Parameter (Unit)	WASP-18 b	WASP-36 b	WASP-43 b$^{(H)}$	WASP-43 b	WASP-50 b
Planet–star radii ratio, $R_\mathrm{b}/R_\star$	$0.096\,84^{+0.000\,13}_{-0.000\,14}$	$0.131\,99 \pm 0.000\,79$	$0.160\,99$	$0.158\,23 \pm 0.000\,38$	$0.136\,82^{+0.000\,49}_{-0.000\,47}$
Sum of radii over semi-major axis, $(R_\mathrm{b} + R_\star)/a_b$	0.3108 ± 0.0015	$0.2027^{+0.0032}_{-0.0031}$	$0.233\,52$	$0.2429^{+0.0022}_{-0.0029}$	0.1553 ± 0.0017
Cosine of inclination angle, $\cos i_b$	$0.0920^{+0.0044}_{-0.0050}$	0.1243 ± 0.0041	$0.128\,10$	$0.1422^{+0.0027}_{-0.0035}$	0.0976 ± 0.0021
Epoch of transit, $T_{0;\mathrm{b}}$ (d; $\mathrm{BJD_{TDB}} - 2{,}457{,}000$)	$1354.457\,906\,(25)$	$1518.505\,321^{+0.000\,272}_{-0.000\,279}$	$2{,}455{,}540.257\,819$	$1545.230\,517\,(46)$	$1411.093\,076\,(110)$
Planetary orbital period, P_b (d)	$0.941\,452\,472\,(43)$	$1.537\,365\,99\,(80)$	$0.813\,474\,37$	$0.813\,474\,032\,(72)$	$1.955\,093\,10\,(40)$
Orbital eccentricity term, $\sqrt{e_\mathrm{b}}\cos\omega_\mathrm{b}$	$-0.0028^{+0.0018}_{-0.0015}$	$-0.000\,16^{+0.013\,61}_{-0.013\,33}$	0.050	0.024 ± 0.021	$0.153^{+0.018}_{-0.031}$
Orbital eccentricity term, $\sqrt{e_\mathrm{b}}\sin\omega_\mathrm{b}$	$-0.048^{+0.013}_{-0.020}$	$-0.000\,15^{+0.013\,51}_{-0.013\,52}$	-0.031	$-0.068^{+0.070}_{-0.065}$	$-0.072^{+0.069}_{-0.079}$
Surface brightness ratio, J_b	$0.0041^{+0.0011}_{-0.0012}$	$0.0017^{+0.0024}_{-0.0012}$	0.057 ± 0.008	$0.0031^{+0.0026}_{-0.0020}$	$0.0040^{+0.0040}_{-0.0028}$
Limb darkening coefficient, q_1	0.320 ± 0.013	$0.428^{+0.016}_{-0.031}$	0.0	$0.534^{+0.019}_{-0.018}$	0.4394 ± 0.0058
Limb darkening coefficient, q_2	0.178 ± 0.013	$0.171^{+0.021}_{-0.036}$	0.0	0.118 ± 0.019	0.1389 ± 0.0089
Doppler-boosting semi-amplitude, $A_{\mathrm{b;beaming}}$ (ppt)	$0.0315^{+0.0033}_{-0.0035}$	$0.033^{+0.028}_{-0.022}$	—	$0.039^{+0.034}_{-0.026}$	$0.037^{+0.035}_{-0.026}$
Atmospher. modulation ampl., $A_{\mathrm{b;atmospheric}}$ (ppt)	0.3069 ± 0.0087	$0.147^{+0.035}_{-0.046}$	—	$0.064^{+0.055}_{-0.041}$	$0.106^{+0.074}_{-0.067}$
Ellipsoidal modulation ampl., $A_{\mathrm{b;ellipsoidal}}$ (ppt)	0.3487 ± 0.0091	$0.232^{+0.040}_{-0.042}$	—	0.112 ± 0.048	$0.022^{+0.028}_{-0.016}$
Stellar variability, amplitude, $\ln S_0$	—	—	—	$-10.51^{+1.45}_{-0.70}$	$-6.78^{+0.30}_{-0.16}$
Stellar variability, damping component, $\ln Q$	—	—	—	$-3.29^{+0.32}_{-0.59}$	$-2.74^{+0.16}_{-0.19}$
Stellar variability, angular frequency, $\ln\omega_0$	—	—	—	$1.61^{+0.16}_{-0.27}$	-0.96 ± 0.02
White noise error scaling, $\ln\sigma_F$	-7.4199 ± 0.0028	$-7.560^{+0.092}_{-0.105}$	$-8.472^{+0.978}_{-4.287}$	$-6.3084^{+0.0041}_{-0.0040}$	-6.3095 ± 0.0039
Baseline offset, ΔF (rel. flux)	$-0.000\,245\,5\,(77)$	$0.000\,043^{+0.000\,591}_{-0.000\,716}$	$-0.000\,041^{+0.000\,130}_{-0.000\,133}$	$-0.0107^{+0.0692}_{-0.0577}$	$-0.000\,27^{+0.006\,90}_{-0.006\,57}$
GP baseline, height scale, $\ln\sigma$	—	$-6.824^{+0.025}_{-0.026}$	$-7.184^{+0.142}_{-0.282}$	$-6.659^{+0.086}_{-0.079}$	$-6.636^{+0.177}_{-0.149}$
GP baseline, length scale, $\ln\rho$	—	$-4.952^{+0.056}_{-0.059}$	$-8.889^{+1.978}_{-2.131}$	$-0.754^{+0.129}_{-0.124}$	$0.200^{+0.178}_{-0.162}$
Host radius over semi-major axis; $R_\star/a_\mathrm{b}$	0.2834 ± 0.0014	$0.1791^{+0.0028}_{-0.0027}$	—	$0.2097^{+0.0019}_{-0.0025}$	0.1366 ± 0.0015
Planetary radius; R_b ($\mathrm{R_J}$)	1.188 ± 0.038	1.265 ± 0.017	—	1.027 ± 0.016	1.138 ± 0.024
Semi-major axis; a_b (AU)	$0.020\,68 \pm 0.000\,67$	$0.025\,58 \pm 0.000\,50$	—	$0.014\,81^{+0.000\,28}_{-0.000\,27}$	$0.029\,10^{+0.000\,70}_{-0.000\,69}$
Inclination; i_b (deg)	$84.72^{+0.29}_{-0.26}$	82.86 ± 0.24	—	$81.82^{+0.20}_{-0.16}$	84.40 ± 0.12
Eccentricity; e_b	$0.0024^{+0.0023}_{-0.0011}$	$0.000\,25^{+0.000\,18}_{-0.000\,17}$	—	$0.0499^{+0.0138}_{-0.0115}$	$0.0316^{+0.0091}_{-0.0078}$
Argument of periastron; ω_b (deg)	$266.9^{+2.0}_{-2.2}$	$181.4^{+123.2}_{-128.6}$	—	$280.8^{+5.2}_{-4.4}$	$37.2^{+285.6}_{-\ 22.2}$
Impact parameter; $b_{\mathrm{tra;b}}$	$0.325^{+0.014}_{-0.016}$	0.694 ± 0.013	—	$0.6831^{+0.0053}_{-0.0054}$	$0.7054^{+0.0079}_{-0.0081}$
Total transit duration; $T_{\mathrm{tot;b}}$ (h)	2.1835 ± 0.0024	1.903 ± 0.014	—	$1.2480^{+0.0039}_{-0.0040}$	$1.8100^{+0.0089}_{-0.0087}$
Full-transit duration; $T_{\mathrm{full;b}}$ (h)	1.7466 ± 0.0040	$1.105^{+0.023}_{-0.024}$	—	$0.6531^{+0.0070}_{-0.0069}$	$1.0083^{+0.0141}_{-0.0145}$
Epoch occultation; $T_{0;\mathrm{occ;b}}$ (d; $\mathrm{BJD_{TDB}} - 2{,}457{,}000$)	$1354.928\,554^{+0.000\,053}_{-0.000\,067}$	$1519.274\,003\,(354)$	—	$1545.638\,154^{+0.001\,381}_{-0.000\,842}$	$1412.102\,824\,(110)$
Impact parameter occultation; $b_{\mathrm{occ;b}}$	$0.324^{+0.014}_{-0.016}$	0.694 ± 0.013	—	$0.6748^{+0.0099}_{-0.0167}$	$0.7228^{+0.0081}_{-0.0083}$
Transit depth; $\delta_{\mathrm{tra;b}}$ (ppt)	10.614 ± 0.015	$18.305^{+0.145}_{-0.147}$	—	$26.625^{+0.075}_{-0.074}$	$19.586^{+0.090}_{-0.091}$
Occultation depth; $\delta_{\mathrm{occ;b}}$ (ppt)	0.346 ± 0.011	$0.180^{+0.047}_{-0.053}$	$1.473^{+0.213}_{-0.214}$	$0.153^{+0.058}_{-0.053}$	$0.199^{+0.057}_{-0.060}$
Nightside flux; $F_{\mathrm{nightside;b}}$ (ppt)	$0.039^{+0.010}_{-0.011}$	$0.028^{+0.043}_{-0.020}$	—	$0.078^{+0.068}_{-0.049}$	$0.077^{+0.072}_{-0.054}$
Equilibrium temperature b ($A_\mathrm{B} = 0.3$); $T_{\mathrm{eq;b}}$ (K)	2214 ± 17	1631^{+39}_{-38}	—	1338 ± 36	1291 ± 25
Combined host density from all orbits; $\rho_{\star;\mathrm{combined}}$ (cgs)	0.938 ± 0.014	$1.394^{+0.065}_{-0.063}$	—	$3.100^{+0.114}_{-0.081}$	$1.940^{+0.064}_{-0.061}$

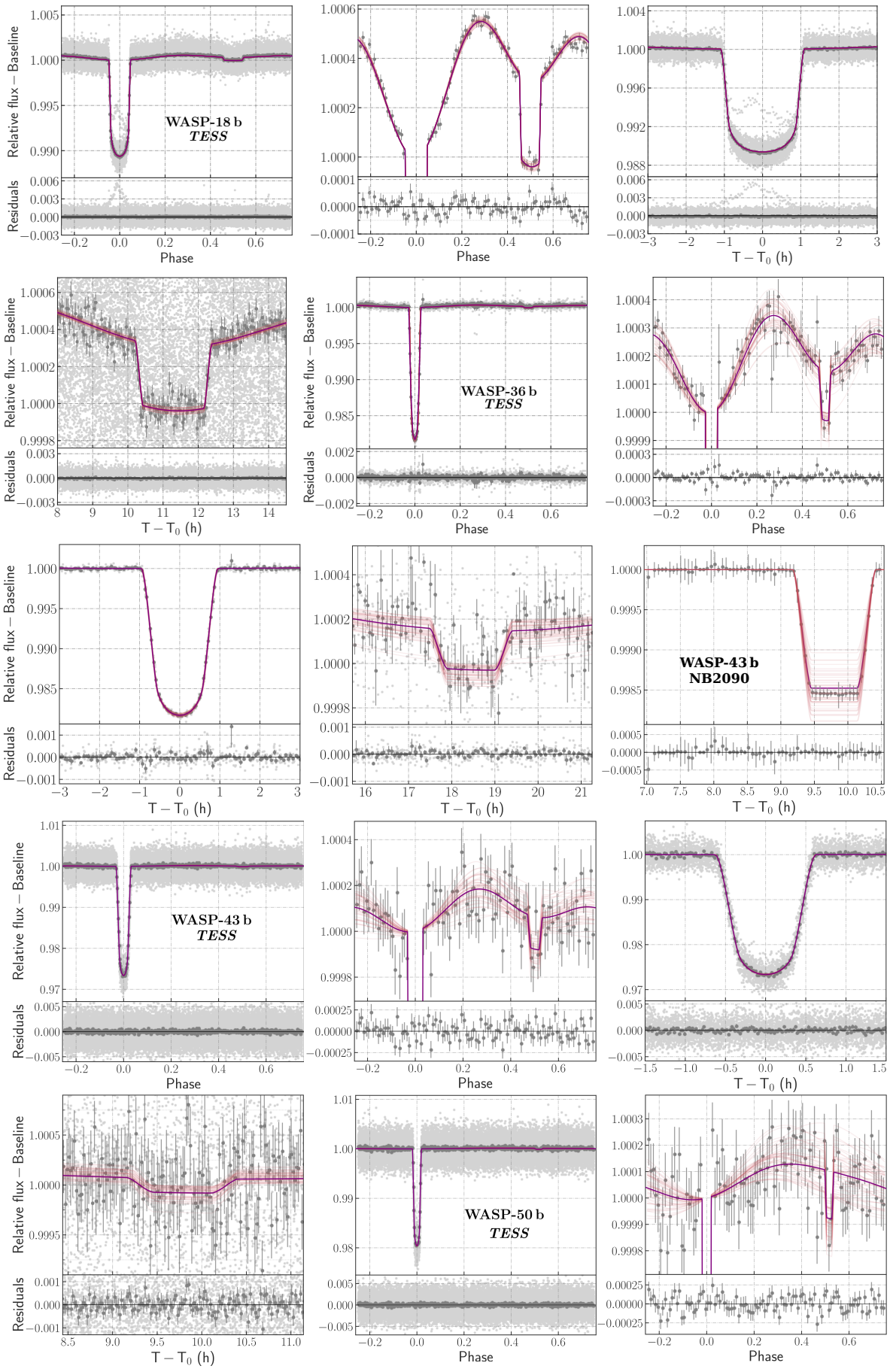
WASP-18 b
TESS
WASP-36 b
TESS
WASP-43 b
NB2090
WASP-43 b
TESS
WASP-50 b
TESS
Relative flux − Baseline
Residuals
Phase
T − T0 (h)

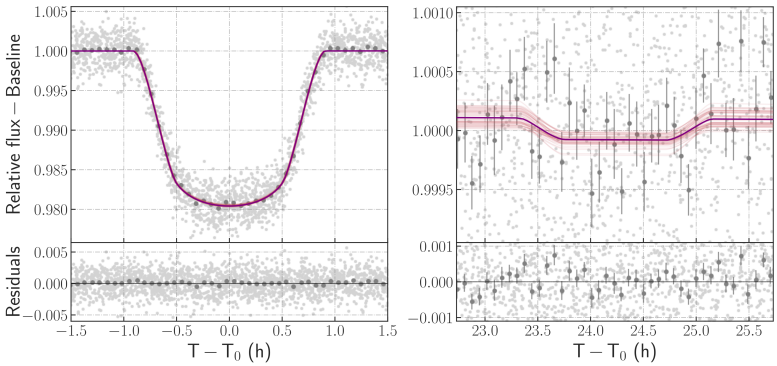

Figure 17: *From left to right and from top to bottom*: Fitted *TESS* (phased) and HAWK-I light curves of the systems analysed in this section. The *TESS* plots are shown and the meaning of the markers and the curves is as in Figure 13. For the HAWK-I plot the meaning is as in Figure 12 but without using upper limits. The forced bins of WASP-18/36/43/50 are: ≈ 2.7/4.4/2.3/5.6 min (50 points = 0.1 phase), ≈ 13.6/22.1/11.7/28.2 min (10 points = 0.1 phase), 2.5/3.5/1.2/4.3 min and 2.5/3.5/1.2/4.3 min, in the order of the listed plots.

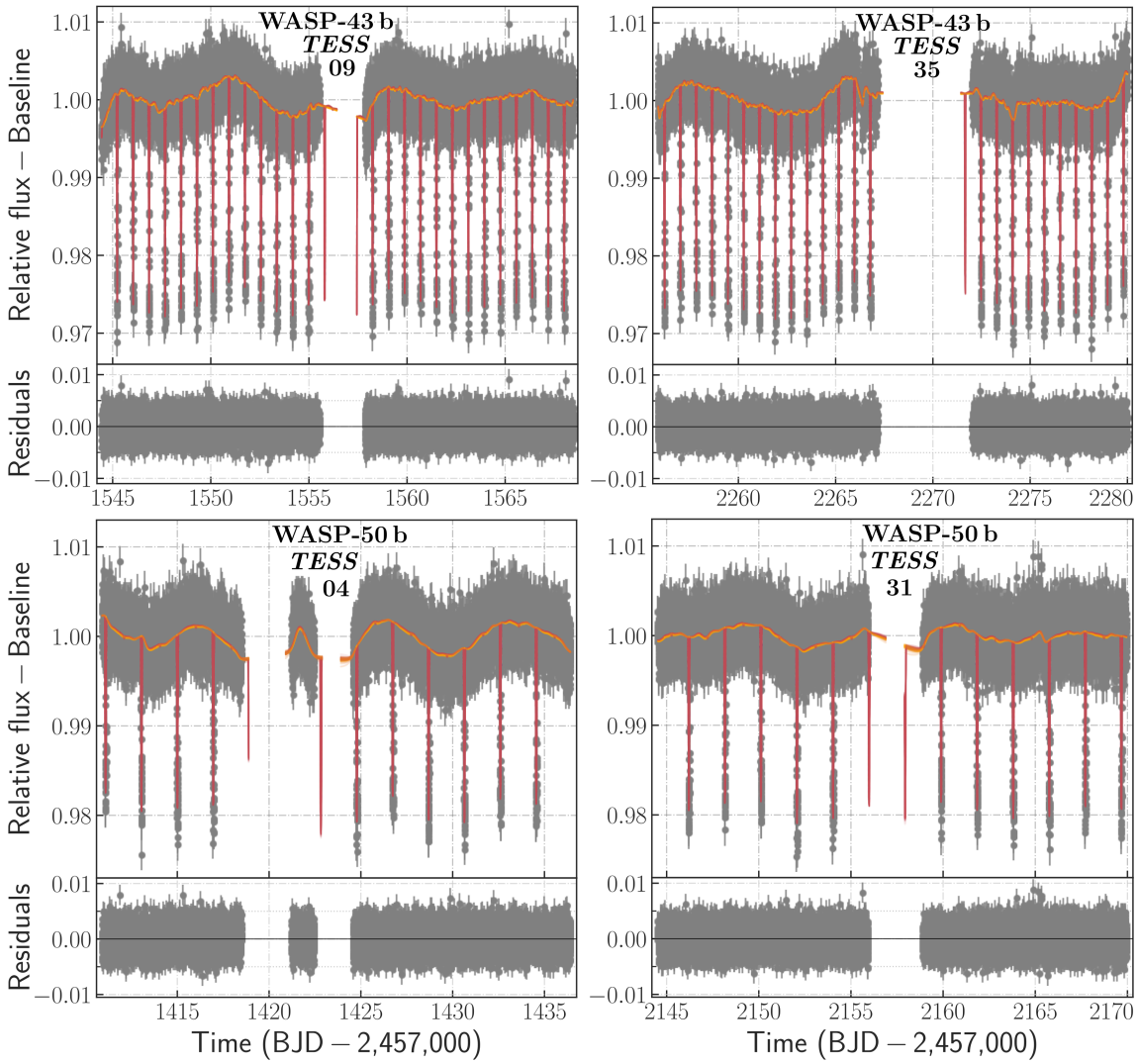

Figure 18: The original *TESS* light curves of WASP-43 and WASP-50 fitted by ALLESFITTER, shown for each sector. The stellar variability is clearly visible, seen as the orange baseline curve, whilst the red curves show transit models.

6.3. Atmospheric properties

The derived occultation depth allowed to get some estimates about the planetary atmosphere. These include measuring of reflectivity by calculating the geometric albedo, finding the brightness temperature of the dayside (and also the nightside if the nightside flux was detected) and deriving the heat redistribution factor. The atmospheric characteristics discussed in this chapter are summarised in Table 11. They were calculated using both the adopted values of the concerning quantities (R_p and a) and the herein derived values. But for clarity of the text only those using the original values are discussed. Moreover, the results obtained applying both of them agree well.

Albedo

WASP-18 b, TESS: To estimate the geometric albedo, the value of thermal contribution of 0.093 ppt was subtracted from the obtained occultation depth. The derived reflected light contribution of 0.253 ppt was then translated to the geometric albedo. This resulted in $A_g = 0.336^{+0.044}_{-0.042}$.

To obtain a more realistic constraint of the geometric albedo, the thermal contribution of 0.327 ppt derived by Arcangeli et al. (2018) from an atmospheric model as in Shporer et al. (2019) was used. If we compare this value with the inferred occultation depth of 0.346 ppt, we can see that these values are comparable and also significantly lower than the total expected depth of 1.118 ppt for $A_g = 1$. This suggests that the geometric albedo is (close to) zero. The difference between the supposed thermal emission and the inferred value of the occultation depth is only at $\approx 1.7\sigma$ significance, so a 3σ upper limit on the occultation depth due to reflected light of 0.033 ppt was placed. This implies a 3σ upper limit on the geometric albedo, $A_g^{3\sigma\mathrm{UL}} < 0.043$. This result is consistent with a 2σ upper limit of 0.048 ppt derived by Shporer et al. (2019). The ivestigation indicates negligible optical scattering as a result of absence of clouds or hazes in the planetary atmosphere. Hence, the radiation of the planet originates in strong thermal radiation.

WASP-36 b, TESS: The derived contribution of reflected light is of 0.166 ppt. This was used to infer the geometric albedo leading to $A_g = 0.296^{+0.085}_{-0.095}$. This is consistent with the constraint placed by Wong et al. (2020), who derived $A_g = 0.16^{+0.16}_{-0.15}$, and also with a 3σ upper limit of 0.286 obtained by Blažek et al. (2022). These numbers suggest that WASP-36 b is a typical hot Jupiter with a low geometric albedo and, thus, lacking the presence of reflective clouds in the atmosphere. On the other hand, the albedo is not zero as this is probable on WASP-18 b, an ultra-hot Jupiter.

WASP-43 b, HAWK-I/NB2090: The obtained reflected light of 0.692 ppt leads to a near-infrared geometric albedo, $A_g = 0.660^{+0.225}_{-0.221}$. Keating & Cowan (2017) studied the energy budget of the atmosphere of this planet. Using *HST*/WFC3 (1.1–1.7 µm) and *Spitzer*/IRAC (3.6 and 4.5 µm) data they found the near-infrared geometric albedo to be 0.24 ± 0.01. If the planetary temperature of 1483 K derived by them is applied, then the reflected light is reduced to 0.569 ppt, resulting in a consistent $A_g = 0.543 \pm 0.211$ at 2.09 µm. The same temperature was used by Blažek et al. (2022) to infer $A_g = 0.395^{+0.174}_{-0.176}$ from a lower occultation depth of the same data set. The albedo estimates obtained for this HAWK-I filter agree within 1.5σ. Moreover, they agree within less than 2σ with the *HST* and *Spitzer* data although the bandpasses are not exactly the same. The derived non-zero NIR geometric albedo suggests that the optical albedo is probably non-zero too; nevertheless, infrared observations are of thermal-emission origin which emanates from bigger depths of atmospheres than the reflected light.

WASP-43 b, TESS: The thermal emission in this bandpass is negligible. Despite that, it was subtracted from the occultation depth and the obtained reflected light contribution

is 0.168 ppt. This leads to an upper limit on the geometric albedo, $A_g^{3\sigma UL} < 0.153$. If the derived occultation depth is used and not the upper limit, we come to $A_g = 0.133^{+0.049}_{-0.053}$. The values are in agreement with $A_g^{3\sigma UL} < 0.154$ (*TESS*) of Blažek et al. (2022) and $A_g^{3\sigma UL} \lessapprox 0.06$ (*HST* WFC3/UVIS) of Fraine et al. (2021). They are also consistent with weak A_g detections of 0.31 ± 0.22 (i' band) and 0.12 ± 0.06 (*TESS* and *Spitzer* data) published by Chen et al. (2014) and Wong et al. (2020), respectively. Moreover, the results also agree with the NIR albedo suggesting that some portion of light is reflected by the planetary atmosphere. Low albedo values of hot Jupiters are generally expected since high temperatures of atmospheres do not allow gases to condensate in dense and significantly reflective clouds. Indeed, this is what is observed in most hot-Jupiter atmospheres. However, since WASP-43 b is a case of a moderate hot Jupiter ($T_{eq} \approx 1500$ K), the presence of reflective clouds or/and hazes is not unprobable and may explain the derived non-zero geometric albedo.

WASP-50 b, TESS: The contribution of reflected light is 0.197 ppt which leads to a geometric albedo, $A_g = 0.564^{+0.167}_{-0.176}$. The derived value of the albedo is high in comparison with what is observed on hot Jupiters but it is consistent with the only published albedo constraint, $A_g^{3\sigma UL} < 0.44$ (Blažek et al., 2022). Such an albedo indicates significant coverage with clouds or/and hazes and is, thus, not too probable for a hot Jupiter of about 1400 K. However, if the (relatively high) uncertainties are taken into consideration, we find the geometric albedo is also consistent with low values. To better constrain the albedo, more precise measurements are needed. Other details could be revealed by creating atmospheric models but more occultation detections in different bandpasses are required to create such models.

Temperatures

WASP-18 b, TESS: From the inferred occultation depth the brightness temperature of the atmosphere in the *TESS* band was obtained, $T_{br} = 3074^{+60}_{-66}$ K. This is significantly greater than the equilibrium temperature of 2477 K. It suggests very hot dayside of the planet, i.e. a temperature contrast between the dayside and the nightside. The temperature of the nightside can be estimated using the inferred nightside flux which is $0.039^{+0.010}_{-0.011}$ ppt. This leads to the nightside brightness temperature of $2227^{+}_{-102}{}^{76}$ K. The temperature difference of about 850 K indicates inefficient day–night heat redistribution which is not rare for close-in planetary systems. The atmosphere of this planet is further studied through the models introduced in the next section.

WASP-36 b, TESS: The calculated equilibrium temperature is $T_{eq} = 1783 \pm 45$ K whereas the derived brightness temperature for the *TESS* bandpass is $T_{br} = 2403^{+}_{-115}{}^{83}$ K. Regrettably, the derived nightside flux of $0.028^{+0.043}_{-0.020}$ ppt only provides a 3σ upper limit of 0.129 ppt which leads to a 3σ upper limit on the nightside brightness temperature of 2296 K. Since it is within 1σ of the dayside temperature, it does not help to deduce if there is an apparent temperature difference. Wong et al. (2020) derived from *TESS/Kepler/CoRoT* data in the visible bandpass $T_{br;vis} = 1500^{+}_{-1100}{}^{700}$ K. The inconsistency between their value and the value of T_{br} derived herein may come from data used for analysis—the three bands versus the *TESS* band only—although considering the high uncertainties of their result the inconsistency vanishes. They also derived, from *Spitzer* data at 3.6 and 4.5 μm, $T_{br} = 1200^{+400}_{-700}$ and 1480 ± 210 K, respectively. As seen, the brightness temperature is higher in the visible bandpass than in the infrared which is supported by the result obtained from the near-infrared data in Section 5.3. Besides thermal emission, this should be caused mainly by reflected light and implies a non-zero geometric albedo which was, in fact, derived.

WASP-43 b, HAWK-I/NB2090: The obtained equilibrium temperature is 1438^{+33}_{-30} K whilst the brightness temperature for this wavelength is $T_{\rm br} = 1655^{+59}_{-63}$ K. We can see that $T_{\rm br}$ is $\approx$ 100–200 K higher than $T_{\rm eq}$. This suggests that there could be a little temperature contrast between the dayside and the nightside of the planet which is admitted by the results of the NB1060 data and also supported by results of the study of the planetary atmosphere by Kataria et al. (2015). Moreover, they found out that the planetary flux significantly deviates from the blackbody spectrum in the near-infrared. This agrees with the work of Keating & Cowan (2017)—they even estimated that the nightside is hotter than the dayside. The equilibrium temperature of 1483 ± 10 K obtained by them as the best-fitting isothermal temperature is well consistent with that calculated here. The atmosphere of this planet is further studied through the models described in the next section.

WASP-43 b, TESS: The derived brightness temperature and its 3σ upper limit are $1971^{+\ 73}_{-107}$ K and < 2001 K, respectively. These are higher values than the equilibrium temperature of 1460 K. This confirms the assumption from NB2090 NIR data about the presence of a temperature contrast between the planetary hemispheres. Regrettably, the poor detection of the nightside flux leads to no useful constraint. The consistency with a non-zero geometric albedo, nevertheless, tells us that some amount of the incident stellar radiation may be reflected back to space and thus increasing the brightness temperature of the dayside at these wavelengths.

WASP-50 b, TESS: The calculated brightness temperature is $T_{\rm br} = 2304^{+\ 83}_{-110}$ K. This is a significantly higher value than the equilibrium temperature of 1411 K. Like in most planets studied in this thesis, this result suggests that there is a temperature contrast between the dayside and the nightside of the planet which is allowed by the results from the NB2090 data too. Further, it is supported by the relatively high geometric albedo which shows that some portion of the stellar radiation is reflected by the upper part of the atmosphere. If the planetary nightside flux was clearly detected, it could help to clarify this problem. Regrettably, the measured nightside flux implies a higher value than the occultation depth is and thus it does not help to elucidate this problem.

Heat redistribution

WASP-18 b, TESS: The equilibrium temperature estimate supposed the heat redistribution factor to be 1/4. This assumption prevents the temperature to be overestimated. Nevertheless, from the data analysed herein the heat redistribution factor was derived to be $f = 0.593^{+0.083}_{-0.087}$. This is consistent with Arcangeli et al. (2018) as this result suggests inefficient day–night heat redistribution which means that the atmosphere instantaneously reradiates the incident stellar radiation. The limiting case describing no heat redistribution around the planet of 2/3 is within 1σ significance level of the value obtained here. Morevoer, it agrees with the analysis of the planetary temperatures.

WASP-36 b, TESS: As in the case of WASP-18 b, the deduced temperature difference between the hemispheres suggests inefficient day–night redistribution of heat. Using $T_{\rm br}$ to derive the atmosphere heat redistribution factor, we come to $f = 0.835^{+0.139}_{-0.177}$ which is an unacceptably high value. Therefore, the real value of the redistribution factor can be claimed to be the greatest possible, i.e. $f \lessapprox 0.667$. The value itself corresponds to instantaneous reradiation of heat which divides the planet into two hemispheres with a significant temperature difference. Although the constraint admits all allowed values, $f \approx 2/3$ agrees with the obtained values of the equilibrium and brightness temperatures.

WASP-43 b, HAWK-I/NB2090: The brightness temperature leads to the heat redistribution factor $f = 0.438^{+0.074}_{-0.076}$ if a zero Bond albedo is supposed. This result implies that

there is partial redistribution of heat across the planetary hemispheres. Using estimates of the dayside and the nightside temperature, Keating & Cowan (2017) inferred the Bond albedo, $A_{\rm B} = 0.3 \pm 0.1$. If this albedo is used in the calculation of f instead of zero, we come to $f = 0.626^{+0.106}_{-0.109}$. This result still allows partial redistribution as well as instantaneous reradiation of heat, i.e. a negligible or apparent temperature contrast between the hemispheres. Studies affirm that the heat transport from the day- to nightside is typically efficient for planets with lower irradiation temperatures, such as e.g. WASP-43 b. This problem is elucidated by the models introduced further.

WASP-43 b, TESS: The derivation of the upper limit on the heat redistribution factor led to $f^{3\sigma{\rm UL}} < 0.882$ or $f = 0.830^{+0.148}_{-0.195}$ if the derived brightness temperature instead of its upper limit was used. Unluckily, the obtained values lie outside the possible range. Therefore, no valuable constraint can be placed, expressed as $0.25 \leqq f \lessapprox 0.667$. The values above stand for $A_{\rm B} = 0$. If we use $A_{\rm B} = 0.3$ as in Keating & Cowan (2017), then the value of the redistribution factor raises as $f \propto 1/(1 - A_{\rm B})$. Since it tends to reach higher values, $f \approx 2/3$ is a more probable value than 1/4. Nevertheless, considering the result from NB2090 data above, the real value of the redistribution factor seems to lie in between the limiting values.

WASP-50 b, TESS: The derived value of the heat redistribution factor is $1.773^{+0.308}_{-0.382}$. This is, however, far beyond a possible value. Moreover, to obtain this factor a zero Bond albedo was assumed. When $A_{\rm B} = 0.5$ is supposed (as $A_{\rm g} = 0.56$), then $f \approx 3.5$ is obtained which is even more unreasonable. Besides the Bond albedo, the factor is a function of the semi-major axis, the stellar radius, and the stellar and planetary temperatures (Equation 6). Considering that $R_\star$, $T_{{\rm eff};\star}$ and a are known with good accuracy, the most uncertain value is the planetary temperature (its fourth power). The lowest f corresponds to the equilibrium temperature whilst the highest f corresponds to the planetary temperature of 1803 K for a zero Bond albedo and 1517 K for $A_{\rm B} = 0.5$. This ambiguity may originates from the occultation depth itself which slightly indicates that it is overestimated. Therefore, it can be only claimed that $f \lessapprox 0.667$.

Table 11: The inferred occultation depths and atmospheric properties obtained from it, except for $T_{\rm eq}$, and compared with those obtained by using adopted values. These are shown for the systems analysed in this section. *Notes*: $^{(a)}$: calculated by using Equation 2; $^{(b)}$: calculated using Equation 3 assuming $f = 1/4$ and $A_{\rm B} = 0$; $^{(c)}$: calculated using Equation 4 and in $^{(d)}$ substituting $\delta_{\rm occ}$ with the nightside flux; $^{(e)}$: calculated using Equation 6 assuming $A_{\rm B} = 0$; $^{(f)}$: obtained with using expected thermal emission derived in Arcangeli et al. (2018) as in Shporer et al. (2019).

	WASP-18/*TESS*		WASP-36/*TESS*		WASP-43/NB2090
Parameter (Unit)	Adopted	This thesis	Adopted	This thesis	Adopted
Occultation depth, $\delta_{\rm occ;b}$ (ppt)	—	0.346 ± 0.011	—	$0.180^{+0.047}_{-0.053}$	$1.473^{+0.213}_{-0.214}$
Geometric albedo$^{(a)}$, $A_{\rm g;b}$	$0.320^{+0.037}_{-0.036}$	$0.336^{+0.044}_{-0.042}$	$0.288^{+0.082}_{-0.092}$	$0.296^{+0.085}_{-0.095}$	$(0.660^{+0.225}_{-0.221})$
3σ up. limit on the geom. albedo$^{(a)(f)}$	< 0.041	< 0.043	—	—	—
Equilibrium temperature$^{(b)}$, $T_{\rm eq;b}$ (K)	2504^{+63}_{-65}	2477^{+72}_{-73}	1754 ± 42	1783 ± 45	1438^{+33}_{-30}
Brightness temperature$^{(c)}$, $T_{\rm br;b}$ (K)	3072^{+60}_{-66}	3074^{+60}_{-66}	$2372^{+\ 81}_{-112}$	$2403^{+\ 83}_{-115}$	1655^{+59}_{-63}
Nightside brightness temp.$^{(d)}$ (K)	$2225^{+\ 76}_{-101}$	$2227^{+\ 76}_{-102}$	< 2267	< 2296	—
Heat redistribution factor$^{(e)}$, $f_{\rm b}$	$0.566^{+0.072}_{-0.076}$	$0.593^{+0.083}_{-0.087}$	$\lessapprox 0.667$	$\lessapprox 0.667$	$0.438^{+0.074}_{-0.076}$

	WASP-43/*TESS*		WASP-50/*TESS*	
Parameter (Unit)	Adopted	This thesis	Adopted	This thesis
Occultation depth, $\delta_{\rm occ;b}$ (ppt)	—	< 0.175	—	$0.199^{+0.057}_{-0.060}$
Geometric albedo$^{(a)}$, $A_{\rm g;b}$	$0.140^{+0.051}_{-0.056}$	$0.133^{+0.049}_{-0.053}$	$0.566^{+0.166}_{-0.176}$	$0.564^{+0.167}_{-0.176}$
3σ up. limit on the geom. albedo$^{(a)}$	< 0.160	< 0.153	—	—
Equilibrium temp.$^{(b)}$, $T_{\rm eq;b}$ (K)	1438^{+33}_{-30}	1460^{+36}_{-32}	1411 ± 33	1411^{+35}_{-34}
Brightness temperature$^{(c)}$, $T_{\rm br;b}$ (K)	$1968^{+\ 73}_{-107}$	$1971^{+\ 73}_{-107}$	$2304^{+\ 83}_{-110}$	$2304^{+\ 83}_{-110}$
3σ up. limit on the bright. temp.$^{(c)}$ (K)	< 1998	< 2001	—	—
Heat redistribution factor$^{(e)}$, $f_{\rm b}$	$\lessapprox 0.667$	$\lessapprox 0.667$	$\lessapprox 0.667$	$\lessapprox 0.667$

Conclusions

WASP-18 b, TESS: The analysis led to a clear detection of the occultation of the planet. From the obtained depth an upper limit on the geometric albedo was derived showing that it is consistent with a zero value. This outcome suggests that the radiation emanating from the planet is in the from of thermal radiation with no light reflected by the atmosphere. The brightness temperatures revealed that there is a temperature contrast between the the dayside and the nightside. This is supported by the obtained heat distribution factor implying absolute (or nearly) instantaneous reradiation of heat between the hemispheres.

WASP-36 b, TESS: The occultation has been detected with sufficient significance when the data were binned. The derived geometric albedo is of a low value although in this case the albedo is not consistent with a zero value. The obtained equilibrium and brightness temperatures show that the dayside is hotter than the nightside. The obtained heat redistribution factor allows the maximum possible value, i.e. instantaneous reradiation of heat, which is in agreement with the derived temperatures.

WASP-43 b, HAWK-I/NB2090: The occultation has been successfully detected. From the depth a non-zero near-infrared geometric albedo was derived. This indicates that neither the optical albedo is consistent with zero, but it is more probable that the planetary infrared radiation is solely in the form of thermal emission. The inferred temperatures suggest that a temperature contrast between the hemispheres may exist. However, the derived heat redistribution factor does not lead to a clear conclusion since it allows both no and partial redistribution of heat.

WASP-43 b, TESS: Although the occultation has not been clearly detected, the placed upper limit led to a valuable constraint on the geometric albedo. The results show that the albedo need not be necessarily equal to zero. Like the previous planets, the obtained equilibrium and brightness temperatures indicate that there is a temperature contrast between the planetary hemispheres. It is also suggested by the heat reditribution factor albeit not convincingly. Further, stellar variation of the parent star was investigated. Even though the fits did not lead to an explicit outcome about the modulation period and the amplitude, they admit the results found in literature.

WASP-50 b, TESS: A successful detection of the occultation has been reached. From that, the geometric albedo, the brightness temperature and consequently the heat redistribution factor were derived. Although the albedo and the brightness temperature are of physically reasonable values, they are unexpectedly high with the redistribution factor beyond the acceptable value. It is obvious that the problem originates in the high value of the derived occultation depth which indicates to be overestimated. The found occultation depth can be in fact a result of the scattered data which fit the time of the occultation. Furthermore, other fits were performed on binned data—they allowed to place 3σ upper limits, a few hundredths ppt lower than the detected depth. This suggests that the occultation is shallower in real. The analysis of this data set also included investigation of the stellar variability of the parent star. Nevertheless, it did not result in convincing results.

6.4. Noise analysis

The time-uncorrelated white and time-correlated red noise were analysed from the obtained light curves. To see which type of noise prevails in each data set, plots of RMS of the binned residuals as the function of bin widths were constructed. Pure white-noise contribution was calculated as $1/\sqrt{bin\ width}$ implying increasing SNR with an increasing bin width. The plots are displayed in Figure 19.

There is an obvious distinction of the contribution of the red noise between the *TESS* and most of the ground-based data. The red noise contribution is weak in the *TESS* data which can be seen in the plots where the solid curve (roughly) follows the dotted line. On the other hand, HAWK-I data exhibit strong presence of the red noise. This is recognisable as the solid curve barely drops with the increasing bin width. Another case is OGLE-9. Here, the solid curve declines more steeply than the dotted line. These plots show white-noise limited data, even those obtained with a ground-based facility. This results from the fact that OGLE-9 is a faint star of 125× lower brightness than of WASP-18, the brightest star of the studied systems.

The main source of the red noise is seeing. The data revealed that the crucial effect on the resulting flux is the seeing variability rather than the seeing value itself. For the studied data obtained by Fast Photometry Mode of HAWK-I there is another contributor increasing RMS of the data. Since the exposure times are often short, the observed stars usually occupy a small area on the detector due to a low number of caught photons. This consequently leads to great differences in the measured absolute flux of the individual images. To decrease the RMS, defocusing of the observed stars to spread them over more pixels on the detector could be an appropriate solution besides extending the integration time.

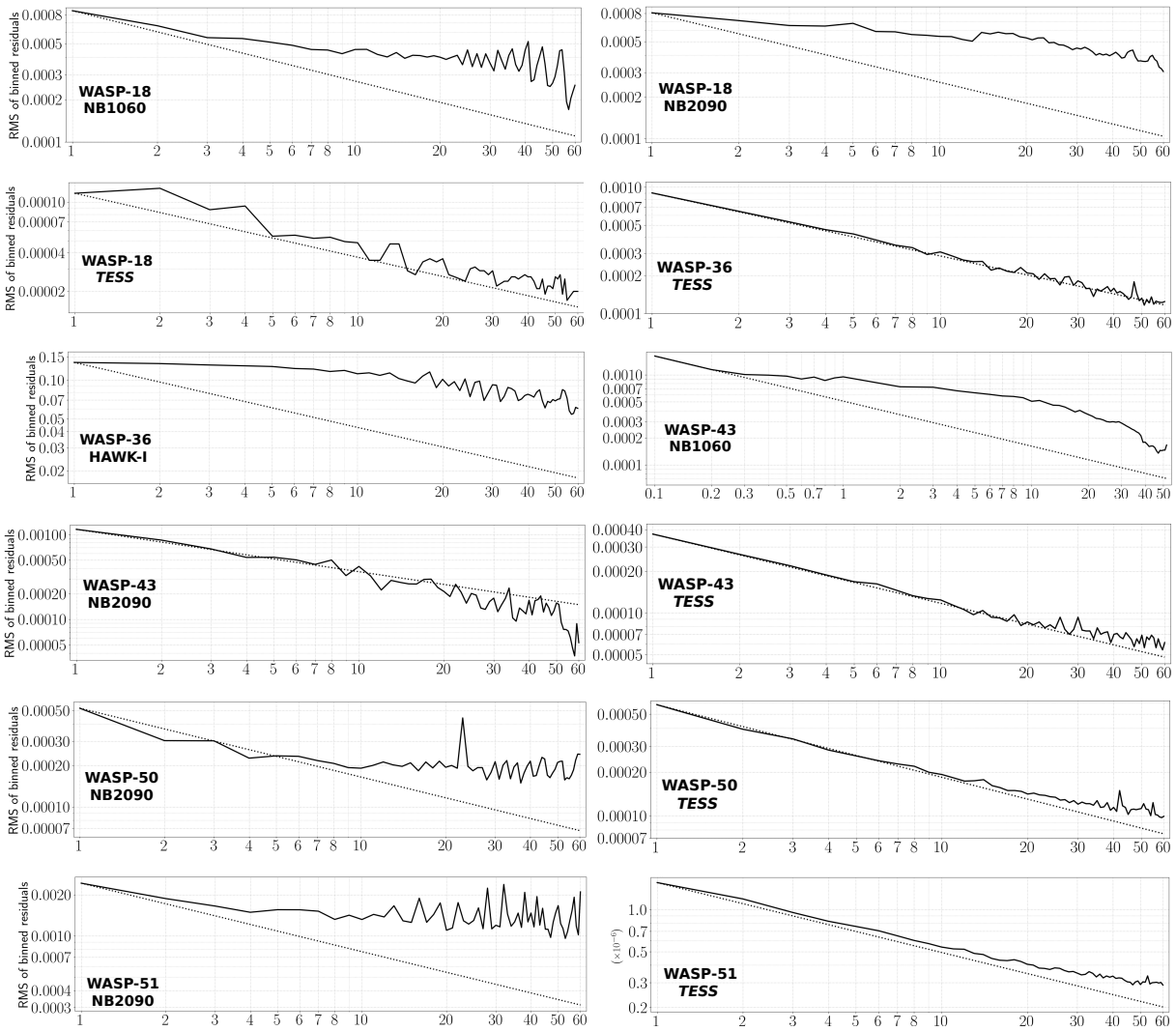

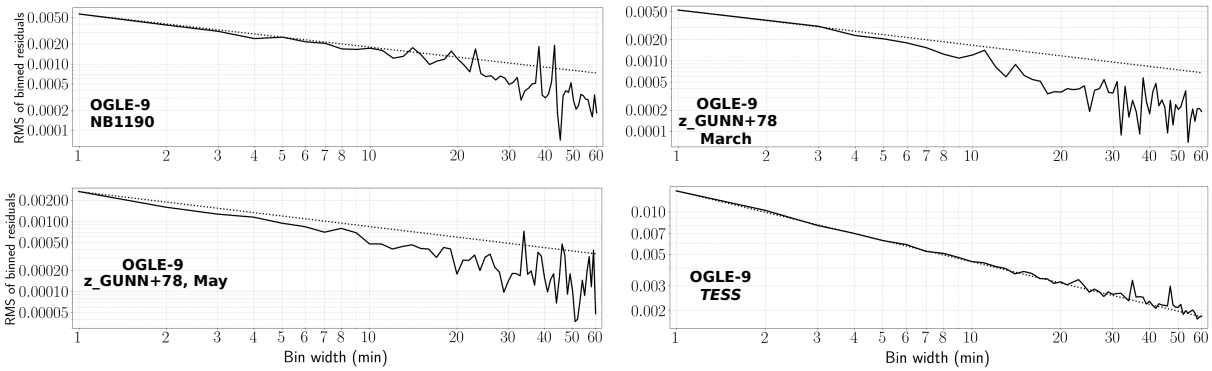

Figure 19: The effect of red noise contained in the data for each of the analysed data sets—the solid curve. The dotted line shows the RMS of the unbinned data, representing expected noise if only white was present.

6.5. Summary of the obtained results

In the previous sections, analyses of six exoplanetary systems covering sixteen data sets were performed. The goal was to detect occultations (secondary eclipses) in the data so that atmospheric characteristics such as albedo, temperatures, or heat distribution could be estimated. For most of the processed data upper limits on the occultation depths and quantites derived from them have been placed since the occultations could not be clearly detected. Apart from these, the equilibrium temperature ($T_{\rm eq}$) was inferred for each of the planets as it is independent of the occultation measurement. The knowledge of studied planets, and thereby their atmospheres, is strongly dependent on our knowledge of their host stars. Note that all stellar properties used in the analyses are adopted. The following paragraphs briefly summarise the obtained results.

Planet WASP-18 b was studied in three different bandpasses of two facilities. The ground based data of HAWK-I instrument of VLT revealed a high level of noise in both the NB1060 and the NB2090 data. This allowed only to put upper limits on the occultation depths ($\delta_{\rm occ}$), the brightness temperature ($T_{\rm br}$) and upper/lower limits on the heat redistribution factor (f). Unluckily, the derived $\delta_{\rm occ}$ in NB2090 filter seems to be underestimated and, thus, being a false positive in the way that the flux drop due to the occultation event is hidden in the noisy data. The space-based *TESS* data, on the other hand, resulted in a clear occultation detection and hence the other quantities relating to the composition of the planetary atmosphere. It is studied in more detail in Section 7 where a self-consistent model of the planetary atmosphere is introduced. In short, the model shows that heat distribution is very inefficient and that the planetary radiation is purely of thermal-emission origin.

The next investigated planet is WASP-36 b where the HAWK-I/NB2090 data led to placing reasonable (3σ) upper limits on $\delta_{\rm occ}$, $T_{\rm br}$ and f. The analysis of the *TESS* data resulted in a clear detection of the occultation if the data set was binned prior to modelling. This is the first occultation detection in the visible bandpass as well as the first valuable constraint on the geometric albedo. Moreover, the detected occultation depth of the binned data is well consistent with the upper limit obtained from the analysis of the unbinned data.

The first data set investigating planet WASP-43 b is HAWK-I/NB1060. The observational run did not cover the whole occultation event but 3σ upper limits could be placed albeit with a weak constraint. In contrast to these data, the outcome of HAWK-I/NB2090

data set is a clear detection of the occultation. It made possible to obtain good-precision values of $T_{\rm br}$, f and $A_{\rm g}$ but considering the geometric albedo is not relevant for the infrared bandpass. The *TESS* data led to placing valuable constraints on $\delta_{\rm occ}$, $A_{\rm g}$ and $T_{\rm br}$. Further, stellar variability was investigated. Although no unambiguous results were obtained, under certain conditions they match the already known stellar-variability model. The introduced model in Section 7 shows that the radiation of the planet is of thermal-emission origin and that there is 10-% redistribution of heat from the dayside to the nightside of the planet.

The investigation of planet WASP-50 b using the HAWK-I/NB2090 data led to placing a (3σ) upper limit on $\delta_{\rm occ}$, $T_{\rm br}$ and f since the occultation was not clearly detected. In the case of *TESS* data, sufficient significance of the occultation detection was reached. This is the first detection of the occultation of this planet. From that, $A_{\rm g}$ and $T_{\rm br}$ were derived together with an upper limit on f. Nevertheless, by taking into account the derived atmospheric characteristics, the occultation depth itself and the level of noise, the obtained depth of the occultation suggests not to be real. Stellar variability of the host star was also investigated. Although the already published stellar rotational period is probable when compared with the results obtained herein, their ambiguity does not lead to a clear conclusion about the properties of the stellar modulation.

Planet WASP-51 b (HAT-P-30 b) was at first studied using the HAWK-I/NB2090 data. The analysis resulted in placing a 3σ upper limit on $\delta_{\rm occ}$ and $T_{\rm br}$. For this bandpass, these are the first estimates of characteristics of the planetary atmosphere. Likewise, the *TESS* data led to placing a 3σ upper limit on $\delta_{\rm occ}$, $A_{\rm g}$ and $T_{\rm br}$. The results are very well consistent with the only study of the occultation of this planet. The measured eccentricity (e) of the planetary orbit revealed that $e \neq 0$. This implies, however, that the HAWK-I data do not involve the occultation event and thus the obtained results do not reflect the change of flux due to the occultation. It is not possible to re-fit the HAWK-I light curve with the derived e—shifting the time of the centre of the occultation from phase of 0.5 to ≈ 0.4 would mean to shift it 6–7 hours prior to the original occultation time. Yet, the baseline between the first data point and the beginning of the occultation spans only ≈ 2 hours.

The last studied planet was OGLE2-TR-L9 b. The HAWK-I data obtained using NB1190 filter led to deriving a 3σ upper limit on $\delta_{\rm occ}$ and $T_{\rm br}$. Further, the planet was investigated by analysing two data sets acquired by FORS2 instrument through z_GUNN+78 filter. As the result a 3σ upper limit on $\delta_{\rm occ}$ and $T_{\rm br}$ were placed. Finally, the *TESS* data were analysed and from the obtained results a 3σ upper limit on $\delta_{\rm occ}$ and $T_{\rm br}$ were placed. These studies are the first ones aimed to investigate occultations and atmospheric properties of this planet.

The derived characteristics of the atmospheres of all the six planets for all particular data sets/instruments/filters are summarised in Table 12.

For all the studied planets the geometric albedo or its upper limit were derived. Since the derived occultation depth/upper limit of each planet is lower than its expected reflected light component, this leads to an unsurprising conclusion that the geometric albedo of the planets is lower than one. An exception is OGLE-9 b where the albedo reached an unacceptably high value and its occultation depth and the upper limit exceeded the value of reflected light for $A_{\rm g} = 1$. This very hot Jupiter has probably very strong thermal radiation which deviates from radiation of a blackbody. The effective temperature of the host star is 6933 K and hence, according to the Wien's displacement law, the peak intensity is around 400 nm, i.e. in the blue part of the visible band. This could explain the great occultation depth in the *TESS* bandpass whilst suggesting a very low albedo since

Table 12: The derived values and upper limits of all the planets from data sets analysed in sections 5 and 6 of this thesis. These are following: occultation depth, 3σ upper limit on the occultation depth, geometric albedo (or 3σ upper limit), brightness temperature (or 3σ upper limit) and heat redistribution factor (or $[3\sigma]$ upper limit), respectively in the order of the given columns. For each of the planets, the equilibrium temperature is also given.

Data set: **Planet** Filter	$\delta_{\rm occ}^{\rm der}$ (ppt)	$\delta_{\rm occ}^{3\sigma{\rm UL}}$ (ppt)	$A_{\rm g}^{(3\sigma{\rm UL})}$ (ppt)	$T_{\rm br}^{(3\sigma{\rm UL})}$ (K)	$f^{([3\sigma]{\rm UL})}$
WASP-18 b:			$T_{\rm eq} = 2477^{+72}_{-73}$ K		
NB1060	$0.463^{+0.278}_{-0.284}$	< 0.853	(< 0.714)	< 3150	< 0.626
NB2090	$0.490^{+0.270}_{-0.280}$	< 0.825	(0)	< 2291	≈ 0.250
TESS	0.346 ± 0.011	—	< 0.043	3074^{+60}_{-66}	$0.593^{+0.083}_{-0.087}$
WASP-36 b:			$T_{\rm eq} = 1783 \pm 45$ K		
NB2090	0.860 ± 0.620	< 1.860	—	< 2176	< 0.592
TESS	$0.180^{+0.047}_{-0.053}$	—	$0.296^{+0.085}_{-0.095}$	$2403^{+\ 83}_{-115}$	$\lessapprox 0.667$
WASP-43 b:			$T_{\rm eq} = 1460^{+36}_{-32}$ K		
NB1060	$1.190^{+0.930}_{-0.830}$	< 2.790	—	< 2621	$\lessapprox 0.667$
NB2090	$1.473^{+0.213}_{-0.214}$	—	$\left(0.660^{+0.225}_{-0.221}\right)$	1655^{+59}_{-63}	$0.438^{+0.074}_{-0.076}$
TESS	$0.153^{+0.058}_{-0.053}$	< 0.175	< 0.153	< 2001	$\lessapprox 0.667$
WASP-50 b:			$T_{\rm eq} = 1411^{+35}_{-34}$ K		
NB2090	$1.072^{+0.590}_{-0.700}$	< 2.100	—	< 2165	$\lessapprox 0.667$
TESS	$0.199^{+0.057}_{-0.060}$	—	$0.564^{+0.167}_{-0.176}$	$2304^{+\ 83}_{-110}$	$\lessapprox 0.667$
WASP-51 b:			$T_{\rm eq} = 1743 \pm 41$ K		
NB2090	$0.589^{+0.426}_{-0.397}$	< 1.278	—	< 2309	$\lessapprox 0.667$
TESS	$0.047^{+0.036}_{-0.029}$	< 0.109	< 0.367	< 2423	$\lessapprox 0.667$
OGLE-9 b:			$T_{\rm eq} = 2014^{+101}_{-100}$ K		
NB1190	$0.264^{+0.394}_{-0.188}$	< 1.183	—	< 3102	$\lessapprox 0.667$
z_GUNN+78	$0.225^{+0.347}_{-0.166}$	< 1.040	—	< 3326	$\lessapprox 0.667$
TESS	$1.153^{+0.527}_{-0.501}$	< 1.582	—	< 3736	$\lessapprox 0.667$

the high planetary temperature does not support existence of reflective clouds, similarly as for WASP-18 b.

The left plot of Figure 20 shows the obtained geometric albedos of the investigated planets as a function of their equilibrium temperature. In addition, several data points of the same and also other planets taken from literature are included to see consistency between the derived and adopted albedos for the given hot-Jupiter sub-categories. Note that the $A_{\rm g}$ value of WASP-18 b of this thesis is obtained using the calculated thermal emission whereas the upper limit is based on the adopted thermal emission from Arcangeli et al. (2018) as in Shporer et al. (2019). The depicted albedos lie below 0.4 with the exception of WASP-50 b where the obtained results are ambiguous. The fact that not all the geometric albedos of hot Jupiters (not only here) are very low reveals that there is a variety of hot-Jupiter atmospheres which originates in ongoing processes in the atmospheres as well as in the types of present clouds. For the same targets, the right plot of the figure shows the geometric albedo as a function of the ratio of the orbital semi-major

axis to the planetary radius. The ratio is an identifier whether an exoplanet matches the characteristics of a hot-Jupiter-type planet. The lower the ratio, the bigger the planet or/and the greater proximity of the planet to its host star. We can see that hot Jupiters are found in a a/R_p region of an order of tens. This is what we do not know from the Solar System. As an example, this ratio is ≈ 23,700, ≈ 23,500 and 10,900 for Mercury, Earth and Jupiter, respectively. Furthermore, a mirror-like pattern of the two plots for most of the presented planets is obvious. The explanation is straightforward—the closer the planet is to its host star, the higher its temperature is.

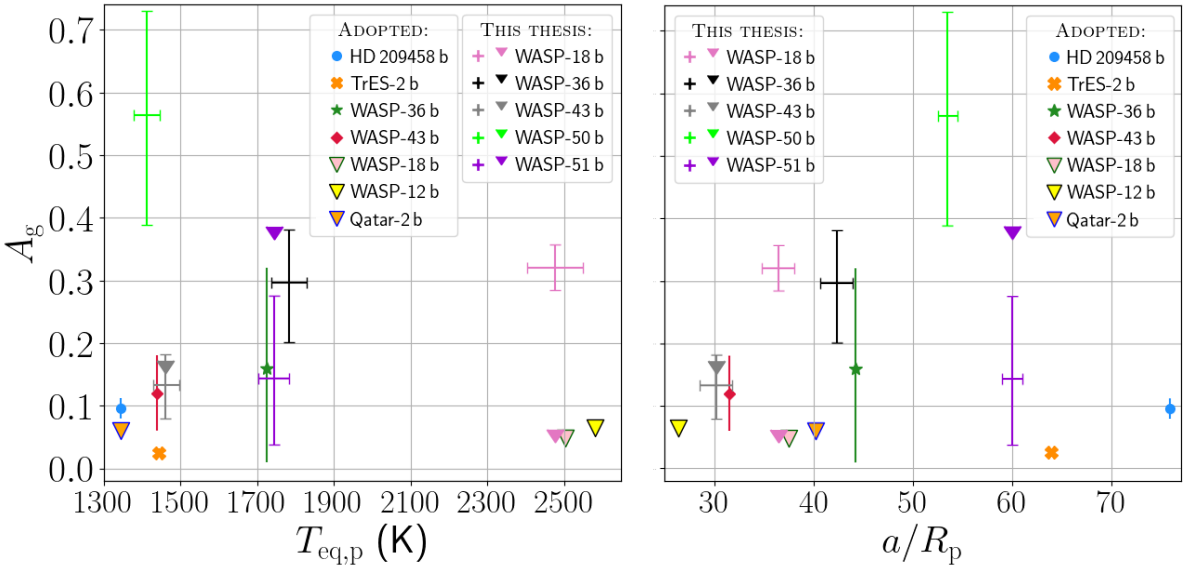

Figure 20: Geometric albedo for the visible *TESS* band as a function of the equilibrium temperature (*left plot*) and the ratio of the semi-major axis to the planetary radius (*right plot*) for the studied planets except OGLE-9 b, all obtained in this thesis. Albedo constraints adopted from literature are also included in the plots. The downward triangles show upper limits—the smaller ones are herein obtained constraints whilst the bigger ones with different-colour contours are adopted albedo constraints. The crosses show the derived values including uncertainties depicted with error-bar caps whilst other symbols with only y error bars without error-bar caps show adopted values. Instruments and corresponding literature references: HD 209458 b: *CHEOPS*, Brandeker et al. (2022); TrES-2 b: *Kepler*, Kipping & Spiegel (2011); WASP-36 b+WASP-43 b: *TESS*, Wong et al. (2020); WASP-18 b: *TESS*, Shporer et al. (2019); WASP-12 b: *HST*/STIS, Bell et al. (2017); Qatar-2 b: *K2/Kepler* Dai et al. (2017).

Observations of occultations are very demanding since the flux drop caused by hiding a planet behind its host star is generally very small, even when compared to the flux drop caused by a planet covering a part of the stellar disc, i.e. during transits. In most cases of the systems investigated in this thesis, the analysis did not lead to a clear detection of the occultation and upper limits were placed for these planets. There are more effects which contributed to this outcome, mainly time-correlated (red) noise and time-uncorrelated (white) noise.

The analysis of all the data sets showed that OGLE-9 data are the only white-noise limited. Indeed, the apparent magnitude of the star is about 14 mag (*TESS*). The low brightness of the star produces, thus, more photon noise than the time-correllated noise.

The ground-based data were acquired by observing through near-infrared filters. Although they were performed with 8-m telescopes, the presence of red noise resulted in data in which occultations could not be detected. Moreover, the contribution of red noise increases with wavelength, therefore the infrared data suffer from its presence. As found, the variability of seeing during the observations was the main contributor causing large data scatter and leading thus to the occultation non-detections. Except two data sets, all observations with HAWK-I instrument were performed using Fast Photometry Mode. The short exposure times, typical for this mode, led to small aperture radii resulting in a low value of the absolute flux. This led to a low value of the signal-to-noise ratio and thus more decreased the probability of a detection of the occultation.

The space-based *TESS* data, on the other hand, produces a very low level of red noise as measurements are not affected by the presence and processes in the atmosphere of the Earth. Nevertheless, there are small telescopes of a 10-cm diameter onboard the spacecraft and hence an occultation detection is at the border of the possibilities of the instrument. This is because in the visible band, where *TESS* observes, there is usually very low thermal emission which hot Jupiters typically produce. But if an ultra-hot Jupiter is measured, it can produce strong thermal emission even in the visible band. This is the case of WASP-18 b and possibly OGLE-9 b, studied in this thesis.

7. Models of planetary atmospheres

In this section, models of emission spectra and temperature profiles are introduced. These were created for planets WASP-18 b and WASP-43 b. Since the former has an equilibrium temperature of ≈ 2500 K and the latter ≈ 1450 K, they are found at opposite temperature ends of the hot-Jupiter group of exoplanets. Hence, they are ideal cases for comparing these two regimes of hot Jupiters.

In the previous sections, occultation depths and geometric albedos were derived from *TESS* and HAWK-I data for the above-mentioned planets. Consequently, they allow to place constraints on the scattering and thermal emission in the visible and especially in the near-infrared band which lead to an assessment of the atmospheric properties of these planets.

The dayside of the atmospheres were self-consistently modelled using GENESIS atmospheric model (Gandhi & Madhusudhan, 2017). It solves for thermal emission spectrum, chemical profile of the atmosphere and the temperature profile. This is reached by line-by-line calculating full radiative transfer under radiative-convective, hydrostatic, thermodynamic and thermochemical equilibrium. To calculate equilibrium chemical abundances, HSC CHEMISTRY software (e.g. Moriarty et al., 2014) applying GIBBS solver (White et al., 1958) was used. The calculations of the equilibrium chemistry consider more than 150 chemical species. Since hot-Jupiter atmospheres were modelled, chemical species which dominate H_2-rich atmospheres of this type planets causing atmospheric opacity (e.g. Burrows & Sharp, 1999) were considered. These are H_2, H^-, He, H_2O, HCN, NH_3, C_2H_2, CH_4, CO, CO_2, TiO, VO, Na and K. Since *TESS* data, sensitive only to the visible flux, do not resolve spectral features due to individual chemical species, only TiO, VO, Na and K were used in the models as the source of atmospheric opacity in this bandpass.

The absorption cross sections were caluclated as in Gandhi & Madhusudhan (2017). For this, line lists from HITEMP and HITRAN (Rothman et al., 2010), and ExoMol (Tennyson et al., 2016) were used. The free prameters in the modelling were the incident irradiation, the internal flux and the elemental abundances. These were explored by changing metallicity and C/O ratio. The dayside incident irradiation was inspected by changing energy distribution efficiencies—on the dayside and between the nightside and the dayside. Since both the studied planets are highly irradiated, the internal flux parametrised by temperature was set to 100 K as the internal flux is not assumed to affect the atmospheres of these planets. The atmospheric models were explored not only to explain the HAWK-I and *TESS* occultation depths obtained in this thesis but also *HST* and *Spitzer* already published occultation depths.

The irradiation temperature of the planets was estimated assuming $A_B = 0$ and no dayside–nightside energy redistribution as

$$T_{\mathrm{irr}} = 2^{-\frac{1}{4}} \left(\frac{R_\star}{a} \right)^{\frac{1}{2}} T_{\mathrm{eff};\star}. \tag{10}$$

7.1. WASP-18 b

The atmospheric model of WASP-18 b (Figure 21) is able to explain the *TESS* and *Spitzer* data under conditions where there is no day–night energy distribution and no energy redistribution on the dayside either, and solar metallicity and C/O = 1 (carbon-to-oxygen ratio) is assumed. The model with no day–night and no dayside redistribution corresponds to a heat redistribution factor of 2/3. This is consistent with *Spitzer* observations (Maxted et al., 2013) and with the results obtained for this planet herein, except for

HAWK-I/NB2090 data—the occultation depth and hence the redistribution factor were found to be underestimated. From *HST*/WFC3 observations, Arcangeli et al. (2019) derived $0.55 < f < 0.63$ implying instantaneous reradiation rather than uniform redistribution of heat. The obtained model is able to fit the derived *TESS* and the adopted *Spitzer* results within $\approx 2\sigma$.

The model of WASP-18 b atmosphere is broadly consistent with earlier works analysing *Spitzer* and *HST*/WFC3 data and studying thermal emission of the planet. Since C/O ratio has been found to significantly influence exoplanetary atmospheres (Madhusudhan, 2012), it was an important free parameter for the atmospheric model. The best match of the model with measurements was reached with C/O = 1 retrieved by Sheppard et al. (2017) from *HST*/WFC3 thermal emission observations. Whilst a higher C/O ratio better fitted the lack of water absorption in WFC3, the *TESS* and *Spitzer* observations were not considerably sensitive to changing of this ratio. To explain the *Spitzer* observations, thermal inversion is needed to be involved which is in agreement with e.g. Sheppard et al. (2017) or Arcangeli et al. (2018). In contrast to *Spitzer* IRAC1, the IRAC2 measurement implies a higher brightness temperature as this wavelength probes a CO emission feature. In addition, since the *TESS* occultation depth fits well the thermal emission model, there is no need for reflected light. This is in accordance with the low upper limit on the geometric albedo (< 0.04) derived from the *TESS* data. The model is also consistent with the near-infrared HAWK-I/NB1090 upper limit on the occultation depth. However, the upper limit obtained from HAWK-I/NB2090 is strongly outlying. This dispcrepancy has been already discussed in sub-chapter 5.2. All that has to be pointed out here is that it is not a matter of a mismatched model—it is a result of low-quality data instead.

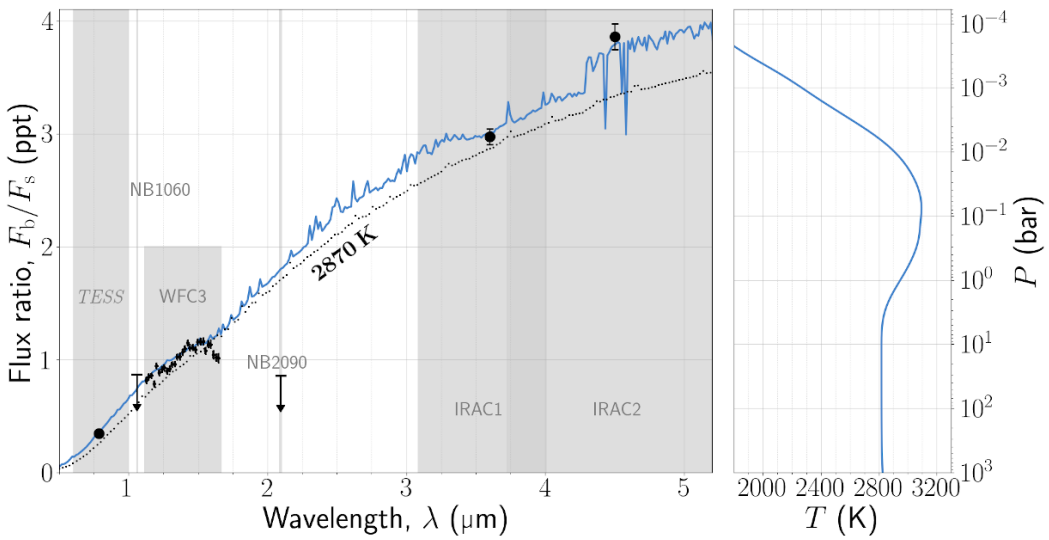

Figure 21: Self-consistent model of thermal emission and pressure-temperature profile of WASP-18 b atmosphere of the dayside (the blue curves). The black points with the error bars show *TESS* (the error bars are within the size of the marker), *Spitzer* IRAC1 and IRAC2, and *HST*/WFC3 measurements (both Sheppard et al., 2017) whilst the black arrows show 3σ upper limits obtained from the HAWK-I observations. The black dotted line represents a blackbody spectrum corresponding to an irradiation temperature of 2870 K. Particularly, for the planet blackbody radiation was supposed whereas for the star a model of the stellar spectrum of Castelli & Kurucz (2003) was used. The model was computed without considering the HAWK-I data points (NB2090 comes from a false occultation detection).

7.2. WASP-43 b

The model of the atmosphere of much cooler WASP-43 b, when compared to WASP-18 b, is shown in Figure 22. The *TESS*, HAWK-I and *Spitzer* data are able to be fitted by the presented model under following assumptions: solar metallicity, C/O = 0.5, energy redistribution on the dayside is efficient, and 10 % of the dayside energy is distributed to the nightside. The heat-energy distribution corresponds to a heat redistribution factor of $f = 0.45$, a case between uniform redistribution and instantaneous reradiation. The value is in very good agreement with the HAWK-I/NB2090 measurement and with earlier results of day–night redistribution of energy found to be inefficient (Gillon et al. 2012, Blecic et al. 2014; TRAPPIST and *Spitzer*, respectively). Although the significant flux contrast between the dayside and the nightside suggests inefficient heat redistribution between the two hemispheres, Stevenson et al. (2017) noted that it can caused by high-altitude clouds on the nightside. The derived model with the low-efficient day–night energy redistribution is consistent with the *Spitzer* and HAWK-I/NB2090 occultation depths within $\approx 1\sigma$.

In contrast to WASP-18 b, the atmosphere of WASP-43 b is dominated by water and carbon monoxide absorption. The absorption features of H_2O and CO are probed by IRAC1 and IRAC2 *Spitzer* channels, respectively. The *TESS* and HAWK-I/NB2090 bands complement the model by probing the continuum and imply, thus, a higher brightness temperature than in the case of the *Spitzer* data. Further, the model fits well the occultation depth obtained from *HST*/WFC3 as in Kreidberg et al. (2014). Note that to explain the *TESS* upper limit, no reflected light component is needed and hence the upper limit is consistent with pure thermal emission, likewise the model of WASP-18 b.

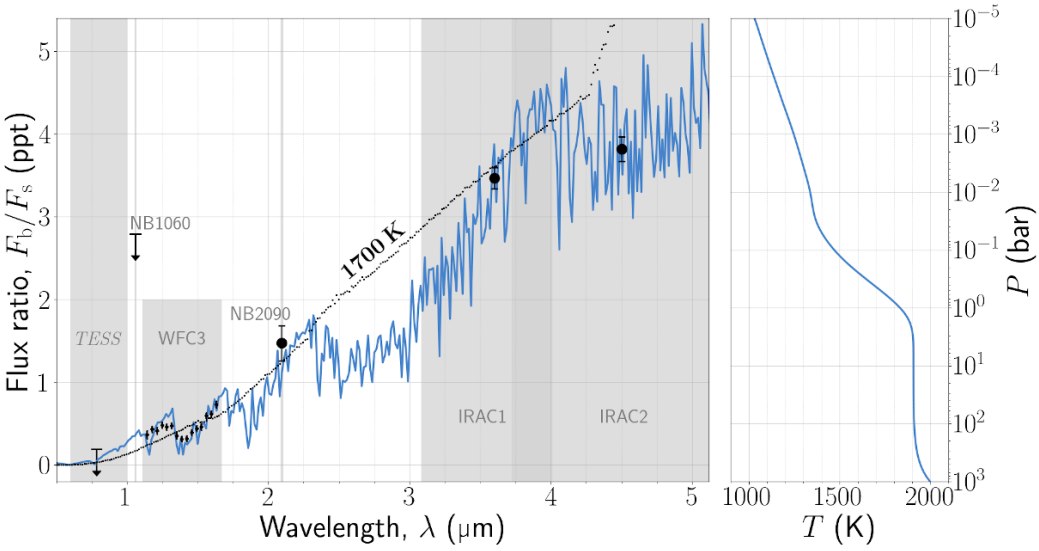

Figure 22: Self-consistent model of thermal emission and pressure-temperature profile of WASP-43 b atmosphere of the dayside. The meaning of the curves and symbols is the same as in Figure 21. The *HST*/WFC3 and *Spitzer*/IRAC1+IRAC2 data are from Kreidberg et al. (2014) and Blecic et al. (2014), respectively. The blackbody spectrum was obtained the same way as in the previous figure but corresponding to an irradiation temperature of 1700 K. The model also fits the HAWK-I/NB1060 upper limit although it was not considered in the computation.

The introduced models together with their description were originally created by Anjali A. A. Piette (Carnegie Postdoctoral Fellow at the Earth & Planets Laboratory, Carnegie Institution for Science, Washington, DC, USA) for article Blažek et al. (2022) where more details concerning the models can be found.

8. Conclusion

This thesis dealt with characterisation of hot-Jupiter type of exoplanets. These planets are relatively easy to study since their presence as well as imprints of their atmospheres are very noticable when compared to small and/or cold planets.

To characterise the six selected hot Jupiters, photometric data and method were used, with one exception involving also data obtained using spectroscopy. Besides the planet characterisation itself, the analysed ground-based and space-based data sets also served as a comparison tool for these two types of observatories. Moreover, the studied planets cover a large range of types of hot Jupiters—from 'normally' hot to ultra-hot ones.

The ground-based data involved light curves obtained by HAWK-I and FORS2 instruments mounted on VLTs of ESO and working in the near-infrared band. Such observations are suitable for investigation of planetary thermal emission which is best pronounced at the (near-) infrared band of the electromagnetic spectrum. On the other hand, observations in the visible band provide information about planetary albedo, i.e. a measure of reflectivity. This was studied using data obtained by the *TESS* mission. Observations at these two wavelength ranges are complementary and help us to describe the planetary atmospheres—their chemical composition, physical processes etc.

The planets in the thesis were investigated by measuring their occultation depth. Such a flux drop is usually very small (even for hot Jupiters) and precise measurements are needed. In the sixteen analysed data sets four occultations were detected with at least 3σ significance. Using the ground-based observations, this is WASP-43 b with $\delta_{\mathrm{occ}} = 1.47 \pm 0.21$ ppt in the NIR band at 2.1 µm. Using the space-based *TESS* visible-band data, these are WASP-18 b with $\delta_{\mathrm{occ}} = 0.35 \pm 0.01$ ppt, WASP-36 b with $\delta_{\mathrm{occ}} = 0.18 \pm 0.05$ ppt and WASP-50 b with $\delta_{\mathrm{occ}} = 0.20 \pm 0.06$ ppt. These values imply the following geometric albedos, respectively: $A_{\mathrm{g}} < 0.04$, $A_{\mathrm{g}} = 0.30^{+0.09}_{-0.10}$ and $A_{\mathrm{g}} = 0.56^{+0.17}_{-0.18}$. However, in the case of WASP-50 b the resulting values are probably overestimated and therefore the real occultation depth and the geometric albedo are expected to be lower.

Besides clear occultation detections, 3σ upper limits from the remaining data sets were placed and in some cases they led to reasonable geometric albedos (*TESS*). Specifically, WASP-43 b resulted in $\delta_{\mathrm{occ}}^{3\sigma\mathrm{UL}} < 0.175$ ppt leading to $A_{\mathrm{g}} < 0.153$ and WASP-51 b resulted in $\delta_{\mathrm{occ}}^{3\sigma\mathrm{UL}} < 0.109$ ppt leading to $A_{\mathrm{g}} < 0.367$. The occultation upper limits obtained from the NIR observations constrain planetary thermal radiation rather than the reflected light. Therefore, NIR albedos are not discussed or compared. The obtained geometric albedos and their upper limits are consistent with very low or zero albedos (except WASP-50 b). This is expected and typically observed on hot Jupiters since there is absence of reflective clouds and hazes in their hot atmospheres.

Hot Jupiter planets have usually poor heat redistribution, both across the irradiated hemisphere at a time and between the hemispheres. The energy redistribution can be in the first approximation described with the heat redistribution factor. For most of the planets this factor resulted in ambiguous constraints. An exception is WASP-43 b suggesting partial distribution of heat from the dayside to the nightside which is consistent with the atmosphere model, see further. Another exception is the heat redistribution factor of WASP-18 b inferred from the *TESS* data and resulting in instantaneous reradiation of heat, i.e. no energy redistribution. The heat redistribution factor of this planet was also derived from a NIR data set (NB2090). Nevertheless, the obtained occultation depth was found to be substantially underestimated.

The discussed characteristics also indicate a temperature contrast between the calculated brightness and equilibrium temperature of each of the studied planets, showing a temperature contrast between the planetary hemispheres. It is most apparent at the

planets with the poorest day–night heat redistribution. This applies for the majority of the investigated planets in this thesis with the exception of WASP-43 b. There is no strong temperature difference between the brightness and equilibrium temperature and this supports the result of the heat redistribution factor.

Most of the analysed data sets led to placing upper limits on the occultation depths. These were derived in cases when a clear occultation detection was not reached. As for the *TESS* data, this was a consequence of a too shallow occultation depth (e.g. WASP-51 b) or low stellar brightness (OGLE-9), or both. However, the occultation non-detections from the data acquired by the ground-based facilities are mainly caused by time-correlated red noise. The study revealed that the strongest contributor to the red noise is seeing, or more precisely—its variance. The trend of the measured differential flux is the same as the trend of seeing which indiates a high level of correlation. To increase the probability of detecting an occultation, it is crucial to observe the target during stable seeing conditions. Another effect on the results is the mode used for the observations. Whilst using Generic Offset Mode of HAWK-I led to an occultation detection from data affected by variable seeing (WASP-43, NB2090), the use of Fast Photometry Mode of the same instrument did not result in a clear detection even though seeing was changing within a similar range (e.g. WASP-18 b with a supposed large occultation depth).

Although most data are red-noise limited, time-uncorrelated photon (white) noise also plays a role in the obtained results. It concerns WASP-36/ *TESS* but especially OGLE-9 with a visual magnitude of $\approx$ 14 mag where the data are mainly affected by the white noise and for the *TESS* case they are purely white-noise limited. It is not suprising since the diameter of pupils of *TESS* ($\approx$ 10 cm) is too small to observe such faint targets with a high signal-to-noise ratio.

The last part of the thesis included introducing and description of models of thermal emission of the atmospheres of WASP-18 b and WASP-43 b. Since these planets represent opposite edges of hot-Jupiter group of planets, they are good targets for a comparative study via atmosphere characterisation. Moreover, the planets are best measured and thus a sufficient amount of data is available to be compared with the models. The derived models are able to explain the herein presented *TESS* and HAWK-I observations as well as those adopted, *HST* and *Spitzer*. Solar metallicity and C/O ratio of 1 and 0.5, respectively for WASP-18 and WASP-43, were set to explain the data. The models of both the planets require inefficient heat redistribution on the dayside and between the hemispheres although the model of WASP-43 b fits the data if 10 % of the incident energy is distributed from the dayside to the nightside. This agrees with observations indicating low efficiencies of energy distribution for highly irradiated planets. Another characteristics being in common for both the planets is that reflected light is not needed to explain the observations, i.e. they are consistent with pure thermal emission. It corresponds to the absence of reflective clouds and/or hazes in the atmospheres. Together with the thermal emission models pressure-temperature profiles were computed. They show that a temperature inversion is required to match the thermal emission spectrum of WASP-18 b (hotter) whilst no inversion is needed in the case of WASP-43 b (cooler). Although there is a strong temperature contrast between these planets, results obtained from the observations do not suggest that clouds and/or hazes are present on the dayside of each of the planets.

These new models which besides adopted data include data from observations of occultations presented in this thesis were originally published in an own article, Blažek et al. (2022). It has to be noted, however, that for this thesis new analyses of all the data sets with subtly different approach were performed. This explains the slight differences between results presented here and in the mentioned article. Moreover, this thesis contains

additional new results of these above-discussed systems as well as of others which are not included in the article.

The number of newly discovered hot Jupiters as well as other-type exoplanets is still growing and along with that our knowledge about their atmospheres. Observations in the visible and infrared bandpasses are complementary since to derive an optical albedo thermal radiation has to be known from infrared measurements. This further enables to put constraints on scattering sources, temperature structures, chemical composition, etc. However, to infer such details precise measurements are required. As presented in this thesis, these are not always reached even if powerful facilities are used for observations. With ground-based telescopes we are limited by the Earth's atmosphere and its 'whims' whilst small sizes of most space-mission telescopes do not allow to detect slight changes in brightness accompanying processes in planetary atmospheres or atmospheres themselves. Nevertheless, new state-of-the-art facilities, such as e.g. ongoing *JWST* or being currently built ELT, will certainly increase the number of answered questions; and on the other hand, it will give rise to brand new exciting ones without any doubts.

A. List of used constants and acronyms

Name	Symbol	Value	Unit
Boltzmann constant	k_B	$1.381 \cdot 10^{-23}$	$J\,K^{-1}$
Planck constant	h	$6.626 \cdot 10^{-34}$	J s
Speed of light	c	$2.998 \cdot 10^{8}$	$m\,s^{-1}$
The mass of the Sun	$M_\odot$	$1.988 \cdot 10^{30}$	kg
The mass of Jupiter	M_J	$1.898 \cdot 10^{27}$	kg
The mass of the Earth	$M_\oplus$	$5.972 \cdot 10^{24}$	kg
The radius of the Sun	$R_\odot$	695,700,000	m
The radius of Jupiter	R_J	71,492,000	m

ESA	European Space Agency
ESO	European Southern Observatory
ICRS	International Celestial Reference System
NASA	National Aeronautics and Space Administration

References and electronic sources

Anderson D. R., et al., 2010, A&A, 513, L3

Angerhausen D., DeLarme E., Morse J. A., 2015, PASP, 127, 1113

Appenzeller I., et al., 1998, The Messenger, 94, 1

Arcangeli J., et al., 2018, ApJL, 855, L30

Arcangeli J., et al., 2019, A&A, 625, A136

Baglin A., Auvergne M., Barge P., Deleuil M., Michel E., CoRoT Exoplanet Science Team 2009, in Pont F., Sasselov D., Holman M. J., eds, IAU Symposium Vol. 253, Transiting Planets. pp 71–81, doi:10.1017/S1743921308026252

Bai L., Gu S., Wang X., Sun L., Kwok C.-T., Hui H.-K., 2022, AJ, 163, 208

Baraffe I., Chabrier G., Barman T. S., Allard F., Hauschildt P. H., 2003, A&A, 402, 701

Batalha N. M., et al., 2011, ApJ, 729, 27

Beatty T. G., et al., 2020, AJ, 160, 211

Bell T. J., et al., 2017, ApJL, 847, L2

Blažek M., 2017, Master's thesis, Masaryk University, Brno, Czech Republic

Blažek M., et al., 2022, MNRAS, 513, 3444

Blecic J., et al., 2014, ApJ, 781, 116

Borucki W. J., et al., 2010a, in American Astronomical Society Meeting Abstracts #215. p. 101.01

Borucki W. J., et al., 2010b, Science, 327, 977

Brandeker A., et al., 2022, A&A, 659, L4

Burrows A., Sharp C. M., 1999, ApJ, 512, 843

Burrows A., et al., 1997, ApJ, 491, 856

Burrows A., Hubeny I., Sudarsky D., 2005, ApJ, 625, L135

Burrows A., Ibgui L., Hubeny I., 2008, ApJ, 682, 1277

Campbell B., Walker G. A. H., Yang S., 1988, ApJ, 331, 902

Casali M., et al., 2006, in McLean I. S., Iye M., eds, Society of Photo-Optical Instrumentation Engineers (SPIE) Conference Series Vol. 6269, Society of Photo-Optical Instrumentation Engineers (SPIE) Conference Series. p. 62690W, doi:10.1117/12.670150

Castelli F., Kurucz R. L., 2003, in Piskunov N., Weiss W. W., Gray D. F., eds, Vol. 210, Modelling of Stellar Atmospheres. p. A20 (arXiv:astro-ph/0405087), doi:10.48550/arXiv.astro-ph/0405087

Charbonneau D., Brown T. M., Latham D. W., Mayor M., 2000, ApJL, 529, L45

Charbonneau D., Brown T. M., Noyes R. W., Gilliland R. L., 2002, ApJ, 568, 377

Chauvin G., Lagrange A. M., Dumas C., Zuckerman B., Mouillet D., Song I., Beuzit J. L., Lowrance P., 2004, A&A, 425, L29

Chen G., et al., 2014, A&A, 563, A40

Colón K. D., Ford E. B., Redfield S., Fortney J. J., Shabram M., Deeg H. J., Mahadevan S., 2012, MNRAS, 419, 2233

Cortés-Zuleta P., Rojo P., Wang S., Hinse T. C., Hoyer S., Sanhueza B., Correa-Amaro P., Albornoz J., 2020, A&A, 636, A98

Cowan N. B., Agol E., 2011, ApJ, 729, 54

Dai F., Winn J. N., Yu L., Albrecht S., 2017, AJ, 153, 40

Davoudi F., Baştürk Ö., Yalçınkaya S., Esmer E. M., Safari H., 2021, AJ, 162, 210

Demory B.-O., et al., 2011, ApJL, 735, L12

Demory B.-O., et al., 2013, ApJL, 776, L25

ESO. European Southern Observatory. http://www.eso.org/

Enoch B., et al., 2011, AJ, 142, 86

Esteves L. J., De Mooij E. J. W., Jayawardhana R., 2015, ApJ, 804, 150

Evans T. M., et al., 2013, ApJL, 772, L16

Foster A. S. D., 2016, Atmospheric, Orbital, and Eclipse-Depth Analysis of the Hot Jupiter HAT-P-30-WASP-51Ab, Honors Undergraduate Theses, https://stars.library.ucf.edu/honorstheses/74

Foster A. S., Harrington J., Cubillos P., Blecic J., Challener R., Foster A. J., Garland J., 2016, in American Astronomical Society Meeting Abstracts #227. p. 212.05

Fraine J., et al., 2021, AJ, 161, 269

Freudling W., Romaniello M., Bramich D. M., Ballester P., Forchi V., García-Dabló C. E., Moehler S., Neeser M. J., 2013, A&A, 559, A96

Gandhi S., Madhusudhan N., 2017, MNRAS, 472, 2334

Gardner J. P., et al., 2023, PASP, 135, 068001

Gatewood G., Eichhorn H., 1973, AJ, 78, 769

Gibson N. P., et al., 2010, MNRAS, 404, L114

Gillon M., et al., 2011, A&A, 533, A88

Gillon M., et al., 2012, A&A, 542, A4

Griffin R., 1973, MNRAS, 162, 243

Günther M. N., Daylan T., 2019, Allesfitter: Flexible Star and Exoplanet Inference From Photometry and Radial Velocity, Astrophysics Source Code Library (ascl:1903.003)

Günther M. N., Daylan T., 2021, ApJS, 254, 13

Hatzes A. P., Cochran W. D., Endl M., McArthur B., Paulson D. B., Walker G. A. H., Campbell B., Yang S., 2003, ApJ, 599, 1383

Hellier C., et al., 2009, Nature, 460, 1098

Hellier C., et al., 2011, A&A, 535, L7

Huber K. F., Czesla S., Schmitt J. H. M. M., 2017, A&A, 597, A113

Husser T. O., Wende-von Berg S., Dreizler S., Homeier D., Reiners A., Barman T., Hauschildt P. H., 2013, A&A, 553, A6

Jenkins J. M., et al., 2016, in Chiozzi G., Guzman J. C., eds, Society of Photo-Optical Instrumentation Engineers (SPIE) Conference Series Vol. 9913, Software and Cyberinfrastructure for Astronomy IV. p. 99133E, doi:10.1117/12.2233418

Johnson J. A., et al., 2011, ApJ, 735, 24

Kataria T., Showman A. P., Fortney J. J., Stevenson K. B., Line M. R., Kreidberg L., Bean J. L., Désert J.-M., 2015, ApJ, 801, 86

Keating D., Cowan N. B., 2017, ApJL, 849, L5

Kipping D. M., Spiegel D. S., 2011, MNRAS, 417, L88

Kissler-Patig M., et al., 2008, A&A, 491, 941

Knutson H. A., et al., 2007, Nature, 447, 183

Knutson H. A., Charbonneau D., Allen L. E., Burrows A., Megeath S. T., 2008, ApJ, 673, 526

Kreidberg L., et al., 2014, ApJL, 793, L27

Latham D. W., Mazeh T., Stefanik R. P., Mayor M., Burki G., 1989, Nature, 339, 38

Lecavelier des Etangs A., Lissauer J. J., 2022, New Astronomy Reviews, 94, 101641

Lendl M., Afonso C., Koppenhoefer J., Nikolov N., Henning T., Swain M., Greiner J., 2010, A&A, 522, A29

MAST. Mikulski Archive for Space Telescopes. https://archive.stsci.edu/

Maciejewski G., et al., 2016, Acta Astron., 66, 55

Madhusudhan N., 2012, ApJ, 758, 36

Mallonn M., Köhler J., Alexoudi X., von Essen C., Granzer T., Poppenhaeger K., Strassmeier K. G., 2019, A&A, 624, A62

Mancini L., Kemmer J., Southworth J., Bott K., Mollière P., Ciceri S., Chen G., Henning T., 2016, MNRAS, 459, 1393

Matthews E. C., et al., 2024, Nature, 633, 789

Maxted P. F. L., et al., 2013, MNRAS, 428, 2645

Mayor M., Queloz D., 1995, Nature, 378, 355

Moriarty J., Madhusudhan N., Fischer D., 2014, ApJ, 787, 81

NASA-Archive. NASA Exoplanet Archive. https://exoplanetarchive.ipac.caltech.edu/

Nymeyer S., et al., 2011, ApJ, 742, 35

Parmentier V., Fortney J. J., Showman A. P., Morley C., Marley M. S., 2016, ApJ, 828, 22

Parviainen H., Aigrain S., 2015, MNRAS, 453, 3821

Perryman M., 2018, The Exoplanet Handbook. Cambridge University Press

Pirard J.-F., et al., 2004, in Moorwood A. F. M., Iye M., eds, Society of Photo-Optical Instrumentation Engineers (SPIE) Conference Series Vol. 5492, Ground-based Instrumentation for Astronomy. pp 1763–1772, doi:10.1117/12.578293

Pollacco D. L., et al., 2006, PASP, 118, 1407

Pont F., Zucker S., Queloz D., 2006, MNRAS, 373, 231

Rauer H., Catala C., 2012, in EGU General Assembly Conference Abstracts. EGU General Assembly Conference Abstracts. p. 7033

Redfield S., Endl M., Cochran W. D., Koesterke L., 2008, ApJL, 673, L87

Ricker G. R., et al., 2014, in Oschmann Jacobus M. J., Clampin M., Fazio G. G., MacEwen H. A., eds, Society of Photo-Optical Instrumentation Engineers (SPIE) Conference Series Vol. 9143, Space Telescopes and Instrumentation 2014: Optical, Infrared, and Millimeter Wave. p. 914320 (arXiv:1406.0151), doi:10.1117/12.2063489

Rothman L. S., et al., 2010, Journal of Quantitative Spectroscopy & Radiative Transfer, 111, 2139

Sada P. V., et al., 2012, PASP, 124, 212

Scandariato G., et al., 2022, A&A, 668, A17

Science Software Branch at STScI 2012, PyRAF: Python alternative for IRAF, Astrophysics Source Code Library, record ascl:1207.011 (ascl:1207.011)

Seager S., 2010a, Exoplanet Atmospheres: Physical Processes. Princeton University Press

Seager S., 2010b, Exoplanets. The University of Arizona Press

Sheppard K. B., Mandell A. M., Tamburo P., Gandhi S., Pinhas A., Madhusudhan N., Deming D., 2017, ApJL, 850, L32

Shporer A., et al., 2019, AJ, 157, 178

Siebenmorgen R., Carraro G., Valenti E., Petr-Gotzens M., Brammer G., Garcia E., Casali M., 2011, The Messenger, 144, 9

Simbad. SIMBAD Astronomical Database. http://simbad.u-strasbg.fr/simbad/

Sing D. K., et al., 2011, A&A, 527, A73

Smith J. C., et al., 2012a, PASP, 124, 1000

Smith A. M. S., et al., 2012b, AJ, 143, 81

Snellen I. A. G., et al., 2009, A&A, 497, 545

Snellen I. A. G., de Kok R. J., de Mooij E. J. W., Albrecht S., 2010, Nature, 465, 1049

Southworth J., 2010, MNRAS, 408, 1689

Stevenson K. B., et al., 2017, AJ, 153, 68

Struve O., 1952, The Observatory, 72, 199

Stumpe M. C., et al., 2012, PASP, 124, 985

Swain M. R., Vasisht G., Tinetti G., 2008, Nature, 452, 329

Tamai R., Koehler B., Cirasuolo M., Biancat-Marchet F., Tuti M., González Herrera J.-C., Ramsay S., 2022, in Marshall H. K., Spyromilio J., Usuda T., eds, Society of Photo-Optical Instrumentation Engineers (SPIE) Conference Series Vol. 12182, Ground-based and Airborne Telescopes IX. p. 121821A, doi:10.1117/12.2631613

Tennyson J., et al., 2016, Journal of Molecular Spectroscopy, 327, 73

Tinetti G., et al., 2007, Nature, 448, 169

Tody D., 1986, in Crawford D. L., ed., Society of Photo-Optical Instrumentation Engineers (SPIE) Conference Series Vol. 627, Instrumentation in astronomy VI. p. 733, doi:10.1117/12.968154

Tody D., 1993, in Hanisch R. J., Brissenden R. J. V., Barnes J., eds, Astronomical Society of the Pacific Conference Series Vol. 52, Astronomical Data Analysis Software and Systems II. p. 173

Tregloan-Reed J., Southworth J., 2013, MNRAS, 431, 966

Udalski A., Szymanski M., Kaluzny J., Kubiak M., Mateo M., 1992, Acta Astron., 42, 253

Udalski A., Kubiak M., Szymanski M., 1997, Acta Astron., 47, 319

Van Rossum G., Drake F. L., 2009, Python 3 Reference Manual. CreateSpace, Scotts Valley, CA

Vidal-Madjar A., Lecavelier des Etangs A., Désert J. M., Ballester G. E., Ferlet R., Hébrard G., Mayor M., 2003, Nature, 422, 143

Vidal-Madjar A., et al., 2004, ApJL, 604, L69

Walker G. A. H., Bohlender D. A., Walker A. R., Irwin A. W., Yang S. L. S., Larson A., 1992, ApJL, 396, L91

White W. B., Johnson S. M., Dantzig G. B., 1958, J. Chem. Phys., 28, 751

Wolszczan A., Frail D. A., 1992, Nature, 355, 145

Wong I., et al., 2020, AJ, 160, 155

Zhou G., Bayliss D. D. R., Kedziora-Chudczer L., Tinney C. G., Bailey J., Salter G., Rodriguez J., 2015, MNRAS, 454, 3002

van de Kamp P., 1963, AJ, 68, 515

van de Kamp P., 1982, Vistas in Astronomy, 26, 141

van der Hucht K. A., 2007, Transactions of the International Astronomical Union, Series B, 26, 1